

**National Central University**

國立中央大學

Department of Atmospheric Sciences

大氣科學學系

Master's Thesis

碩士論文

**Investigating the microphysical characteristics of  
precipitation systems during the 2018 Southwest  
Monsoon (SWM) season in South Luzon, Philippines**

菲律賓南呂宋地區降水系統的微物理特徵研究－  
2018年西南季風期間

Author 研究生: **John Ruel Loyola Locaba** 盧嘉瑞

Adviser 指導教授: **Professor Wei-Yu Chang** 張偉裕

June 2025

中華民國 114 年 6 月

# National Central University Library Authorization for Thesis/ Dissertation

Application Date : 2025 / 8 / 4

The latest version since Sep. 2019

Applicant Name	John Ruel L. Locaba 盧嘉瑞	Student Number	<u>112621601</u>
Schools / Departments	Department of Atmospheric Sciences	Graduate Degree	<input checked="" type="checkbox"/> Master <input type="checkbox"/> Doctor
Thesis/Dissertation Title	Investigating the microphysical characteristics of precipitation systems during the 2018 Southwest Monsoon (SWM) season in South Luzon, Philippines	Advisor Name	Wei-Yu Chang 張偉裕

## Authorization for Internet Access of Thesis/ Dissertation

This license authorizes my complete electronic thesis to be archived and read in the

• National Central University Library Electronic Theses & Dissertations System .

- ( ☒ ) Released for Internet access immediately  
(    ) Released for Internet access starting from: \_\_\_\_\_ / \_\_\_\_\_ / \_\_\_\_\_ ( YYYY / MM / DD )  
(    ) Disagree, because: \_\_\_\_\_

• NDLTD(National Digital Library of Theses and Dissertations in Taiwan).

- ( ☒ ) Released for Internet access immediately  
(    ) Released for Internet access starting from: \_\_\_\_\_ / \_\_\_\_\_ / \_\_\_\_\_ ( YYYY / MM / DD )  
(    ) Disagree, because: \_\_\_\_\_

I hereby agree to authorize the electronic versions of my thesis/dissertation and work to National Central University, University System of Taiwan(UST) and National Central Library(National Digital Library of Theses and Dissertations in Taiwan), in a non-exclusive way and without reimbursement, in accordance with the Copyright Act. The fore-mentioned authorized items can be reproduced by the authorized institution in the form of text, video tape, audio tape, disc and microfilm, or converted into other digital formats, without the limitation of time, places, and frequency for non-commercial uses.

## Delayed Public Release for Paper Copy of Thesis/Dissertation

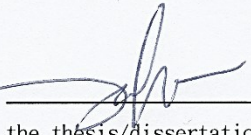
(You do not need to fill out this section if you make the paper copy of your thesis/dissertation available to the public immediately.)

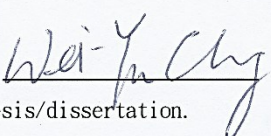
• Reasons for the delayed release (choose one)

- (    ) Filing for patent registration. Registration number: \_\_\_\_\_  
(    ) Submission for publication  
(    ) Your research contains information pertaining to national non-disclosure agreements.  
(    ) Contents withheld according to the law. Please specify \_\_\_\_\_

• Delayed Until : \_\_\_\_\_ / \_\_\_\_\_ / \_\_\_\_\_ ( YYYY / MM / DD )

You should submit another paper copy to National Central Library (NCL) through the NCU Division of Registrar. If you would like to delay the release of this paper copy in NCL, please fill out the "Application for Embargo of thesis/dissertation" of NCL.

Signature of the Applicant : 

Signature of the Advisor : 

\*Please attach this form after the thesis/dissertation cover when submitting your thesis/dissertation.



國立中央大學碩士班研究生  
論文指導教授推薦書

大氣科學學系大氣物理碩士班 學系/研究所 盧嘉瑞 研究生  
所提之論文 Investigating the microphysical characteristics of  
precipitation systems during the 2018 Southwest Monsoon  
(SWM) season in South Luzon, Philippines

係由本人指導撰述，同意提付審查。

指導教授 張博鈞 (簽章)

114 年 7 月 2 日



國立中央大學碩士班研究生  
論文口試委員審定書

大氣科學學系大氣物理碩士班 學系/研究所 盧嘉瑞 研究生  
所提之論文 Investigating the microphysical characteristics of  
precipitation systems during the 2018 Southwest Monsoon  
(SWM) season in South Luzon, Philippines  
經由委員會審議，認定符合碩士資格標準。

學位考試委員會召集人

委

員

林品芳

林沛練

張傳裕

中 華 民 國

114 年

7 月

22日



## 中文摘要

西南氣流 (Southwest Monsoon, SWM) , 每年為菲律賓帶來近過半的降雨, 過往有許多相關研究, 然而降雨中的微物理卻未被探索。本研究使用2018年六至九月期間, PARSIVEL 雨滴譜儀的觀測, 以及位於Tagaytay的 C波段雙偏極化氣象雷達的資料, 分析菲律賓南方呂宋島 (South Luzon) 降雨的微物理特徵。將降水分為四種型態: 大範圍強對流 (SWC)、獨立強對流 (SIC)、淺對流 (WC) 與層狀 (WS) 降水。利用主成份分析法 (PCA) 分析雨滴粒徑分布 (Drop Size Distribution, DSD) 和降雨積分參數 (integral rain parameters), 客觀地將DSD分群 (PCA Groups, PGs) 以分析和不同微物理過程的關聯。

透過比對PGs和雷達參數, 如: 回波 ( $Z_H$ )、差異反射率 ( $Z_{DR}$ )、比差異相位差 ( $K_{DP}$ ) 與相關係數 ( $\rho_{HV}$ ) 時間序列剖面圖, 顯示雷達參數垂直分佈與時序變化和微物理過程特徵一致。SIC由高濃度的中至大雨滴組成, 伴隨高 $Z_H$ 、 $Z_{DR}$ 與 $K_{DP}$ 數值, 且發展達高度10公里, 觀測到以冰相為基礎的PG對流分群, 並伴隨降雨率 ( $R$ )、液態水含量 ( $LWC$ ) 和 $Z_H$ 的極值, 也解釋地面觀測到大雨滴的現象。SWC有較廣的雨滴粒徑分布區間, 且許多分群會隨系統轉移, 其 $\log_{10}N_w$  (雨滴濃度 參數)、 $D_m$  (質量權重平均粒滴直徑) 與 $LWC$ 可與SIC相當, 卻伴隨較弱降雨率。WC通常可見高濃度小雨滴的淺對流, 強回波 ( $Z_H > 35$  dBZ) 不超過6公里高。WS主要由小至中型雨滴組成, 低降雨率, 有明顯亮帶訊號, 其DSDs緊密分布於對流/層狀分界線以下。

本研究進一步使用CFAD (Contoured frequency by altitude diagrams) 找出雷達參數垂直結構與PGs的關係。常態對流 (PG1) 與以冰相為主的對流 (PG6) 在各雷達參數均有較高數值, PG6的回波值可達40dBZ, 且出現顯著柱狀 $Z_H$ 、 $Z_{DR}$ 與 $K_{DP}$ 。至於淺對流 (PG3)



的強回波在5公里以下。在CFADs對層狀的分群中，弱層狀 (PG2) 與中度層狀 (PG4) 高頻率地出現低 $Z_H$ 、 $Z_{DR}$ 與 $K_{DP}$ 數值，中度層狀因為更強的融解作用，稍微有著更高的數值，較大的雨滴會反映在 $Z_{DR}$  CFAD中。上述發現對於菲律賓過往降雨事件研究中未提及的部分，提供了更詳盡的觀點。



# **Investigating the microphysical characteristics of precipitation systems during the 2018 Southwest Monsoon (SWM) season in South Luzon, Philippines**

John Ruel Loyola Locaba<sup>1</sup> and Wei-Yu Chang<sup>1</sup>

(1) Department of Atmospheric Sciences, National Central University,  
Zhongli District, Taoyuan City, Taiwan

## **Abstract**

The Southwest Monsoon (SWM), which brings nearly half of the Philippines' annual rainfall, has been extensively studied; however, its rainfall microphysics remain largely unexplored. This study investigates the microphysical characteristics of rainfall in South Luzon, Philippines, during the 2018 SWM season (June to September), using data from a PARSIVEL disdrometer and the Tagaytay C-band dual-polarization weather radar.

Four precipitation types are presented: strong widespread convection (SWC), strong isolated convection (SIC), weak shallow convection (WC), and weak stratiform (WS). Applying principal component analysis (PCA) to the drop size distribution (DSD) and integral rain parameters, PCA groups (PGs) are identified and linked to dominant microphysical processes. PGs and the averaged time-height plots of reflectivity ( $Z_H$ ), differential reflectivity ( $Z_{DR}$ ), specific differential phase ( $K_{DP}$ ), and co-polar cross-correlation coefficient ( $\rho_{HV}$ ) were time-matched to reveal these processes. SIC exhibited high concentrations of mid-to-large drops and with high  $Z_H$ ,  $Z_{DR}$ , and  $K_{DP}$  values reaching heights up to 10 km —typical for deep convective systems. Most ice-based convection DSDs (PG6) were observed after the peak rainfall rate ( $R$ ), liquid water content ( $LWC$ ), and  $Z_H$ , explaining the large drops observed at the surface. SWC showed wider range of drop diameters with multiple PGs observed showing the transitions within the system. The values of normalized intercept parameter ( $\log_{10}N_w$ ), mass-weighted mean diameter ( $D_m$ ) and  $LWC$  are comparable to SIC, but with lower  $R$ . High concentrations of small drops were typically observed in WC, but convective reflectivities ( $>35$  dBZ) were confined at the lower levels, hence the shallow classification. Meanwhile, in WS, small to mid-sized drops dominate, with low  $R$ , with an evident bright band signature and DSDs are tightly clustered below the convective-stratiform (CS) separation line.

Contoured frequency by altitude diagrams (CFAD) were used to relate radar vertical profiles to specific PGs. Both normal convection DSD group (PG1) and PG6 have high values



of the same radar parameters. However, reflectivity values for PG6 are centered around 40 dBZ and usually show pronounced columns of  $Z_H$ ,  $Z_{DR}$  and  $K_{DP}$ . For shallow convection (PG3), high values of  $Z_H$  ( $\geq 35$  dBZ) are confined below 5 km suggesting the less intense and shallow nature of this convection compared to other convective groups. CFADs for stratiform groups—weak (PG2) and moderate (PG4) — revealed high frequencies of low  $Z_H$ ,  $Z_{DR}$  and  $K_{DP}$  values. PG4 has slightly higher values, likely due to more intense melting, which produces larger drops as reflected in the  $Z_{DR}$  CFAD. These findings provide a more detailed perspective on Philippine precipitation systems which were not presented in previous literature.



## Acknowledgments

To **Dr. Wei-Yu Chang**, *the best adviser and mentor*, who patiently taught me way more than just doing research but also to become a better teacher and mentor myself. Through his words and personal example, I learned to trust in people's potential and that sometimes all it takes is for someone to believe. Thank you, Professor Chang, for taking a risk even when I am completely clueless, and for constantly reassuring me that I am good and way more capable than I imagine.

To my other professors in the laboratory, **Dr. Yu-Chieng Liou** and **Dr. Kao-Shen Chung**, for their patience, encouragement, and kind words. And for reminding me that what I'm doing is not only for myself but also for my country.

To the Radar Meteorology Laboratory, especially to **Dr. Jui Le (Haidy) Loh** for patiently sharing her expertise in handling radar data. And to **Xiao-Na** for all the help. *I had fun.*

To my home university, Bicol University, especially the College of Science and the Department of Physics and Meteorology. To **Mam Jocelyn Serrano**, **Sir Jason Punay**, **Mam Amelia Dorosan**, **Mam Marierose Jasareno**, **Mam Jo-Ann Cordovilla**, **Mam Karen Conda-Botin**, **Sir Erwin Bañares** and **Mam Jennifer Banton** for the endless support and encouragement. To the BU-CHED LAKAS team, especially to **Mam Lany Maceda** and **Mam Jennifer Llovido**, for willingly stepping in to help me when I started out.

To **Surya Pramod**, for leading the way and for making it easier as I navigated graduate school in NCU.

To my rainfall microphysics friends, **Larry Ger Aragon** and **Marco Polo Ibañez** for helping me understand the confusing parts of the research.

To my classmates who became my good friends. **Lien-Xiang**, **Chi-Chun**, **Shi-Kai**, **Yun-An**, **Yi-Tong**, **You-Wei**, **Yong-Wei**, **Wei-Hsien**, **Kai-Ting** and **Xian-Zheng**. I am fortunate and very grateful that you are my classmates. I had a good time in the university because of you. I know all of you will do great things in the future.

To **Hao-Yu**, my Taiwanese brother and best friend. Your friendship made me feel less lonely and less isolated in this foreign land. To **Zaimund** who became my closest Filipino friend in NCU, **Meng-Jie**, **Chih-Lung** and **Ting-Kai**— *we had good times!* I'm proud to say I made very good friends in Taiwan.

To all my good friends —old and new.

To my family. Mama and Papa, *this is for you.*

*I hope I made you all proud!*

John Ruel 盧嘉瑞

# Table of Contents

中文摘要	i
Abstract	iii
Acknowledgments.....	v
Table of Contents.....	vi
List of Figures .....	viii
List of Tables.....	xii
List of Abbreviations .....	xiii
<b>Chapter 1 INTRODUCTION .....</b>	<b>1</b>
1.1 On precipitation microphysics .....	1
1.2 The Philippine Southwest Monsoon (SWM) season .....	2
1.3 Motivation of the study.....	3
1.4 Scope and Delimitation.....	4
<b>Chapter 2 DATA AND METHODS.....</b>	<b>5</b>
2.1 Domain, instrumentation and data .....	5
2.2 Disdrometer data and quality control procedures .....	6
2.3 Calculation of DSD information and integral rainfall parameters.....	10
2.4 T-matrix scattering simulation .....	12
2.5 Tagaytay C-band weather radar data and quality control procedures.....	13
2.5.1 $\Phi_{DP}$ processing.....	14
2.5.2 Removal of noise and non-meteorological signals .....	15
2.5.3 Attenuation correction.....	16
2.5.4 $Z_{DR}$ system bias correction.....	18
2.6 Time-height plots of averaged dual polarization parameters .....	18
2.7 Principal component analysis on DSD data.....	19
2.8 Selection and description of case studies.....	20
2.9 Contoured Frequency by Altitude Diagrams (CFAD) per PCA group .....	20
<b>Chapter 3 RESULTS AND DISCUSSIONS.....</b>	<b>22</b>
3.1 Seasonal variation of DSD in South Luzon .....	22
3.2 Modes of DSD .....	25
3.3 Microphysical characteristics of precipitation during 2018 SWM season .....	27
3.3.1 Strong Widespread Convection .....	27
3.3.2 Strong Isolated Convection.....	31
3.3.3 Weak Shallow Convection .....	33



3.3.4 Weak Stratiform .....	35
3.3.5 CFAD-PCA Group analysis .....	37
<b>Chapter 4 CONCLUSION .....</b>	<b>45</b>
4.1 Summary .....	45
4.1.1 Seasonal variability of DSD in South Luzon, Philippines.....	45
4.1.2 Modes of DSD .....	45
4.1.3 DSD-radar joint analysis.....	46
4.1.4 Conclusion .....	47
4.2 Future work.....	47
<b>References</b>	<b>49</b>
<b>Appendix</b>	<b>54</b>

# List of Figures

Figure 2.1 Digital Elevation Map (DEM) of the area of study from the NASA Shuttle Radar Topography Mission (SRTM) (2013). The location of the Tagaytay weather radar is represented by the yellow star symbol, while the red box represents the site of the PARSIVEL disdrometer. The triangles are the locations of DOST-PAGASA synoptic stations: Port Area, Manila (blue), Ambulong, Batangas (green) and Science Garden in Quezon City (magenta). .....	7
Figure 2.2 2018 to 2024 plots for TC vs non-TC days. Note that there is no data for 2021.....	8
Figure 2.4 Sample DSD (a) before, and (b) after QC process, and (c) mean bias (dBR) calculated from observed rainfall vs calculated rainfall from disdrometer. ....	9
Figure 2.3 The quality control process implemented for the disdrometer data. ....	9
Figure 2.5 The quality control process implemented for the Tagaytay weather radar data.....	14
Figure 2.6 Sample raw PPI plots for (a) $Z_H$ , (b) $Z_{DR}$ , (c) $\rho_{HV}$ , and (d) $\Phi_{DP}$ showing issues that need to be addressed in the QC process. The x- and y-axis are range in kilometers.....	14
Figure 2.7 $\Phi_{DP}$ processing for Tagaytay C-band radar data. (a) $\Phi_{DP}$ raw data and (b) $\Phi_{DP}$ after unfolding. Green box is the area of folding shown by the abrupt shift from positive values to negative values. ....	15
Figure 2.8 Removing non-meteorological signals for Tagaytay C-band radar data. (a) $Z_H$ raw data and (b) $Z_H$ after $\rho_{hv}$ and $\sigma\Phi_{DP}$ thresholds were applied. ....	16
Figure 2.9 Attenuation coefficients ( $\alpha$ and $\beta$ ) derived from fitting $K_{DP-A_H}$ and $K_{DP-A_{DP}}$ respectively for (a) all season data, (b) SWM, (c) NEM, and (d) transition months (TRA)....	17
Figure 2.10 Pie charts for precipitation type classification and the identified DSD-radar samples. (a) precipitation types, and (b) DSD groups.....	21
Figure 3.1 Frequency distribution of DSD in $\log_{10}N_w-D_m$ plane (a-d), C/S classification (e-h). (a, d) all data, (b, f) SWM, (c, g) NEM, and (d, h) transition months.....	23
Figure 3.2 Averaged seasonal DSD per rain rate classes. (a) Class 1, (b) Class 2, (c) Class 3, (d) Class 4, (e) Class 5, and (f) normalized DSD. Red represents SWM, blue represents NEM and TRA shown in green. Values presented in the plot are mean R and count per season per rain rate class. ....	24
Figure 3.3 DSD clusters revealed by principal component analysis (PCA). (a) PC standard anomalies showing distinct groups: red is group 1 (PG1; convective), green is group 2 (PG2; stratiform), yellow is group 3 (PG3, convective), blue is group 4 (PG4; stratiform), group 5 is magenta (PG5; convective) and cyan is group 6 (PG6; convective), all AMB are colored gray, (b) same as (a) but PCA clusters shown in $\log LWC-D_m$ plane, (c) same as (a) and (b) but shown in $R-Z_H$ plane. The black and orange lines are the BR09 and TH15 convective-stratiform (C/S) separation lines. ....	26



Figure 3.4 Time series of rainfall microphysics for SWC representative case (Event 79). (a) R color-coded blue to red to depict time progression; (b) $N(D)$ ; (c) $\log_{10}N_w-D_m$ plot, same color-code as R to depict time; (d) same as (c) but for LWC; (e) PCA DSD groups in $\log_{10}N_w-D_m$ plot; (f) PPI plot of case. ....	28
Figure 3.5 Averaged time-height plots of (a) $Z_H$ (dBZ), (b) $Z_{DR}$ (dB), (c) $K_{DP}$ ( $^{\circ}\text{km}^{-1}$ ), and (d) $\rho_{HV}$ for SWC case. Colored squares below the radar plots are the time series of PGs matched with the vertical profile. Magenta box highlights $\pm 5$ mins from $R_{\max}$ . Black box shows the whole rainfall event time range. Broken line shows the 35 dB contour.....	29
Figure 3.6 Same as Figure 3.5 but for SIC case (Event 55). ....	30
Figure 3.7 Same as Figure 3.6 but for SIC case (Event 55). ....	31
Figure 3.8 Same as Figure 3.5 but for WC case (Event 11). ....	33
Figure 3.9 Same as Figure 3.6 but for WC case (Event 11). 30 dBZ contour line is shown instead of 35 dBZ.....	34
Figure 3.10 Same as Figure 3.5 but for WS case (Event 27). ....	35
Figure 3.11 Same as Figure 3.6 but for WS case (Event 27).....	36
Figure 3.12 Contoured frequency by altitude diagrams (CFAD) of $Z_H$ (dBZ), $Z_{DR}$ (dB) and $K_{DP}$ ( $^{\circ}\text{km}^{-1}$ ) for convective groups (a,d,g) PG1, (b,e,h) PG3, and (c,f,i) PG6. Red dashed line depicts the freezing level at 5 kms.....	38
Figure 3.13 Contoured frequency by altitude diagrams (CFAD) of $Z_H$ (dBZ), $Z_{DR}$ (dB) and $K_{DP}$ ( $^{\circ}\text{km}^{-1}$ ) for stratiform groups (a,d,g) PG2, and (b,d,f) PG4. Red dashed line depicts the freezing level at 5 kms. ....	39
Figure 3.14 PRHIs of different radar parameters for 2018-09-06 (Event 79) which represents the SWC case. (a-e) $Z_H$ (dBZ), (f-j) $Z_{DR}$ (dB), (k-o) $K_{DP}$ ( $^{\circ}\text{km}^{-1}$ ), and (p-t) $\rho_{HV}$ . Time is indicated in each figure. The black triangle represents the relative location of the disdrometer from the TAG radar site. The red box highlights the vertical profile of the atmosphere above the disdrometer. ....	41
Figure 3.15 PRHIs of different radar parameters for 2018-08-06 (Event 55) which represents the SIC case. (a-e) $Z_H$ (dBZ), (f-j) $Z_{DR}$ (dB), (k-o) $K_{DP}$ ( $^{\circ}\text{km}^{-1}$ ), and (p-t) $\rho_{HV}$ . Time is indicated in each figure. The black triangle represents the relative location of the disdrometer from the TAG radar site. The red box highlights the vertical profile of the atmosphere above the disdrometer. ....	42
Figure 3.16 PRHIs of different radar parameters for 2018-06-09 (Event 11) which represents the WC case. (a-e) $Z_H$ (dBZ), (f-j) $Z_{DR}$ (dB), (k-o) $K_{DP}$ ( $^{\circ}\text{km}^{-1}$ ), and (p-t) $\rho_{HV}$ . Time is indicated in each figure. The black triangle represents the relative location of the disdrometer from the TAG radar site. The red box highlights the vertical profile of the atmosphere above the disdrometer. ....	43

Figure 3.17 PRHIs of different radar parameters for 2018-06-10 (Event 27) which represents the WS case. (a-e)  $Z_H$  (dBZ), (f-j)  $Z_{DR}$  (dB), (k-o)  $K_{DP}$  ( $^{\circ}\text{km}^{-1}$ ), and (p-t)  $\rho_{HV}$ . Time is indicated in each figure. The black triangle represents the relative location of the disdrometer from the TAG radar site. The red box highlights the vertical profile of the atmosphere above the disdrometer. .... 44



Figure A. 1 Inventory of PHL Tagaytay radar data and PARSIVEL disdrometer data from 2018-2020. Values represent the number of 1-min DSD data while the shading represents the available radar data. ....	54
Figure A. 2 Inventory of PHL Tagaytay radar data and PARSIVEL disdrometer data from 2022-2024. Values represent the number of 1-min DSD data while the shading represents the available radar data. ....	55
Figure A. 3 ZDR system bias for 09Jun2018, 06Sep2018 and 06Jun2018. Dots and lines are the time series of ZDR and standard deviation. Blue broken line is the mean ZDR calculated from radar, the red line is the mean ZDR from the disdrometer, and the black line shows the calculated $Z_{DR}$ system bias. ....	56
Figure A. 4 $Z_{DR}$ system bias for 06Aug2018, 27Jul2018 and 10Jun2018. Dots and lines are the time series of $Z_{DR}$ and standard deviation. Blue broken line is the mean $Z_{DR}$ calculated from radar, the red line is the mean $Z_{DR}$ from the disdrometer, and the black line shows the calculated $Z_{DR}$ system bias. ....	57
Figure A. 5 $Z_{DR}$ system bias for 16Jul2018, 11Aug018 and 16Sep2018. Dots and lines are the time series of ZDR and standard deviation. Blue broken line is the mean $Z_{DR}$ calculated from radar, the red line is the mean $Z_{DR}$ from the disdrometer, and the black line shows the calculated $Z_{DR}$ system bias. ....	58
Figure A. 6 $Z_{DR}$ system bias for 22Jun2018, 17Jul2018 and 31Aug2018. Dots and lines are the time series of ZDR and standard deviation. Blue broken line is the mean $Z_{DR}$ calculated from radar, the red line is the mean $Z_{DR}$ from the disdrometer, and the black line shows the calculated $Z_{DR}$ system bias. ....	59
Figure A. 7 Frequency distribution of DSD for (a) SWM, (b) NEM, (c) transition months, (d) TC rains, (e) all non-TC rains and (f) average. ....	60

# **List of Tables**

Table 2.1 The Tagaytay C-band weather radar technical specifications.....	6
Table 2.2 Control conditions for T-matrix scattering simulations used to retrieve polarimetric variables from disdrometer data. ....	13
Table 2.3 Monthly (mon_ave) and seasonal (swm_ave) average temperature (°C) from three synoptic stations near the domain based on 1991-2020 climatological normals (DOST-PAGASA, n.d.). Science Garden and Port Area are located north of the domain in Quezon City and City of Manila, respectively. Ambulong station is located in the Province of Batangas which is south of the domain. ....	13
Table 2.4 Attenuation coefficients calculated through least-squares fitting of $K_{DP-A_H}$ and $K_{DP-A_{DP}}$ . ....	18
Table 2.5 PCA group characteristics based on Dolan et. al (2018). ....	19
Table 3.1 Average values of $\log_{10}NW$ and $D_m$ from 2018-2024 disdrometer data for across seasons. C refers to convective, S for stratiform and ave for average values. ....	25

## List of Abbreviations

<i>Af</i>	fully humid
<i>Am</i>	equatorial monsoon
<i>BB</i>	brightband
<i>CFAD</i>	contoured frequency by altitude diagram
<i>CT</i>	continental cluster
<i>DEM</i>	digital elevation map
<i>DOST - PAGASA</i>	Department of Science and Technology - Philippine Atmospheric Geophysical and Astronomical Services Administration
<i>DSD</i>	Drop size distribution
<i>HPE</i>	high precipitation events
<i>IRP</i>	integral rainfall parameter
<i>JJAS</i>	June, July, August, September
<i>LST</i>	local standard time
<i>LWC</i>	liquid water content
<i>MT</i>	maritime cluster
<i>NEM</i>	Northeast Monsoon
<i>NOAA IBTrACS</i>	National Oceanic and Atmospheric Administration International Best Track Archive for Climate Stewardship
<i>PARSIVEL</i>	particle size velocity
<i>PCA</i>	principal component analysis
<i>PC</i>	principal component
<i>PG</i>	PCA group
<i>PRHI</i>	pseudo range height indicator
<i>QC</i>	quality control
<i>QPE</i>	quantitative precipitation estimation
<i>R</i>	rainfall rate
<i>RSD</i>	Raindrop size distribution
<i>SIC</i>	strong isolated convection
<i>SNR</i>	signal-to-noise ratio
<i>SWC</i>	strong widespread convection
<i>SWM</i>	Southwest Monsoon
<i>TC</i>	tropical cyclone
<i>TRA</i>	transition period
<i>UPLB</i>	University of the Philippines-Los Baños
<i>WC</i>	weak shallow convection
<i>WNP</i>	Western North Pacific
<i>WS</i>	weak stratiform



# Chapter 1 INTRODUCTION

This chapter opens the discussion on recent studies and trends in precipitation microphysics studies, the weather and climate of the Philippines specifically discussing the Southwest Monsoon (SWM) season. Finally, the motivation of the study is presented as well as the study's scope and delimitations.

## 1.1 On precipitation microphysics

Understanding the microphysical characteristics and processes behind precipitation systems has crucial implications especially for remote sensing of rainfall and other hydrological applications. Surface instruments such as disdrometers provide information about the drop size distribution (DSD), drop concentration, drop diameter, and other rainfall parameters. Providing more spatial coverage than point observations, weather radars reveal essential details such as reflectivity, shape and type of hydrometeors, and even liquid water content ( $LWC$ ). Combining and relating both data opens opportunities to look at rainfall events in full detail such as developing more accurate rainfall estimates derived from rainfall rate-radar reflectivity ( $R-Z_H$ ) relationships which are significant products used in flood prediction models (Krajewski & Smith, 2002). Moreover, knowing the raindrop spectra helps to improve the microphysics parameterization in numerical models (McFarquhar et al., 2015).

Various climatological and regional differences in the atmospheric environment significantly affect and determine the microphysical characteristics of precipitation (Bringi et al., 2003). Using long term observations from two-dimensional video disdrometers, Bang et al. (2020) showed the differences in DSD characteristics between South Korea (Daegu and Boseong) and the United States (Norman, Oklahoma). Rainfall in the South Korean sites were shown to be light and were derived from shallow systems. Additionally, DSD characteristics were found to be similar to Eastern China DSDs (Chen et al., 2013) and the maritime clusters (MT). On the contrary, rainfall from a more continental environment such as in Norman, Oklahoma, were typically heavy with the collision-coalescence process dictating drop growth as well as the production of graupel and ice particles due to strong updrafts. In another study, Seela et al. (2017) compared the DSDs of Taiwan and Palau— two islands in the western Pacific— with more concentration of mid-sized to large drops observed in Taiwan. In an attempt to generalize and describe DSD, Dolan et al. (2018), hereafter DO18, examined global

disdrometer datasets which was divided into three significant groups: high, mid- and low latitudes. DSD variability was clearly observed using a statistical tool called principal component analysis (PCA) which helped cluster and determine trends within the data.

## **1.2 The Philippine Southwest Monsoon (SWM) season**

The Philippines's geographic location in the Western North Pacific (WNP) basin, which is the most active tropical cyclone (TC) basin globally (Huang et al., 2024), makes it susceptible to various severe weather conditions which brings considerable impacts to both lives and livelihood. In fact, the country expects 18 to 20 TCs annually which peaks during July and August. Coinciding with the TC season, from June to September, the SWM (locally known as “*Habagat*”) becomes active and affects most of the western parts of the country. The differential heating between the greater Asian landmass and the vast waters of the Indian Ocean drives this monsoon system. While it is active, winds prevail from the southwest bringing rains over most of the country. In effect, around 43% of the annual average accumulated rainfall in the country is associated with SWM (Flores & Balagot, 1969; Bagtasa, 2020).

Studies have explored the combined effects of TCs and SWM particularly looking into the enhancing effects of TCs to the monsoon rains. Bañares et al. (2021) studied convective events in Metro Manila from 2013-2014 using observations from a network of 16 automated weather stations. They noted that the highest average accumulated rainfall is from SWM and that rains associated with TCs contributed to almost 25% of the total rainfall. Cayanan et. al. (2011) studied the effects of this TC-monsoon interaction on rainfall through flow decomposition. Their study concluded that the presence of TCs over the northeast of Luzon generate a strong southwesterly wind over the western part of Luzon. These findings are supported by Bagtasa (2019) who analyzed high precipitation events (HPE) during the same season. Interestingly, TC occurrences coincide with more than 90% of the identified HPEs from the dataset. It is further revealed that TCs usually move along a line segment between northern Luzon and Okinawa, Japan during HPEs. In another study, the deepening of the Asian monsoon trough due to the presence of TCs (*Typhoon Haikui* and *Typhoon Utor*) led to the remarkable enhanced SWM events in August 2012 and 2013 (Bagtasa, 2023).

Though the Philippines has a network of weather radars managed by the Department of Science and Technology - Philippine Atmospheric Geophysical and Astronomical Services Administration (DOST - PAGASA), the country's weather bureau, the use of radars to observe SWM rain events is still relatively underexplored. The study of Heistermann et al. (2013) is the

first to use radar data from the Subic S-band radar in Zambales, Philippines in combination with the dense rain gauge network in Metro Manila to reconstruct the enhanced SWM event in August 2012. The study revealed that if the rainfall field moved no more than 20 kms eastward, it would have increased the Marikina River peak discharge to 30% which may mean more damage than what was experienced in Metro Manila. Using another radar from the network, Crisologo et al. (2014) evaluated the potential for quantitative precipitation estimation (QPE) of the Tagaytay C-band dual polarization dual polarization weather radar. An elaborate quality control (QC) process was implemented though the reflectivity was still deemed underestimated due to radar miscalibration. Also using the Subic radar, Abon et al. (2016) evaluated the potential of using QPE products in application to a hydrological model. In a recent study, Macuroy et al. (2021) evaluated radar QPE from the Tagaytay radar using raindrop size distribution (RSD) in Southern Luzon. These studies, though few in number, highlights the potential of use of weather radars and its applications in the Philippines.

Aside from climatological studies focusing on the dynamics of SWM, several research has been conducted to understand the microphysical characteristics and processes associated with the SWM rain events. Using observations from four disdrometers from 2020-2022, Ibañez et al. (2022) analyzed the RSD of SWM in the western Philippines. The larger drops from convective rains observed at the Clark station are said to be influenced by the terrain and both the maritime and continental air, thus, the continental-maritime clusters (Bringi et al., 2003) are not observed. Ibañez et al. (2023) further looked into the DSD characteristics of SWM focusing in Metro Manila and developed QPE relations from disdrometer data. On the other hand, Aragon et al (2024) provided a detailed discussion on the seasonal differences in DSD characteristics between the monsoon systems noting the abundance of smaller drops during the Northeast Monsoon (NEM) season and, conversely, the high concentration of mid-sized to large drops in both the transition months (TRA) and SWM.

### **1.3 Motivation of the study**

The SWM has been extensively studied in the past decade albeit from a synoptic and climatological perspective. Most of what is known about this monsoon season is limited by the lack of studies using both surface and radar observation data. Thus, this study endeavors to investigate the microphysical characteristics of precipitation systems in South Luzon, Philippines during the 2018 SWM season using the combined DSD observations from PARSIVEL disdrometer and the Tagaytay radar, specifically answering the following questions:

- a) How do DSDs vary among precipitation types during the SWM season in South Luzon based on disdrometer observations?
- b) How are these variations in rainfall microphysics reflected in dual-polarimetric variables in different precipitation types?

#### **1.4 Scope and Delimitation**

To have a general description of the seasonal variability of the DSD in South Luzon, Philippines, this study used the whole set of DSD data (2018-2024). However, for the joint DSD-radar analysis of rainfall events, this research only focused on the 2018 SWM season due to the limited data availability for other seasons. The microphysical analysis is only limited to the calculated integral rainfall parameters (IRP) shown in Chapter 2. These parameters were chosen since they describe both the DSD and the DSD variability. The Tagaytay C-band weather radar data, upon inspection, significantly requires quality control (QC) process to ensure the usability of the data. The QC steps implemented for the radar data are determined as needed. The QC steps implemented may deviate or add to the existing QC steps done by DOST - PAGASA or the earlier published papers using the same radar. While there are significant improvements in the data, issues may still remain unresolved which can be attributed to the hardware issues.



## Chapter 2 DATA AND METHODS

This chapter introduces the domain of the research study, the instruments used and as well as the data gathered. This also tackles the quality control procedures implemented for both the disdrometer and radar data, related processes in obtaining DSD and IRPs, principal component analysis of DSD, and selection of case studies which best describes a certain type of precipitation in South Luzon. Finally, the process of matching DSD groups to radar is also discussed.

### 2.1 Domain, instrumentation and data

According to the updated Köppen-Geiger climate classification (Kottek et al., 2006), the climate of the Philippines, an archipelagic country in Southeast Asia, is considered both equatorial rainforest, fully humid (*Af*), and equatorial monsoon (*Am*). The climate of South Luzon, our subject domain, is under the combined influence of Climate I and Climate III based on the Modified Coronas Classification (Flores & Balagot, 1969). Generally, June to September (JJAS) is considered the wet season with the SWM bringing most of the rain. The rest of the year is divided into NEM season (October to February), and the transition months (TRA) from March to May. These follows the classification used by Aragon et. al. (2024). The present study, while it also discusses the variability across the seasons, will put much emphasis on the SWM season since an average of 43% of the annual rainfall in the country can be attributed to this season (Asuncion & Jose, 1980).

To observe microphysical characteristics of rainfall, a PARSIVEL disdrometer (hereafter, disdrometer) has been installed at the Agrometeorology station inside the University of the Philippines-Los Baños (UPLB) compound. This disdrometer uses laser emitter and a receiver which measures changes in signal voltage when hydrometeors pass through. This simultaneously measures particle size and velocity of precipitation with 1-min sampling interval and groups them into 32 bins (Löffler-Mang & Joss, 2000). Using this data, one can derive drop concentration, particle diameter as well as the kinetic energy of the hydrometeors. We can also determine the type, calculate intensity and amount of precipitation, and other IRPs. Details about these are discussed in the next section.

The primary source of weather radar data for this study is the Tagaytay C-band dual-polarization radar (hereafter, radar) which sits at the highest peak of the Tagaytay ridge in the southern part of Luzon, Island, Philippines (Figure 2.1). This radar is around 40 kms south of

Metro Manila and around 24 kms west of the disdrometer. The radar scans every 10 minutes and, given the altitude, with the lowest data available at about 1-km above the surface. This radar is one of the major radars from the weather bureau's network. It has run operationally and regularly maintained by DOST-PAGASA since 2012. The radar technical specifications are shown in Table 2.1.

*Table 2.1 The Tagaytay C-band weather radar technical specifications.*

<b>Specification</b>	<b>Value</b>
Radar Name	DWSR-93C
Location	Lat: 14°8'31" / Lon: 121°1'19"
Altitude	752 m a.m.s.l.
Polarization	Dual-Pol
Wavelength	5.34375 cm
Peak Power	250 kW
Antenna Diameter	4.3 m
Maximum Range	120 km
Gate Length	500 m
Volume Cycle Interval	10 min
Transmission	Simultaneous
Elevation Angle (°)	0.5, 1.0, 1.5, 2.4, 3.4, 4.3, 5.3, 6.2, 7.5, 8.7, 10, 12, 14, 16.7, 19.5

## **2.2 Disdrometer data and quality control procedures**

The DSD characteristics of precipitation was observed through the PARSIVEL disdrometer (hereafter disdrometer), which gathers 1-minute samples of both the size and fall velocity of drops. This study made use of both 1-minute and 6-minute DSD samples with the former used to observe the behavior of the DSD per rain event in terms of rainfall rate, measurements of the logarithmic form of the normalized intercept parameter ( $\log_{10}N_W$ ;  $\text{m}^{-3} \text{mm}^{-1}$ ), mass-weighted mean diameter ( $D_m$ ; mm) and  $LWC$  ( $\text{g m}^{-3}$ ) while the latter is used for the simulation of dual polarimetric parameters via the T-matrix scattering method.

The disdrometer collected data starting May 2018 up to the present (as of this writing). The data inventory shown in Figure A.1 and A.2 (see *Appendix*), revealed periods of sparse to no data recorded. This inconsistency is attributed to certain factors: (1) *frequent power interruption at the site*, and (2) *operations was severely affected during the COVID-19 pandemic*. Though this lack can evidently affect the overall representation of the seasonal variability of DSD in the chosen domain, enough DSD samples were gathered for the SWM season in 2018 and thus this season is deemed sufficiently represented.

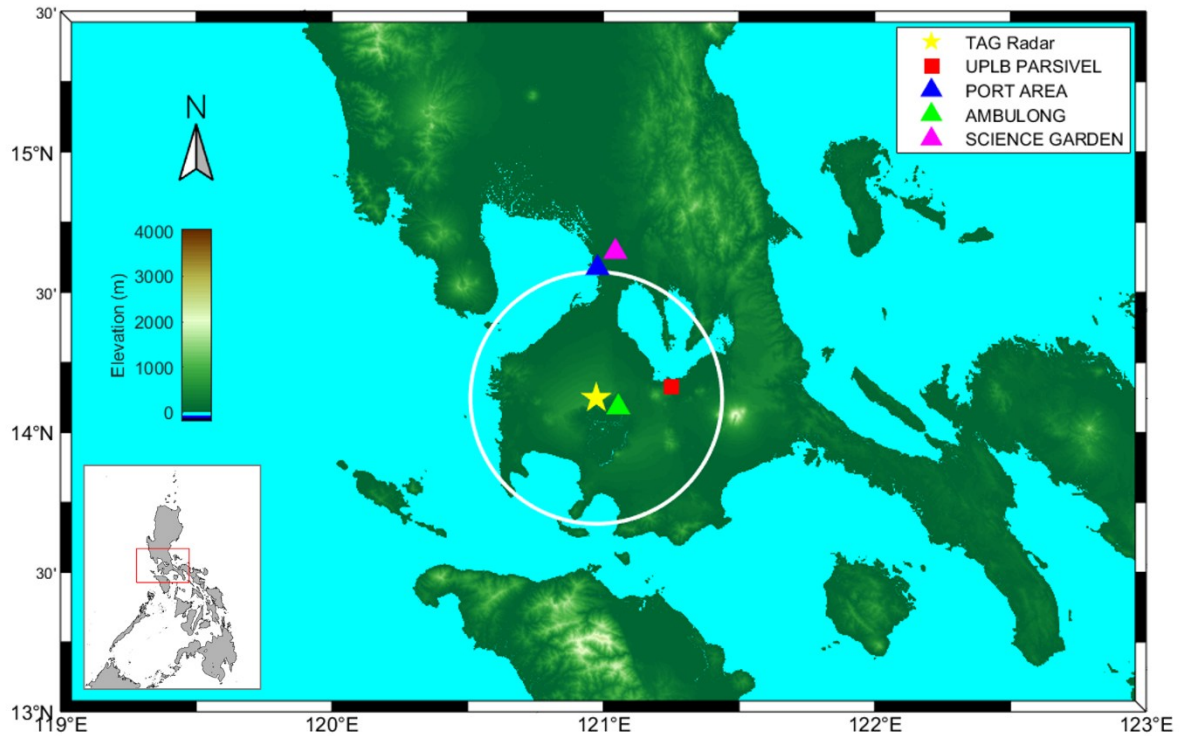


*Figure 2.1 Digital Elevation Map (DEM) of the area of study from the NASA Shuttle Radar Topography Mission (SRTM) (2013). The location of the Tagaytay weather radar is represented by the yellow star symbol, while the red box represents the site of the PARSIVEL disdrometer. The triangles are the locations of DOST-PAGASA synoptic stations: Port Area, Manila (blue), Ambulong, Batangas (green) and Science Garden in Quezon City (magenta).*

To ensure no contamination of rainfall events likely triggered or influenced by tropical cyclones (TC) in the analysis, all DSD data were subjected to a preliminary check to determine certain days likely affected by any synoptic event. TC and non-TC days were determined from the analysis. This is achieved by calculating the great circle distance between the disdrometer location and the eye or center of the TC. A day is considered a TC-day and excluded once any calculated 3-hour distance is less than 1000 kilometers. Such technique has been employed in earlier studies that discriminate among rainfall events (Bagtasa, Contribution of Tropical Cyclones to Rainfall in the Philippines, 2017). TC information was gathered from the National Oceanic and Atmospheric Administration International Best Track Archive for Climate Stewardship (NOAA IBTrACS) for the period of the study. The archive provides best track data every three hours. This preliminary check determined 113 (16%), out of the overall 677 days with available disdrometer data, are considered TC days. It should be noted that DSD samples in 2018 were reduced by about 18% after this initial check. A detailed description of this TC/non-TC classification is shown in Figure 2.2.

After the preliminary check, the QC process for the disdrometer data follows. Drops falling outside the 50% spread of the empirical diameter-velocity curve (Beard, 1976) are excluded (Figure 2.4a and 2.4b). This ensures that outliers are removed before processing and will not skew the results. Also, to address bias in the disdrometer data, daily accumulated rainfall calculated from both the station and the disdrometer are averaged and compared. A multiplication factor was applied to correct the one-minute DSD thereby removing the bias but retaining the shape of the DSD (Chang et al., 2020). The choice to utilize the daily accumulated rain instead of rainfall data with finer time resolution stemmed from the data issue observed in the retrieved surface observation data from the nearest automated weather stations (AWS). Figure 2.4c reveals a meager **0.14 dBR** bias between the station and the calculated rainfall from the disdrometer. This implies that the disdrometer overestimates rainfall albeit not that much. A rainfall threshold of 1 mm hr<sup>-1</sup> is used to sift through various rain rates with those less than this set threshold being excluded entirely in the analysis. A simple flow chart that details the QC process for the disdrometer data is shown in Figure 2.3.

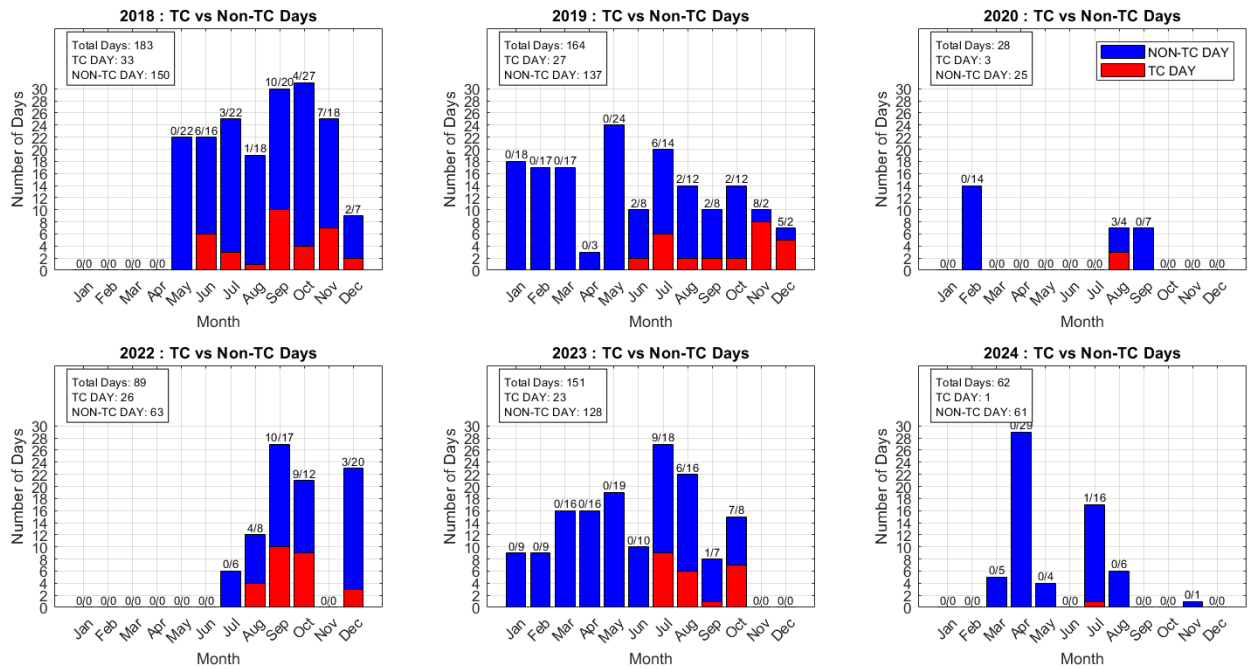


Figure 2.2 2018 to 2024 plots for TC vs non-TC days. Note that there is no data for 2021.



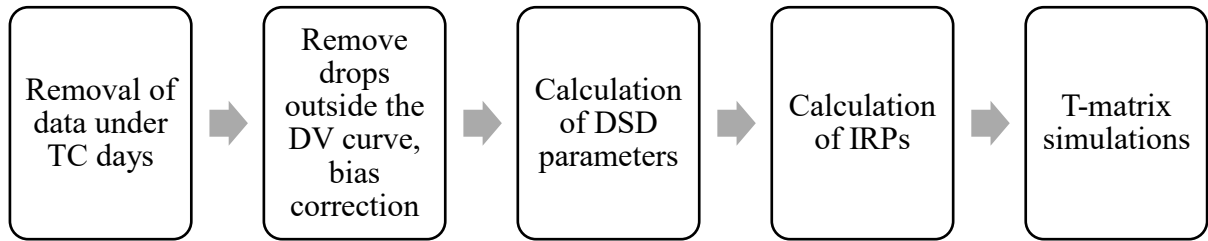


Figure 2.4 The quality control process implemented for the disdrometer data.

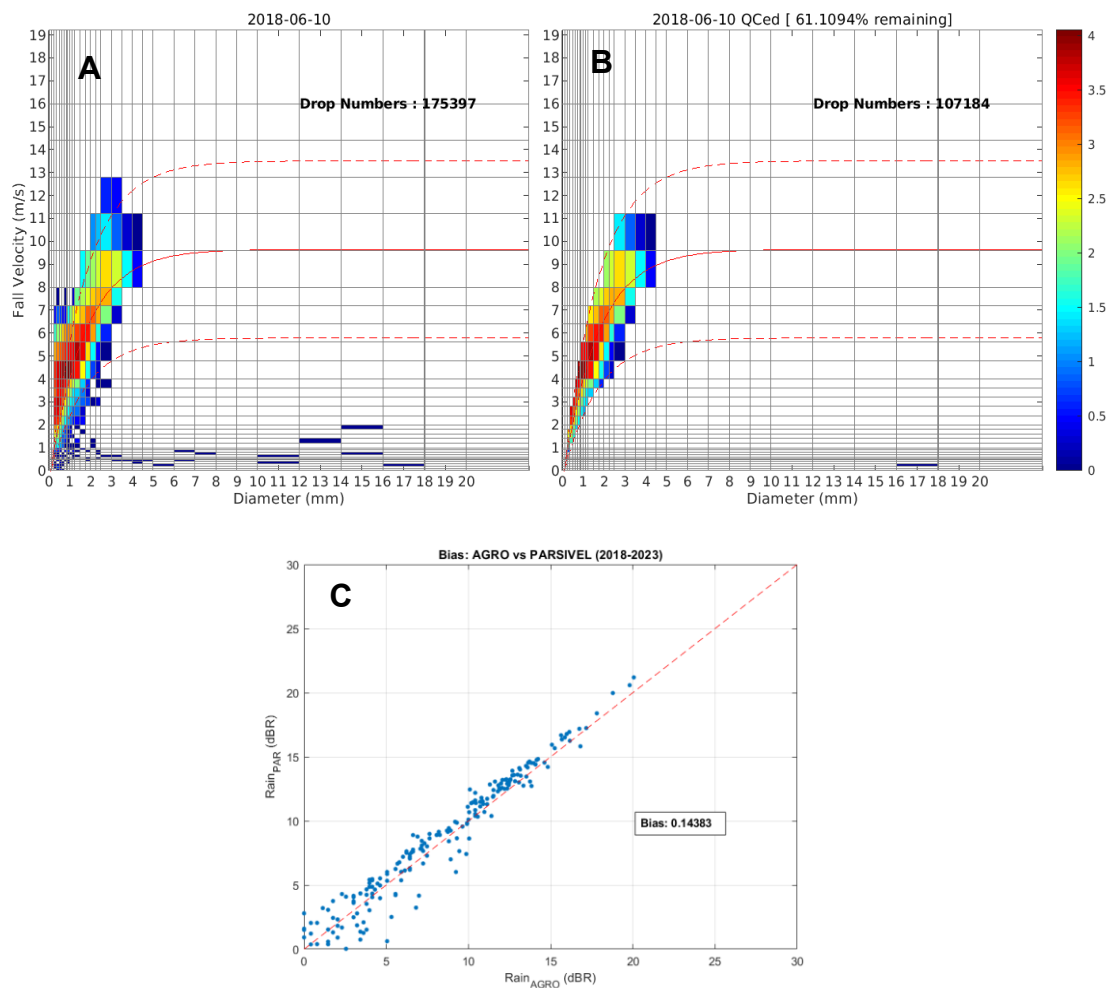


Figure 2.3 Sample DSD (a) before, and (b) after QC process, and (c) mean bias (dBR) calculated from observed rainfall vs calculated rainfall from disdrometer.

### 2.3 Calculation of DSD information and integral rainfall parameters

The number of raindrops per unit volume per unit volume-equivalent diameter is represented by  $N(D)$  ( $mm^{-1} m^{-3}$ ) in the form

$$N(D) = N_0 D^\mu \exp(-\Lambda D) \quad (1)$$

This gamma model of the DSD (Ulbrich, 1983) is characterized by the intercept  $N_0$  ( $mm^{-1} m^{-3}$ ), shape parameter  $\mu$  (dimensionless) and slope parameter  $\Lambda$  ( $mm^{-1}$ ). These parameters can be derived by calculating the integration of the third, fourth, and sixth moments of DSDs.

$$N_0 = \frac{\Lambda^{\mu+4} M_{3.67}}{\Gamma(\mu + 4)} \quad (2)$$

$$\mu = \frac{11G - 8\sqrt{G(G+8)}}{2(1-G)} \quad (3)$$

$$\Lambda = \frac{(\mu + 4)M_{3.67}}{M_4} \quad (4)$$

where

$$G = \frac{M_4^3}{M_{3.67}^2 M_6^1} \quad (5)$$

To derive the mass-weighted mean diameter  $D_m$  (mm), the third and fourth DSD moments are also used.

$$D_m = \frac{\mu + 4}{\Lambda} = \frac{M_4}{M_3} \quad (6)$$

To compare spectra with different LWC and  $D_m$ , normalization should be applied in such a way that the intrinsic shape of the DSD is not dependent on the said parameters. In this study, we use the normalized gamma distribution to illustrate the DSDs (Testud et al., 2001; Willis, 1984; Sekhon & Srivastana, 1971). The normalized intercept parameter  $N_w$  ( $mm^{-1} m^{-3}$ ) can be derived from

$$N_w = \frac{(4.0)^4}{\pi \rho_w} \left( \frac{10^3 LWC}{D_m^4} \right) \quad (7)$$

where  $\rho_w$  is the density of rainwater ( $1.0 \text{ g cm}^{-3}$ ) and  $LWC$  ( $\text{g m}^{-3}$ ) calculated from the DSD. The  $N_w$  parameter can be incorporated into the gamma distribution of DSDs and transform it to the normalized gamma distribution in the form

$$N(D) = N_w f(\mu) \left( \frac{D}{D_m} \right)^\mu \exp \left[ - (4.0 + \mu) \frac{D}{D_m} \right] \quad (8)$$

where

$$f(\mu) = \frac{6}{(4.0)^4} \frac{(4.0 + \mu)^{\mu+4}}{\Gamma(\mu + 4)} \quad (9)$$

In this study, using the DSD measured by the optical disdrometer, drop concentration per unit volume  $N(D_i)$  can be calculated through

$$N(D_i) = \sum_{i=1}^{32} \frac{n_i}{v(D_i) A t \Delta D_i} \quad (10)$$

where  $D_i$  is the drop diameter (mm) for the size bin  $i$ , drop fall velocity is represented by  $v(D_i)$ ,  $A$  is the sampling area,  $t$  is the sampling time and  $\Delta D_i$  (mm) is the corresponding diameter interval.

IRPs can be deduced from DSD information. The following equations are used to calculate rainfall rate  $R$  ( $\text{mm hr}^{-1}$ ),  $LWC$  ( $\text{g m}^{-3}$ ), total number concentration  $N_t$  ( $\text{m}^{-3}$ ), and reflectivity factor  $Z$  ( $\text{mm}^6 \text{ mm}^{-3}$ ) from DSD data.

$$R = 6\pi \times 10^{-4} \sum_{i=1}^{32} v(D_i) N(D_i) D_i^3 \Delta D_i \quad (11)$$

$$LWC = \frac{\pi}{6000} \sum_{i=1}^{32} N(D_i) D_i^3 \Delta D_i \quad (12)$$

$$N_t = \sum_{i=1}^{32} N(D_i) \Delta D_i \quad (13)$$

$$Z = \sum_{i=1}^{32} N(D_i) D_i^6 \Delta D_i \quad (14)$$

The mass spectrum standard deviation  $\sigma_m$  (mm), which is dependent on  $D_m$ , can be expressed using  $N(D)$  as presented by Williams et. al (2014). This parameter tells how close the masses of drops are from  $D_m$ . Low values usually pertain to stratiform rainfall, and high values are associated with convective precipitation due to mixed drop sizes.

$$\sigma_m = \frac{D_m}{\sqrt{4 + \mu}} = \left[ \frac{\sum_{D_{min}}^{D_{max}} (D - D_m)^2 N(D) D^3 dD}{\sum_{D_{min}}^{D_{max}} N(D) D^3 dD} \right] \quad (15)$$

The DSD and IRPs shown in this section are employed to analyze the microphysical characteristics of each precipitation type discussed in the study.

## 2.4 T-matrix scattering simulation

To calculate dual polarization parameters from DSD information, the T-matrix/Mueller scattering simulation method, which was first introduced by Waterman (1971), was used. This method calculates electromagnetic scattering of non-spherical particles. Parameters such as radar wavelength, elevation angle, axis ratio, and environmental temperature are needed to simulate radar parameters. The axis ratio is assumed to be oblate and follows the raindrop shape model proposed by Brandes et. al. (2002) which can be expressed as a fourth-order polynomial equation:

$$\gamma = 0.9951 + 0.0251D + 0.03644D^2 + 0.00503D^3 - 0.0002492D^4 \quad (16)$$

where  $\gamma$  is the axis ratio (vertical axis divided by the horizontal axis) and  $D$  is the equivalent-volume drop diameter (mm). Diameter range is set to 0.01 mm to 10 mm at 0.01 mm intervals.

Compared to previous studies (Macuroy et al., 2021; Ibañez et al., 2023; Aragon et al., 2024), this study set the environmental temperature to 28.4°C for the SWM season which was based on the averaged 1991-2020 climatological normal of the DOST-PAGASA synoptic stations near the domain (see Table 2.3): (a) *Science Garden in Quezon City*, (b) *Port Area, Manila*, and (c) *Ambulong station in Batangas Province*. This value is much higher than the 20°C initially set by these earlier studies. It can be noted that attenuation is sensitive to temperature variability (Jameson, 1992), so it is crucial to set near realistic values. Variations in attenuation coefficients due to temperature variability was also clearly shown in the work of Loh et. al. (2022) highlighting the importance of simulating radar parameters with realistic temperature values. The details on the full control conditions are summarized in Table 2.2.



Table 2.2 Control conditions for T-matrix scattering simulations used to retrieve polarimetric variables from disdrometer data.

T-matrix control condition	Value
Radar wavelength	5.3 cm
Radar elevation angle	0°
Hydrometeor type	Rain
Environmental temperature	28.4 °C
Raindrop shape model	Brandes et. al. (2002)
Diameter range	0.1 mm to 10 mm
Diameter interval	0.1 mm

Table 2.3 Monthly (*mon\_ave*) and seasonal (*swm\_ave*) average temperature (°C) from three synoptic stations near the domain based on 1991-2020 climatological normals (DOST-PAGASA, n.d.). Science Garden and Port Area are located north of the domain in Quezon City and City of Manila, respectively. Ambulong station is located in the Province of Batangas which is south of the domain.

Month	Stations			Average	
	Science Garden	Ambulong	Port Area	<i>mon_ave</i>	<i>swm_ave</i>
June	29.1	28.7	29.7	29.17	28.4
July	28.2	27.8	28.7	28.23	
August	27.9	27.7	28.5	28.03	
September	27.9	27.8	28.4	28.03	

## 2.5 Tagaytay C-band weather radar data and quality control procedures

For this study, radar data from the 2018 SWM season was utilized. Initial inspection of the raw radar data revealed the following problems: (1) *inconsistency of  $\Phi_{DP}$  values at or near the radar site*, (2)  *$\Phi_{DP}$  folding*, (3) *severe attenuation especially for cases of heavy rainfall*, and (4) *huge area of negative  $Z_{DR}$  values* (see Figure 2.6). Due to these identified data issues, a comprehensive QC procedure must be done.

An earlier study on this same radar noted serious hardware miscalibration which prompted recalibration of reflectivity using self-consistency techniques (Crisologo et al., 2014). The QC procedures implemented are shown in Figure 2.5 and is mostly based on the work of Loh et. al. (2022) who assessed the reflectivity biases and wet-radome effect of collocated S- and C-band radars in Taiwan.

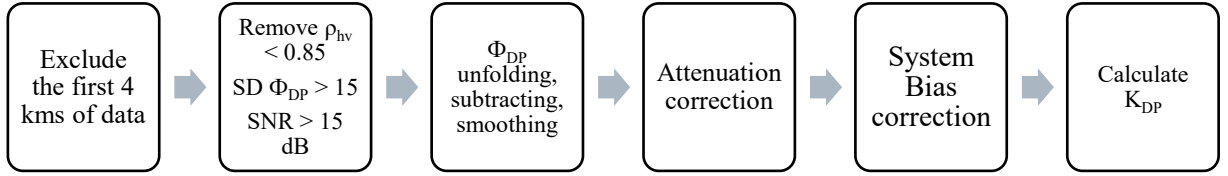


Figure 2.5 The quality control process implemented for the Tagaytay weather radar data.

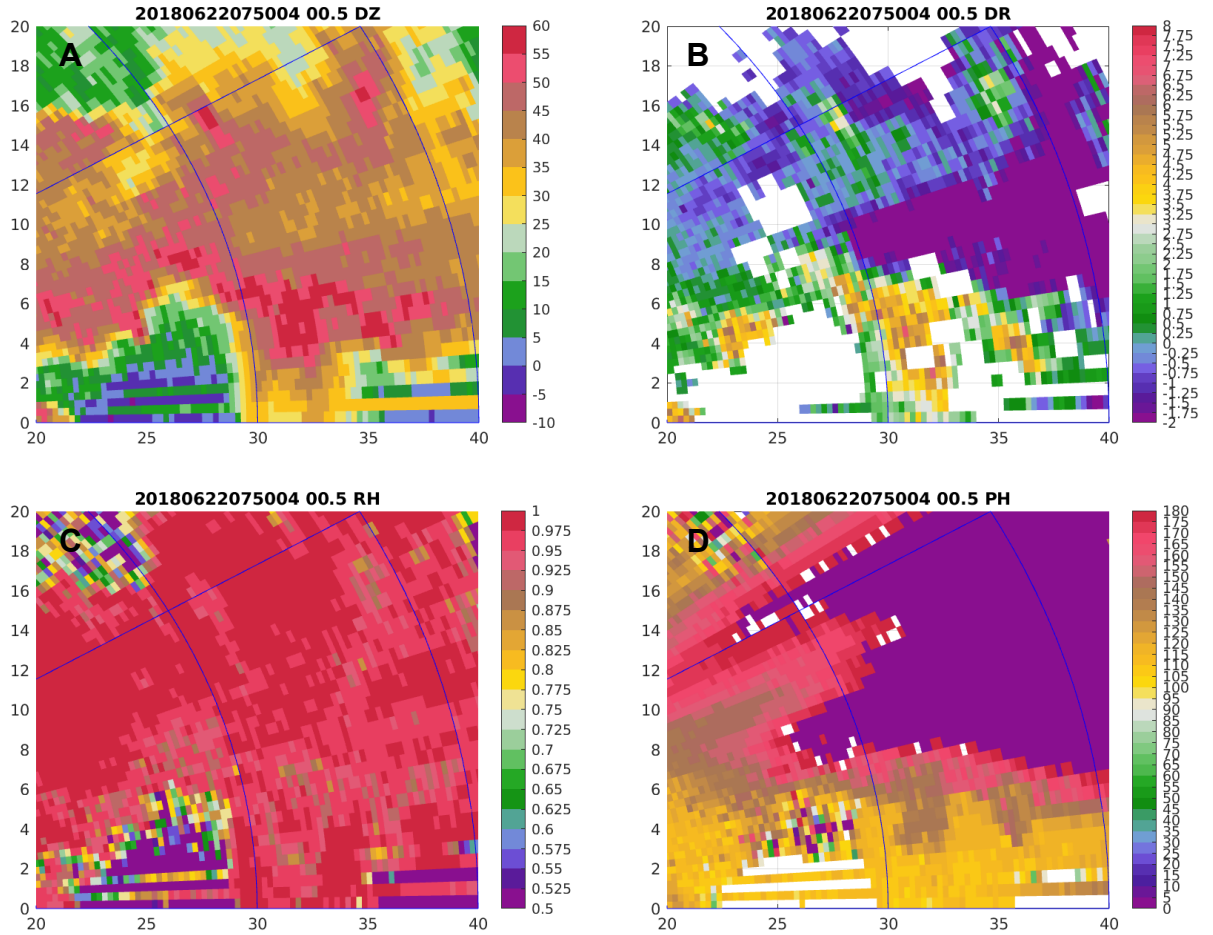


Figure 2.6 Sample raw PPI plots for (a)  $Z_H$ , (b)  $Z_{DR}$ , (c)  $\rho_{HV}$ , and (d)  $\Phi_{DP}$  showing issues that need to be addressed in the QC process. The x- and y-axis are range in kilometers.

### 2.5.1 $\Phi_{DP}$ processing

Differential phase shift ( $\Phi_{DP}$ ; °) is a radar parameter that measures the phase difference between horizontally and vertically polarized waves as it moves through a medium such as rain (Carey et al., 2000). This parameter usually increases monotonically with range under rainfall conditions. However, once it exceeds its maximum unambiguous value, folding or wrapping can occur. Strong rainfall events are severely affected by folding thus the unfolding process of the  $\Phi_{DP}$  is applied to the data.

Upon inspection, it can be observed that  $\Phi_{DP}$  values at or near the radar site are inconsistent, hence warranting the decision to exclude the nearest four kilometers of data. This step is crucial since  $\Phi_{DP}$  is subtracted from the initial values ( $\Phi_{DP}^0$ , or  $\Phi_0$ ) (Jameson, 1991) to obtain  $\Delta\Phi_{DP}$ , which is used for attenuation correction in the later part of the QC process. After these processes, smoothing of  $\Phi_{DP}$  is done.

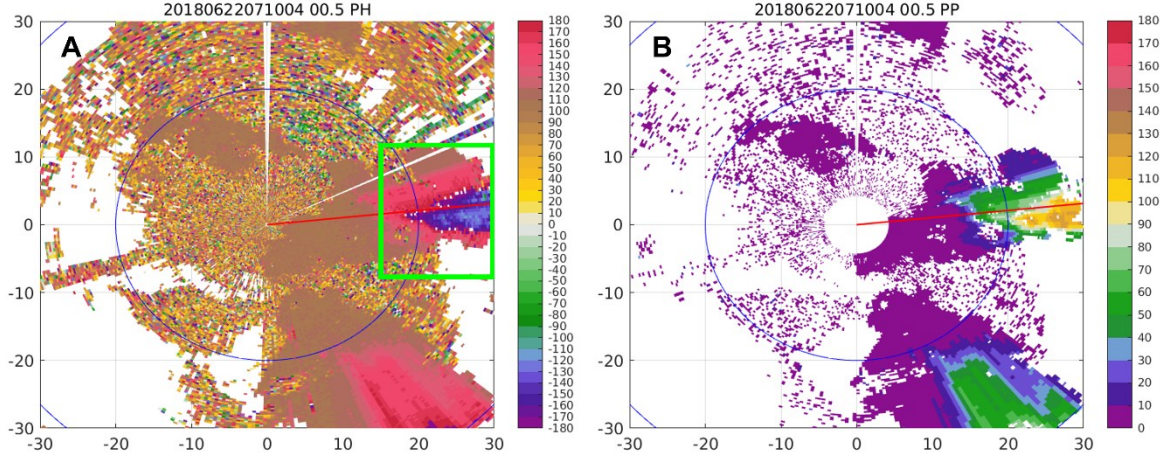


Figure 2.7  $\Phi_{DP}$  processing for Tagaytay C-band radar data. (a)  $\Phi_{DP}$  raw data and (b)  $\Phi_{DP}$  after unfolding. Green box is the area of folding shown by the abrupt shift from positive values to negative values.

### 2.5.2 Removal of noise and non-meteorological signals

Once issues with  $\Phi_{DP}$  have been addressed, removal of noise and non-meteorological signals follows. Crisologo et. al. (2014), working on the same radar, addressed these signals through fuzzy logic classification which was initially presented by Vulpiani et. al. (2012). A recent study by Lin et al. (2021) also made use of the fuzzy logic approach to remove these signals using three radars in the Philippine radar network such as Hinatuan, Mactan and Tagaytay.

A simpler approach to addressing these unwanted signals has been implemented for the current radar data set. This is done though using the co-polar cross correlation coefficient ( $\rho_{hv}$ ) and setting the threshold to 0.85. In rainfall, it is known that  $\rho_{hv}$  values range from 0.98 to 1. Setting the threshold of  $\leq 0.85$  efficiently excludes non-uniform scatterers such as ground and sea clutters, biological scatterer and anomalous propagation. Following this step is the removal of noise by using the standard deviation of  $\Phi_{DP}$  ( $\sigma\Phi_{DP}$ ) of five neighboring gates. Where the  $\sigma\Phi_{DP} > 20^\circ$ , data is thereby excluded. Finally, signal-to-noise ratio (SNR) of less than 15 dB is also eliminated to ensure that the data only captures meteorological signals.

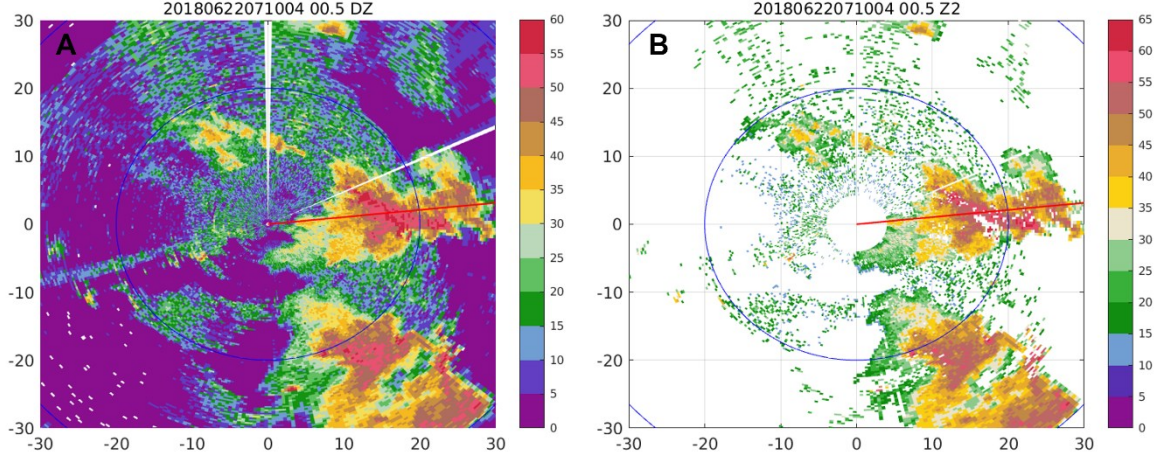


Figure 2.8 Removing non-meteorological signals for Tagaytay C-band radar data. (a)  $Z_H$  raw data and (b)  $Z_H$  after  $\rho_{hv}$  and  $\sigma\Phi_{DP}$  thresholds were applied.

### 2.5.3 Attenuation correction

As observed in the radar raw plots, especially for strong convective precipitation, the data suffered from severe attenuation appearing like a ‘shadow’ after a region of increased  $Z_H$  and  $Z_{DR}$  values (see Figure 2.6a-b). Attenuation is known to become increasingly serious especially for radar wavelengths,  $\lambda$ , below 10 cm (Smyth & Illingworth, 1998). This issue is not unexpected since this has been observed in most operational C-band radars. Thus, before the data can be used and proper analysis can be done, the attenuated radar measurements should be corrected.

Generally, attenuation can be effectively estimated through specific differential phase ( $K_{DP}$ ;  $^{\circ}\text{km}^{-1}$ ) since this radar parameter is relatively unaffected by system biases, antenna and receiver gain factors, attenuation, power calibration, partial beam blockage, and less sensitive to the DSD variability (Chang et al., 2014; Loh et al., 2022; Ryzhkov & Zrnice, 1996). Added to this advantage is the linear relationship of  $K_{DP}$  to both the one-way specific attenuation ( $A_H$ ;  $\text{dB km}^{-1}$ ) and differential attenuation ( $A_{DP}$ ;  $\text{dB km}^{-1}$ ) as shown in the work of Bringi et. al. (1990).

Recalling that the  $\Phi_{DP}$  is twice the sum of  $K_{DP}$  over a specified range, we can use the  $\Phi_{DP}$ -based method (Bringi et al., 1990) to estimate the path-integrated attenuation (PIA) and differential attenuation (PIDA) using the increments of  $\Phi_{DP}$  in precipitation.

$$PIA = \alpha \times \Delta\phi_{DP} \quad (17)$$

$$PIDA = \beta \times \Delta\phi_{DP} \quad (18)$$

where  $\Delta\phi_{DP}$  is the increment of observed  $\phi_{DP}$  and the coefficients  $\alpha$  and  $\beta$  are in  $\text{dBZ km}^{-1}$ .

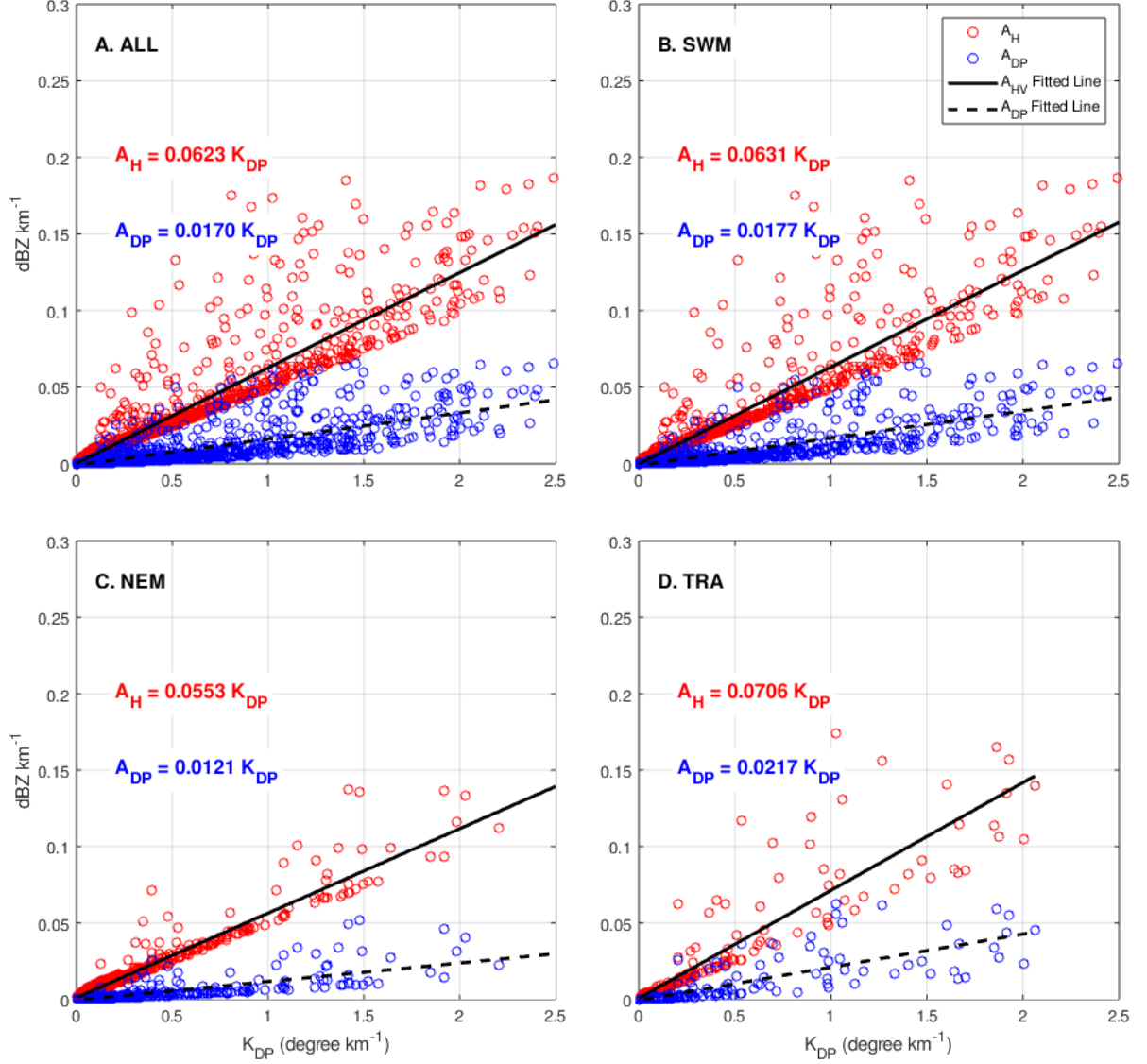


Figure 2.9 Attenuation coefficients ( $\alpha$  and  $\beta$ ) derived from fitting  $K_{DP}-A_H$  and  $K_{DP}-A_{DP}$  respectively for (a) all season data, (b) SWM, (c) NEM, and (d) transition months (TRA).

For this study, using the available DSD data from 2018 to 2024, attenuation coefficients  $\alpha$  and  $\beta$  are calculated using least squares fitting of  $K_{DP}-A_H$  and  $K_{DP}-A_{DP}$  for (a) all season, (b) SWM, (c) NEM and (d) TRA as shown in Figure 2.9 and Table 2.4. Using these attenuation coefficients and the calculated PIA and PIDA,  $Z_H$  and  $Z_{DR}$  can then be corrected as follows:

$$Z_H^{cor} = Z_H + PIA \quad (19)$$



$$Z_{DR}^{cor} = Z_{DR} + PIDA \quad (20)$$

where  $Z_H^{cor}$  is the corrected  $Z_H$  and  $Z_{DR}^{cor}$  is the corrected  $Z_{DR}$ . Table 2.4 shows the attenuation coefficients calculated for SWM, NEM, TRA and all season.

Table 2.4 Attenuation coefficients calculated through least-squares fitting of  $K_{DP}-A_H$  and  $K_{DP}-A_{DP}$ .

Attenuation coefficients	ALL	SWM	NEM	TRA
$\alpha$	0.0623	0.0631	0.0553	0.0706
$\beta$	0.0170	0.0177	0.0121	0.0217

#### 2.5.4 $Z_{DR}$ system bias correction

To further address the issue with the regions of negative  $Z_{DR}$ , correction of system bias follows attenuation correction.  $Z_{DR}$  system bias is determined through vertical pointing radar assuming that the shape of raindrops at  $90^\circ$  are nearly circular (Vivekanandan et al., 2003). However, this can be quite a challenge since most operational radars cannot scan vertically. Smyth and Illingworth (1998) suggests using data from weak echo regions or reflectivity from regions of light rain. In principle, rain drops in these regions are expected to be nearly spherical.

In this study, to calculate for the  $Z_{DR}$  system bias, the following characteristics are used to classify regions of light rain:

- a)  $\rho_{HV} > 0.95$
- b)  $15 \text{ dBZ} \leq Z_H \leq 25 \text{ dBZ}$
- c)  $\Delta\Phi_{DP} < 15^\circ \text{ km}^{-1}$
- d) altitude: below 4 km (to avoid freezing level)
- e) completely exclude beams with blockages

Most of these parameters also appeared in Macuroy et. al. (2021) albeit the slight differences in values. The mean  $Z_{DR}$  from radar,  $Z_{DR}^{rad}$  is calculated from all beams for all elevation angles. The same averaged  $Z_{DR}$  is calculated from 2018-2014 disdrometer data,  $Z_{DR}^{par}$ . Finally, these values are then used to calculate the  $Z_{DR}$  system bias using the equation:

$$Z_{DR}^{sys} \text{Bias} = \text{mean } Z_{DR}^{rad} - \text{mean } Z_{DR}^{par} \quad (21)$$

## 2.6 Time-height plots of averaged dual polarization parameters

After all the QC steps has been completed, generating time-height plots of  $Z_H$ ,  $Z_{DR}$ ,  $K_{DP}$ , and  $\rho_{HV}$  over the disdrometer site follows. These plots are used to examine the averaged vertical

profile over the disdrometer site during selected rainfall events. This is done by setting a 10 km by 10 km area, with the disdrometer at the center. Values within the selected area are averaged for every level with 0.25 km vertical resolution. While averaging values is expected to lessen or dampen the magnitude of the parameters, it should still adequately capture the dominant features of precipitation systems that passed through the site.

## 2.7 Principal component analysis on DSD data

To provide an in-depth analysis on the microphysical characteristics and its corresponding transitions within the precipitation system, we employ the principal component analysis (PCA) to study the current DSD data. The methods and processes applied here are based on DO18, who studied global DSD datasets and determined PCA clusters which corresponds to dominant microphysical process as verified by the matched disdrometer and radar data. This study made use of the same parameters as the DO18's study, such as  $\log_{10}N_w$ ,  $D_m$ ,  $\sigma_m$ ,  $\log LWC$ ,  $\log R$ , and  $\log N_t$ . These DSD parameters were chosen because they describe the DSD itself and its variability. The same threshold of  $\pm 1.5$  is applied to determine the PCA groups, however, it should be noted that this threshold is arbitrary and that increasing (decreasing) this value decreases (increases) the overlap between clusters. DO18 determined seven PCA groups (PGs), with the six groups corresponding to either convective and stratiform processes and the one set as ambiguous (AMB) since multiple principal components overlap with this group. The characteristics of each group is shown and summarized in Table 2.5.

Table 2.5 PCA group characteristics based on Dolan et. al (2018).

PCA group	Characteristics
1	<i>Convective</i> . PG has components of both warm and ice-based processes and conforms with the Bringi et. al. (2009), henceforth BR09, convective-stratiform (C/S) separation line.
2	<i>Stratiform</i> . This PG corresponds to weak stratiform precipitation with small to mid-sized drops. Increasing $D_m$ and $\log_{10}N_w$ correlates to increasing bright band (BB) intensity ( $\sim 20$ to $25$ dBZ). Melted vapor-grown particles leads to aggregation and riming.
3	<i>Convective</i> . Shallow weak convection. Numerous but small drops, shallow echo top height and generally weak reflectivities. Associated with weak convective motions (tropics) or orographic enhancement.
4	<i>Stratiform</i> . Characterized by larger drops but low $\log_{10}N_w$ values compared to PG2. BB reflectivity reaches $>30$ dBZ.

5	<i>Convective</i> . Dominated by warm rain processes especially in deep convection. Collision-coalescence process leads to growth of drops. Conforms the BR09 CS separation line.
6	<i>Convective</i> . Ice-based convective precipitation. Melting of graupel and hail results to large drops at the surface. Conforms the BR09 C/S separation line.
<i>AMB</i>	DSDs that overlaps with multiple PCs and thus excluded from analysis.

## 2.8 Selection and description of case studies

To facilitate the detailed examination of rainfall events and the related microphysical characteristics and mechanisms, a list of possible case studies has been created through matching both the available disdrometer and radar data. Continuous rainfall events were considered when the time gap between  $R$  is less than or equal to 10 minutes. Rainfall events with time gaps exceeding this set threshold are considered entirely different rainfall events. This threshold allows efficient isolation of rainfall events especially for days with multiple rainfall events observed. Rainfall events with recorded rainfall durations less than 10 minutes were excluded further since the Tagaytay radar scans only every 10 minutes. Including these short-lived rainfall events in the analysis can be quite challenging given the limitations with the data available. The remaining possible rainfall event cases were individually checked against the available time-height averaged vertical profile of dual polarization parameters such as  $Z_H$ ,  $Z_{DR}$ ,  $K_{DP}$  and  $\rho_{HV}$ .

From the viable 2018 data, a total of 42 (48%) were identified from the pool of 88 rainfall events (Figure 2.10a). These were further classified into four types: *strong widespread convection (SWC)*, *strong isolated convection (SIC)*, *weak shallow convection (WC)* and *weak stratiform (WS)*. These classifications were based on the earlier work of Thompson et. al. (2015), hereafter TH15, which grouped rainfall events from tropical oceanic datasets obtained from Manus and Gan Island. About 37% of the cases are WS, while SWC cases are around the same at 36%. WC and SIC are about 17% and 10% of the cases respectively.

## 2.9 Contoured Frequency by Altitude Diagrams (CFAD) per PCA group

To further explore the relationship between the averaged vertical profiles and the disdrometer observations, both radar and DSD data were time matched to create contoured frequency by altitude diagrams (CFADs) of  $Z_H$ ,  $Z_{DR}$  and  $K_{DP}$  for each PGs.

It can be recalled that the DSD data has a 1-min time resolution while the radar scans every 10 minutes. These differences in time resolution can be quite a challenge when comparing both data thereby creating a dilemma in selecting the PCA group to represent each radar vertical profile since in one radar time stamp can have multiple PGs. To address this, 10-mins worth of PGs per identified radar scan time were examined and the PG with the most dominant DSDs were chosen to represent the radar vertical profile for that same time range. This stringent threshold, however, threatens to further decrease radar samples for DSD groups such as PG5 and PG6 which has relatively lesser samples compared to other PGs. With this, for PG5 and PG6, once DSD samples contain at least 3 of these they will automatically be represented by such PGs.

Excluding the ambiguous groups (PG7) from the analysis, a total of 131 DSD-radar samples were identified (Figure 2.10b) with 31% (40) and 26% (34) representing PG1 and PG2 respectively. This is followed by PG4 at 21% (27) and PG3 at 14% (19). PG5 and PG6 trailed behind with fewer samples at 3% (4) and 5% (7). The radar vertical profiles for each PG were combined to create a CFAD to facilitate the joint analysis of both DSD and radar data.

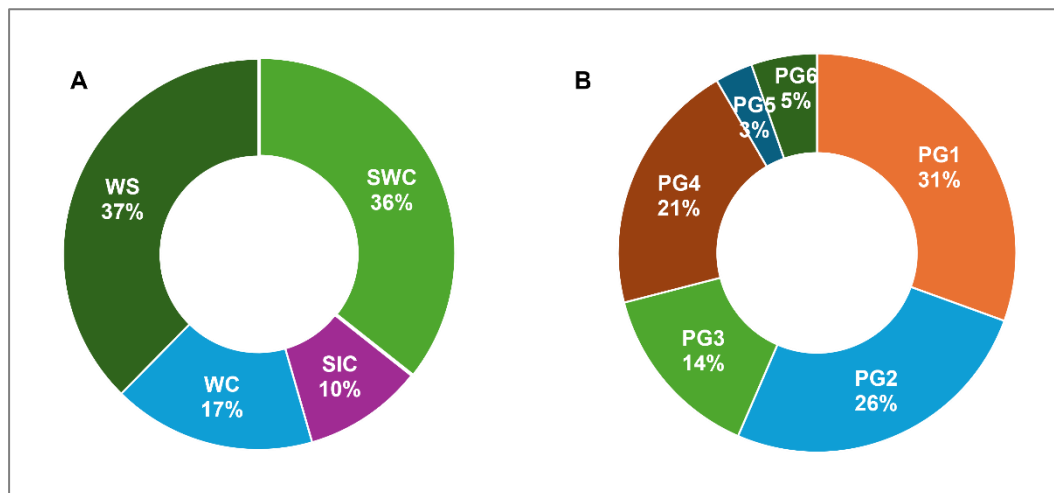


Figure 2.10 Pie charts for precipitation type classification and the identified DSD-radar samples. (a) precipitation types, and (b) DSD groups

## Chapter 3 RESULTS AND DISCUSSIONS

This chapter discusses in detail the results from the methods of analysis laid out in the previous chapter. This includes the variability of the DSD across seasons while putting emphasis on the SWM, changes in the microphysical characteristics of DSD during the rain event shown in the  $\log_{10}N_W$ - $D_m$  and  $LWC$ - $D_m$  plane, and the modes of DSD revealed by the PCA matched with the averaged time-height profiles of radar dual polarization variables. To compare the general characteristics of the precipitation types in terms of radar parameters, pseudo range-height indicator (PRHI) plots and CFAD are also presented.

### 3.1 Seasonal variation of DSD in South Luzon

To show variations of DSDs across seasons  $\log_{10}N_W$ - $D_m$  plots were generated from the 2018-2024 data. Around 60% of the dataset are from the SWM season, hence, enough data to represent this season. For the general purpose of discussion, we compare the DSDs between these seasons shown in Figure 3.1.

The frequency distribution  $\log_{10}N_W$ - $D_m$  plots (Figure 3.1a-d) generally shows that most of the DSD fall below the BR09 separation line, thus most rainfalls are classified as stratiform. Average values for  $D_m$  for SWM and TRA are bigger than the all-season average, while NEM generally has almost the same average  $\log_{10}N_W$  value compared with the all-season average (see Table 3.1). For all season,  $\log_{10}N_W$  values are around  $3.7 \text{ mm}^{-1} \text{ m}^{-3}$  with  $D_m$  values at 1.7 mm. For SWM, mean value for  $\log_{10}N_W$  is at  $3.3 \text{ mm}^{-1} \text{ m}^{-3}$ , which is lower than the all-season average and the NEM average ( $3.7 \text{ mm}^{-1} \text{ m}^{-3}$ ). However, the  $D_m$  average for SWM is the highest recorded at 1.8 mm, followed by TRA at 1.7 mm with NEM trailing behind at 1.4 mm. This is not unexpected for NEM since most of the rainfall recorded from this season falls under stratiform. The average values for these parameters are lower, though not very significant, compared to those determined by Aragon et. al. (2024). Figure 3.1e-h reveals much more details as DSDs are classified into convective and stratiform groups. This is done by simply applying the  $R > 10 \text{ mm hr}^{-1}$  threshold to consider a DSD as convection. The plots show that convective and stratiform mean for both SWM and TRA are close to the continental cluster (CT) introduced by Bringi et. al (2003). The NEM mean values, on the other hand, is much closer to the maritime cluster (MT), which is characterized by high concentration of relatively small drops. This is consistent with initial findings such as that of Ibañez et al. (2022) and Aragon et. al (2024).

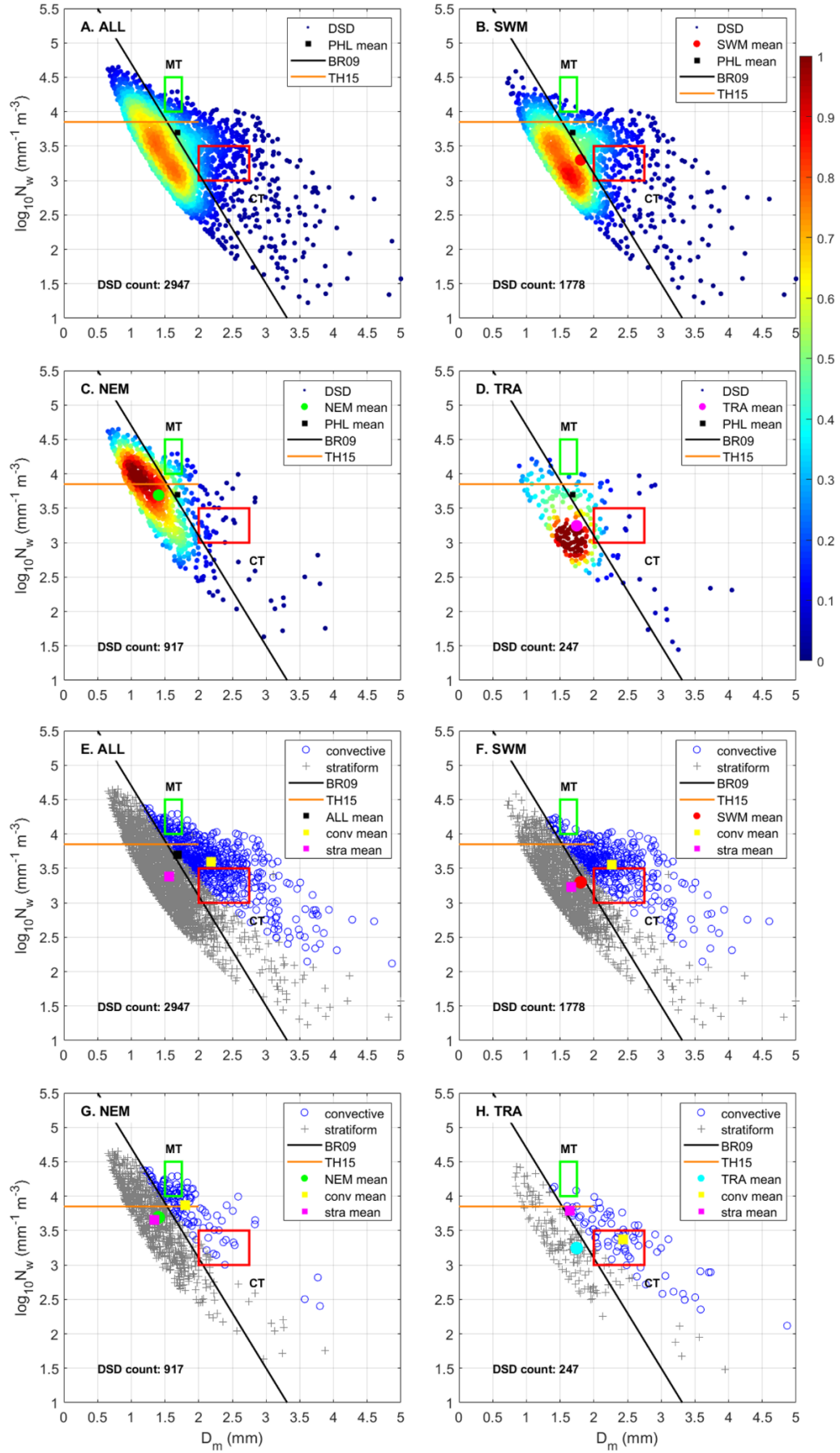


Figure 3.1 Frequency distribution of DSD in  $\log_{10}N_w$ - $D_m$  plane (a-d), C/S classification (e-h). (a, d) all data, (b, f) SWM, (c, g) NEM, and (d, h) transition months



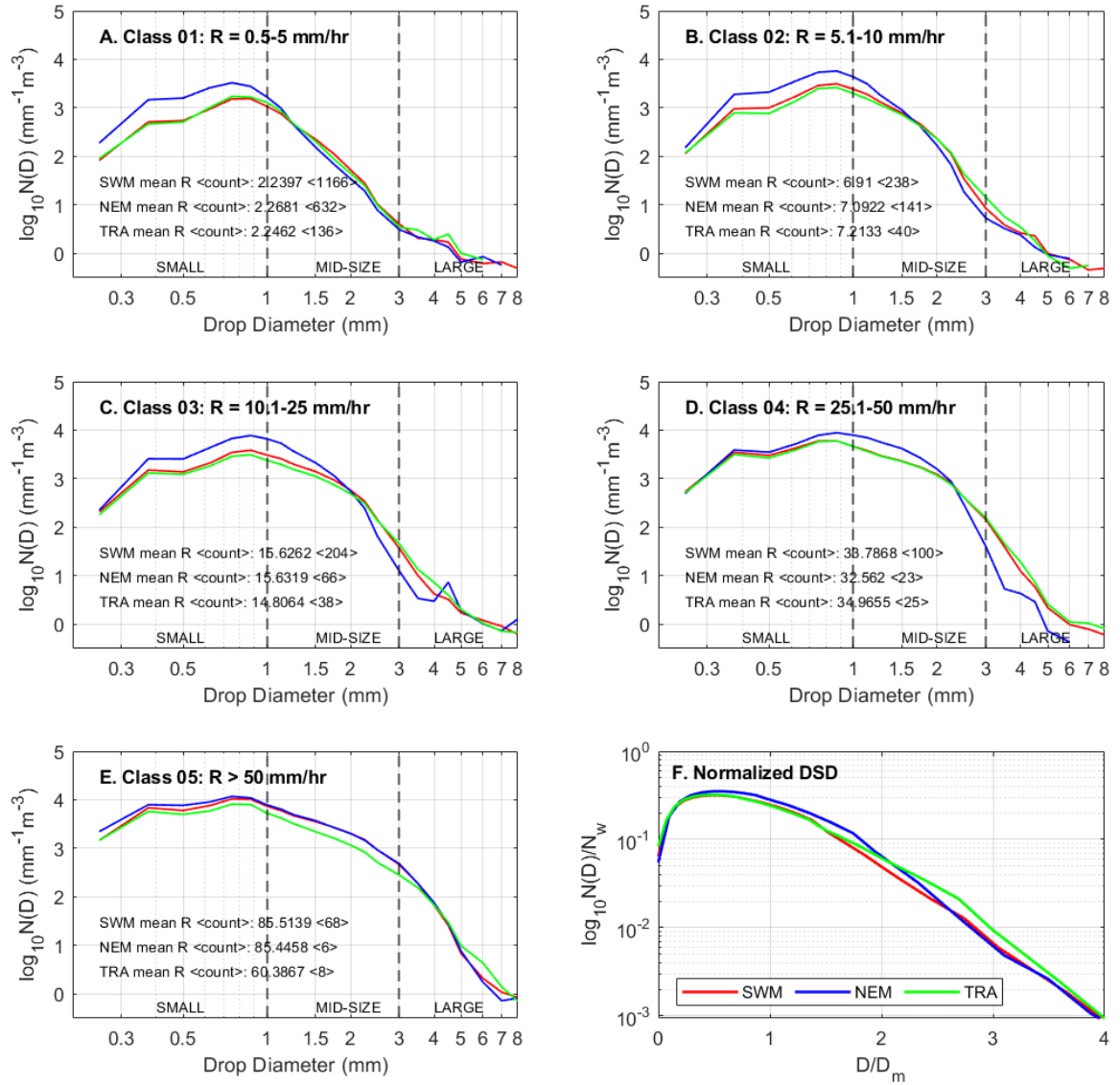


Figure 3.2 Averaged seasonal DSD per rain rate classes. (a) Class 1, (b) Class 2, (c) Class 3, (d) Class 4, (e) Class 5, and (f) normalized DSD. Red represents SWM, blue represents NEM and TRA shown in green. Values presented in the plot are mean  $R$  and count per season per rain rate class.

To further investigate the differences in DSD characteristics between the seasons,  $N(D)$  and  $D_m$  are examined by grouping DSD into various  $R$  classes (Figure 3.2a-e). In this study, five  $R$  classes were determined (Class 1:  $R = 0.5-5$  mm hr<sup>-1</sup>; Class 2:  $R = 5.1-10$  mm hr<sup>-1</sup>; Class 3:  $R = 10.1-25$  mm hr<sup>-1</sup>; Class 4:  $R = 25.1-50$  mm hr<sup>-1</sup>, and Class 5:  $R > 50$  mm hr<sup>-1</sup>). This  $R$  classification was adapted from previous research (Seela et al., 2017; Aragon et al., 2024) but was modified for this study due to the number of DSD samples available. Classification of drops to small (0-1 mm), mid-size (1-3 mm) and large ( $>3$  mm) drops were also adapted. Regardless of the  $R$  class, it can be clearly seen that for small drops (0-1 mm), NEM has the highest concentration compared to the other seasons. For mid-sized to large drops, specifically  $\geq 2.5$  mm, SWM and TRA has much higher concentration. This difference can be clearly seen in classes with higher  $R$  specifically classes 3 and 4.

To further examine the DSD variability across different rain types and seasons, normalization of DSD (Testud et al., 2001) was applied (Figure 3.2f). Unlike the results from Aragon et al. (2024) which observed that variability of DSD is mostly noted at  $D/D_m < 0.4$ , there is a clear deviation of DSDs between the seasons for South Luzon at around  $D/D_m = 1.5$ . It can also be noted that both SWM and NEM converged again at  $D/D_m = 2.5$ . This suggests that the microphysical processes that dictates the surface DSDs is present in both SWM and NEM. Among the seasons, TRA showed more variance, however, this can be attributed to the limited samples for this season compared to the previous two seasons.

Table 3.1 Average values of  $\log_{10}N_W$  and  $D_m$  from 2018-2024 disdrometer data for across seasons. *C* refers to convective, *S* for stratiform and *ave* for average values.

	ALL			SWM			NEM			TRA		
	<i>ave</i>	<i>C</i>	<i>S</i>	<i>ave</i>	<i>C</i>	<i>S</i>	<i>ave</i>	<i>C</i>	<i>S</i>	<i>ave</i>	<i>C</i>	<i>S</i>
$\log_{10}N_W$ ( $\text{mm}^{-1} \text{m}^{-3}$ )	3.7	3.6	3.4	3.3	3.4	3.2	3.7	3.9	3.7	3.2	3.4	3.8
$D_m$ (mm)	1.7	2.2	1.6	1.8	2.3	1.6	1.4	1.8	1.3	1.7	2.4	1.6

### 3.2 Modes of DSD

To conform with the established primary modes of DSD from DO18, this study also examined the DSDs from the current data using the PCA. Figure 3.3a shows the DSD clusters revealed by plotting the standard anomalies of principal component (PC) 1 against PC2. The combined variances of these two PCs are about 95%, which means that both the primary PCs describes most of the variances in the DSD. These clusters of DSDs are shown in different planes such as  $\log_{10}N_W$ - $D_m$  (Figure 3.3b),  $\log LWC$ - $D_m$  (Figure 3.3c), and  $R$ - $Z_H$  (Figure 3.3d). It can be observed that most of the DSDs (39%) were below the set threshold ( $|1.5|$ ) and are thus considered AMB. This is followed by PG2 at 20%, PG3 at 15%, and PG1 at 13%. The remaining PGs (4, 5 and 6) were much lesser at 7%, 2% and 3% respectively. These DSDs color-coded by the PG are plotted to match the radar averaged time-height plots in a later section.

It can be noted that compared to DO18, PG3 of the current study does not have a wider scatter of DSDs towards positive PC2 standard anomaly compared DO18. We infer that this is because of the abundance of shallow convection observed from DO18's tropics dataset. To recall, DO18's dataset to describe the DSDs in the tropics is composed of the combined disdrometer observations from three locations: Manus Island in Papua New Guinea, Gan Island in Maldives, and Darwin, Australia. It can also be recalled further that Manus and Gan Island datasets were used to explain the DSD characteristics in a tropical oceanic regime (TH15) thus

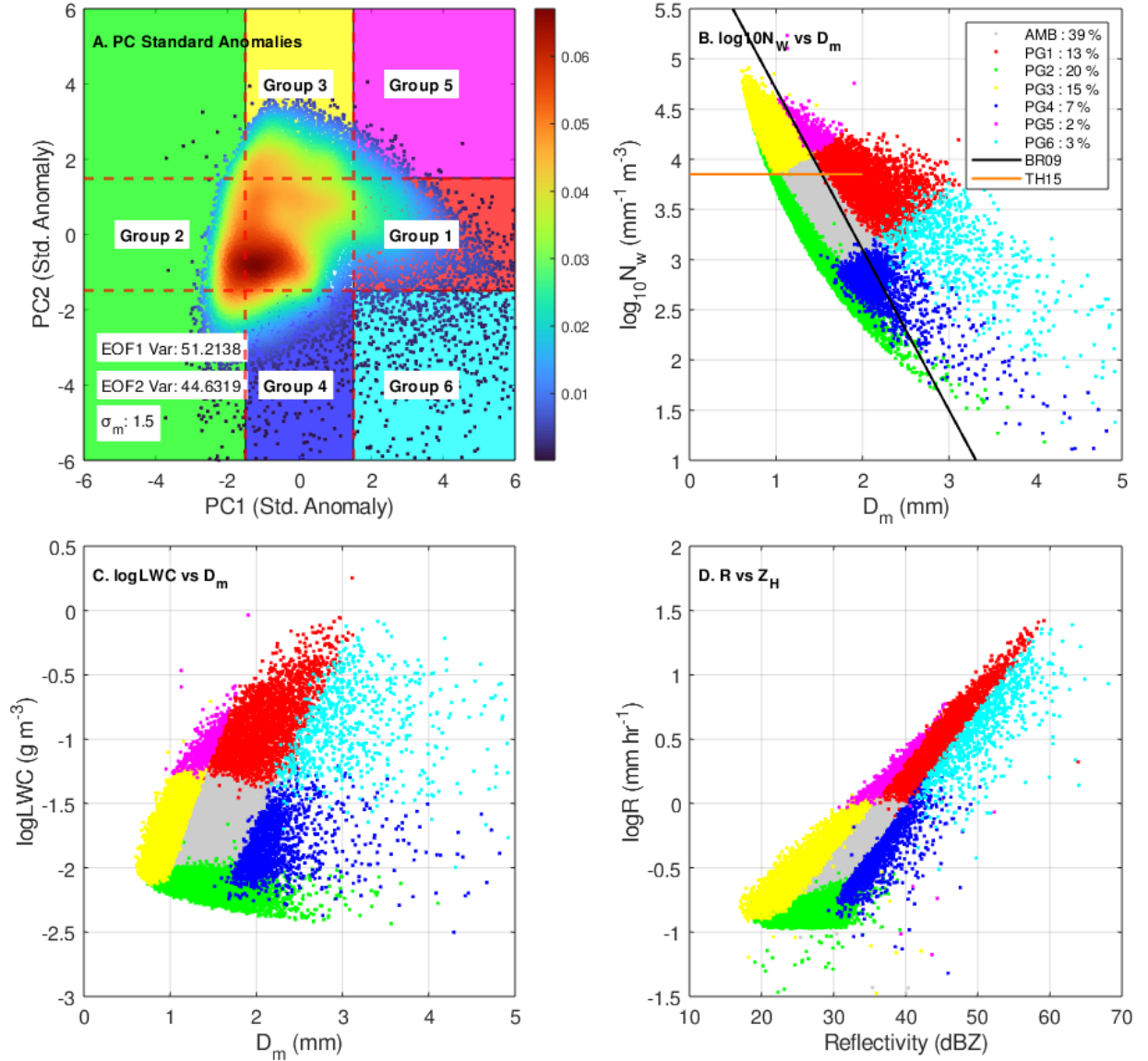


Figure 3.3 DSD clusters revealed by principal component analysis (PCA). (a) PC standard anomalies showing distinct groups: red is group 1 (PG1; convective), green is group 2 (PG2; stratiform), yellow is group 3 (PG3, convective), blue is group 4 (PG4; stratiform), group 5 is magenta (PG5; convective) and cyan is group 6 (PG6; convective), all AMB are colored gray, (b) same as (a) but PCA clusters shown in  $\log LWC$ - $D_m$  plane, (c) same as (a) and (b) but shown in  $R$ - $Z_H$  plane. The black and orange lines are the BR09 and TH15 convective-stratiform (C/S) separation lines.

the significant number of observed weak shallow convection in the area prompting a wider spread of this cluster. Clearly, though the data of the current study is within the tropics, there are significant differences when it comes to these precipitation systems.

This raises a few notable questions worthy of exploration in the future: (1) Are the datasets used by DO18 for the tropics enough to represent the region? (2) Are there substantial variations in DSD clusters within the tropics which warrants an in-depth examination? (3)

*Would including observations from more continental sites in the tropics significantly change the mode of the DSD?*

Convective DSDs (PGs 1, 5 and 6) except PG3 clearly has higher  $LWC$ ,  $R$ , and  $Z_H$ , with PG1 reflectivity values ranging from 35 dBZ to 60 dBZ. Values exceeding these are indicative of the transition of the microphysical process from the usual convective to ice-based convective which can be observed during times of intense convection. Meanwhile, PG4 has larger  $D_m$  recorded as well as reflectivities though almost having the same  $R$  as compared to PG3.

These PGs are investigated by comparing the averaged time-height profile of radar parameters to the DSD characteristics at the surface. Doing such analysis may potentially dilute significant details of the precipitation systems but nevertheless reveals the most dominant microphysical processes within the system. For ease and to ensure a smooth flow of discussion, alternate names for PGs will be used in discussing the microphysical characteristics as well as the CFADs. For convective DSD group, PG1, PG3, PG5 and PG6 are referred to as *normal convection*, *shallow convection*, *cc (collision-coalescence) convection* and *ice-based convection* respectively. In contrast, for stratiform DSD groups, PG2 is referred to as *weak stratiform* while PG4 is referred to as *moderate stratiform*.

### **3.3 Microphysical characteristics of precipitation during 2018 SWM season**

The following sections will direct the discussion towards the microphysical characteristics of precipitation by using the matched radar-disdrometer plots. Using multiple types of data allows for an in-depth study of the microphysical characteristics, especially for the representative cases chosen for *strong widespread convection (SWC)*, *strong isolated convection (SIC)*, *weak shallow convection (WC)*, and *weak stratiform (WS)*. PRHI plots are also used to reveal the vertical profile of the event. CFADs will also be presented to discuss these precipitation types in general.

#### **3.3.1 Strong Widespread Convection**

Figure 3.4 shows the microphysical processes and transitions during Event 79 which is a case for SWC. Among all the other precipitation types, SWC recorded the longest durations. Consistent with other cases for this type, this event initiated as light rain from the leading stratiform that gradually transitioned to full convection, and during the later part, transitioned back to light rain attributed to the trailing stratiform as the system passed the disdrometer location (Figure 3.4a). This widespread convection event happened on the 6<sup>th</sup> of September

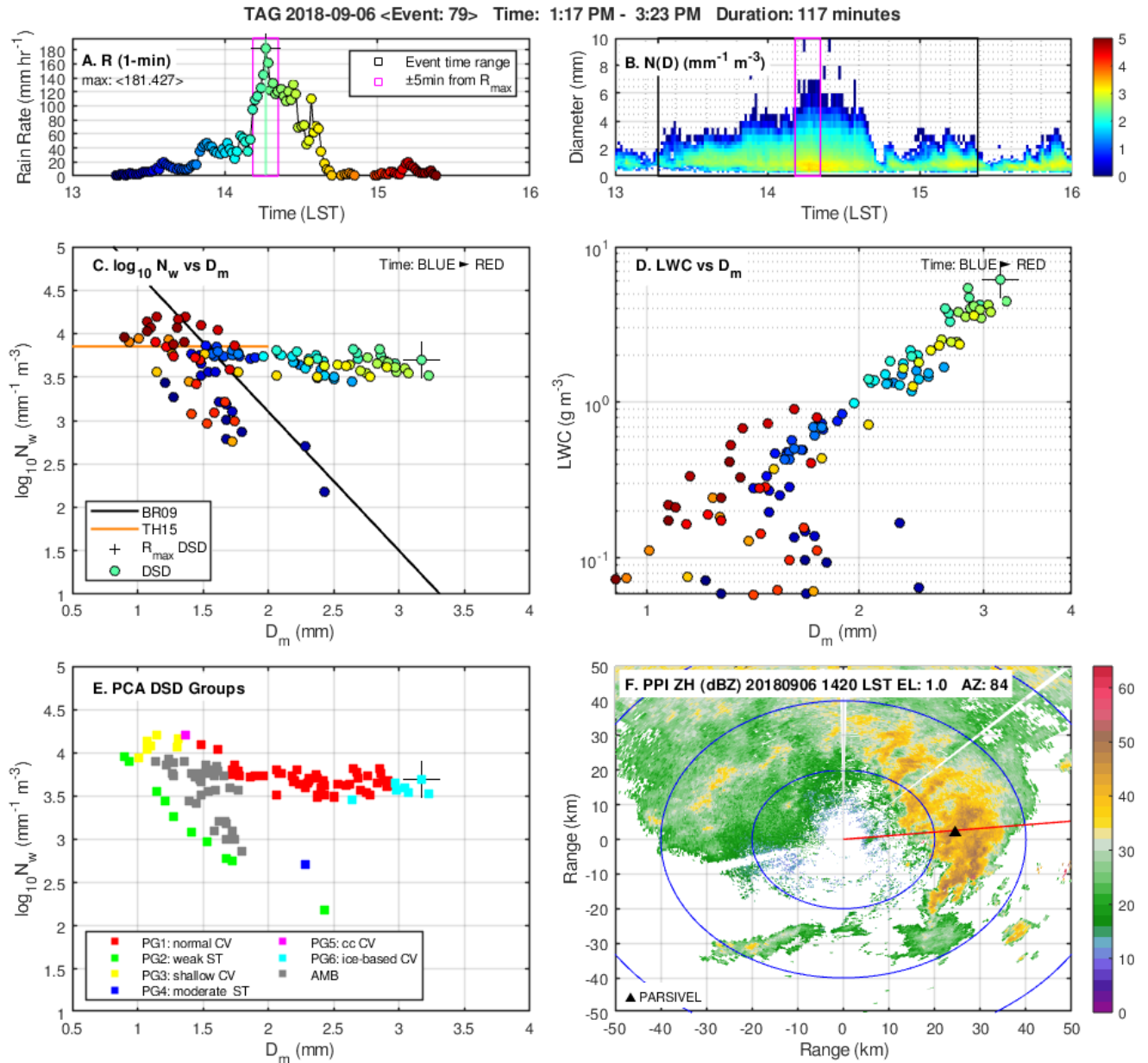


Figure 3.4 Time series of rainfall microphysics for SWC representative case (Event 79). (a)  $R$  color-coded blue to red to depict time progression; (b)  $N(D)$ ; (c)  $\log_{10}N_w$ - $D_m$  plot, same color-code as  $R$  to depict time; (d) same as (c) but for  $LWC$ ; (e) PCA DSD groups in  $\log_{10}N_w$ - $D_m$  plot; (f) PPI plot of case.

2018 at around 1317 LST and persisted for almost two hours as the system moved from southwesterly (Figure 3.4f). This event recorded intense  $R$  values reaching up to  $180 \text{ mm hr}^{-1}$  with sustained high  $R$  ( $>100 \text{ mm hr}^{-1}$ ) lasting almost half an hour. During peak  $R$ , high  $N(D)$  values can also be observed, and high concentrations of large drops were recorded. The  $\log_{10}N_w$ - $D_m$  (Figure 3.5c) plot reveals a sharp transition to the left which depicts increasing  $D_m$  values up to around  $3.25 \text{ mm}$ , but with  $\log_{10}N_w$  only slightly decreasing. Also, high  $LWC$  (Figure 3.4d) values were recorded at around  $6.1 \text{ g m}^{-3}$  during the peak  $R$ . Figure 3.4e shows multiple PGs, with convective groups (normal, shallow and ice-based) dominating the DSDs. The DSDs transitioned from normal to ice-based convection during the time of peak  $R$  and  $LWC$ .

The averaged time-height plots of dual polarization parameters (Figure 3.55a-d) also show these transitions. Around 1330 LST,  $Z_H$  values started to increase with values around 40 dBZ. During peak  $R$ , reflectivities around 50 dBZ can be seen at 3 to 4 kms and 35 dBZ can still be observed past 6 kms.  $Z_{DR}$  values show 1.5 dB and  $K_{DP}$  at the highest at  $2.5^\circ \text{ km}^{-1}$ . Correspondingly, DSDs during this time shows PG6 which explains the large drops recorded at the surface. It is also of interest that ice-based convection DSDs (PG6) appear after the highest echo top (Figure 3.5a, 1410 LST). The 35 dBZ contour can be seen near 6 kms, owing to the strong updraft during this convective event. Stratiform DSDs, particularly weak stratiform

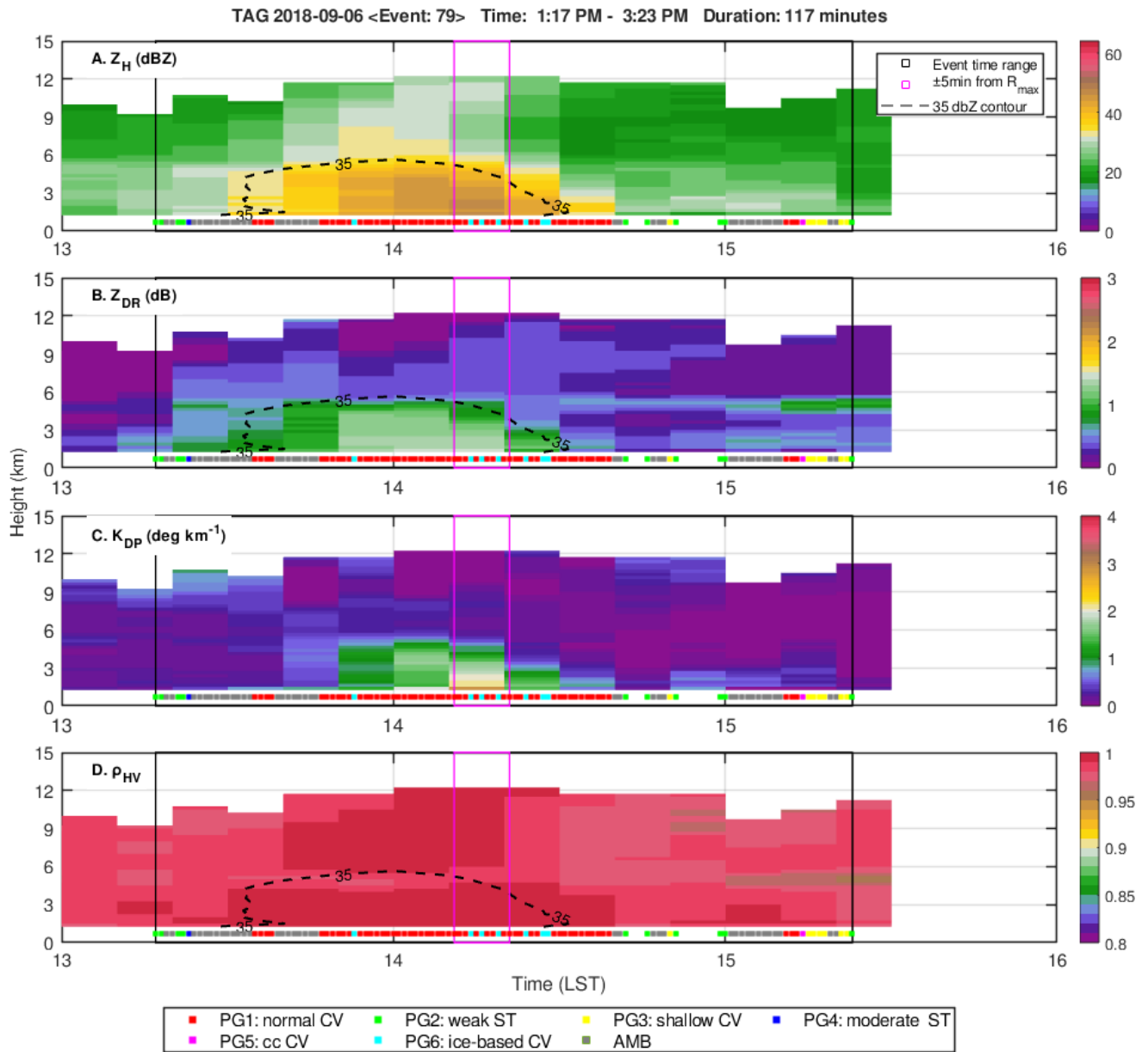


Figure 3.5 Averaged time-height plots of (a)  $Z_H$  (dBZ), (b)  $Z_{DR}$  (dB), (c)  $K_{DP}$  ( $^\circ \text{ km}^{-1}$ ), and (d)  $\rho_{HV}$  for SWC case. Colored squares below the radar plots are the time series of PGs matched with the vertical profile. Magenta box highlights  $\pm 5$  mins from  $R_{\max}$ . Black box shows the whole rainfall event time range. Broken line shows the 35 dB contour.



DSD (PG2), are also observed at the beginning and end time of this rain event. However, it is worth noting that though the initial and final part are both considered stratiform rain (associated with both the leading and trailing stratiform part of the precipitation system), there are differences observed in DSD characteristics. The rain event started with low concentrations of small to mid-sized drops, but the later part showed more concentrations of smaller raindrops.

PRHIs (Figure 3.14a-t) of this event shows higher values for the same radar parameters presented in the averaged time-height plots. At 1420 LST, during peak  $R$ , reflectivity values of around 50 dBZ can be observed at low levels (1-2 km) and extends up to 6 kms,  $Z_{DR}$  at 2 dB, and  $K_{DP}$  values of 2-2.25  $^{\circ}\text{km}^{-1}$ .

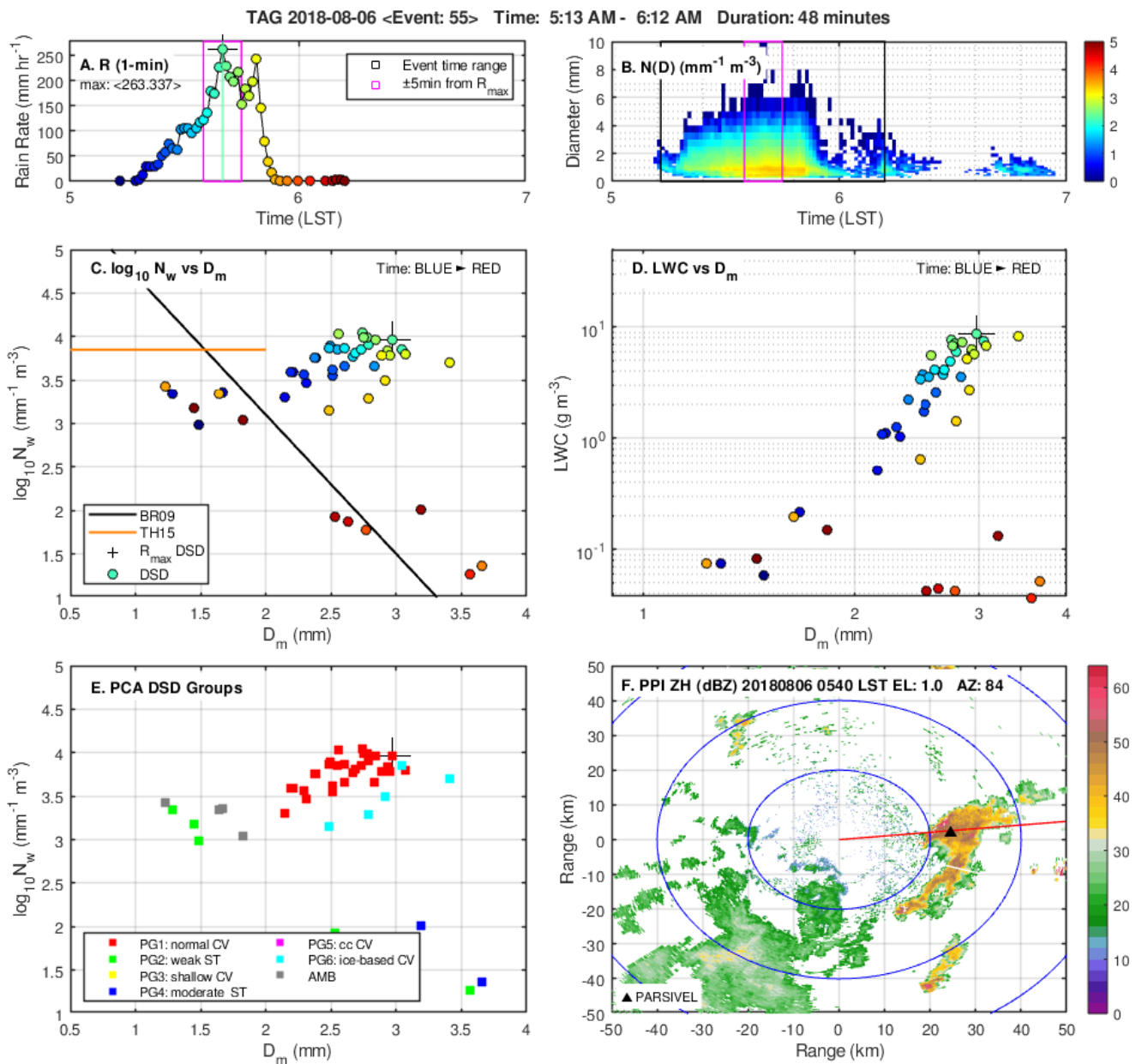


Figure 3.6 Same as Figure 3.5 but for SIC case (Event 55).



### 3.3.2 Strong Isolated Convection

Cases for SIC are usually short-lived convection systems with the most intense rainfall. In particular, Event 55, which happened during the early morning of the 6<sup>th</sup> of August 2018, lasted only about 48 minutes yet maximum  $R$  recorded reached  $263 \text{ mm hr}^{-1}$ . This convection is also spatially smaller than SWC and covers only approximately  $200 \text{ km}^2$  (Figure 3.6f) when it moved over the disdrometer.

Figure 3.6 describes the microphysical characteristics of this precipitation type. The  $\log_{10}N_w-D_m$  plot (Figure 3.6c) reveals an abrupt jump of DSDs from the relatively brief stratiform phase of the precipitation to clustering over a considerable distance above the BR09

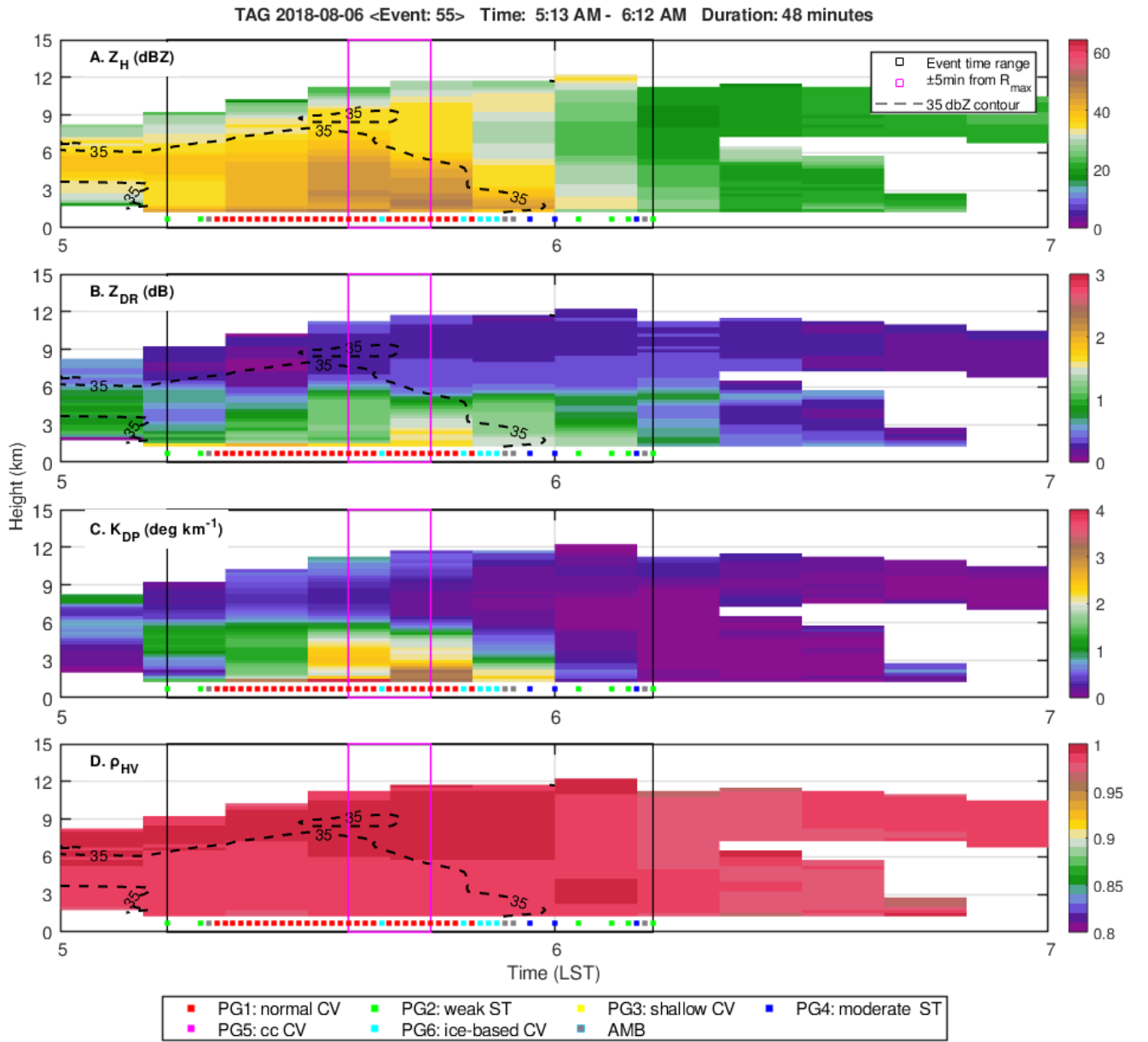


Figure 3.7 Same as Figure 3.6 but for SIC case (Event 55).

C/S line. Interestingly, there are two observable  $R$  peaks for this case: the time of  $R_{max}$  (263 mm hr<sup>-1</sup>) and eight minutes after  $R_{max}$  (250 mm hr<sup>-1</sup>). Figure 3.6c-d shows high values of  $\log_{10}N_w$  and  $LWC$ , with corresponding mid-sized to large drops. It is worth mentioning that max values of  $D_m$  (3.5-3.7 mm) were observed during the later phase of the event and not during max  $R$ . Also, for comparison, the SIC case from TH15 recorded a maximum  $LWC$  amount of 7 to 8 g m<sup>-3</sup>, however, this case recorded around 9 g m<sup>-3</sup>. This higher  $LWC$  can be attributed to the moisture-rich coastal environment primarily enhanced by the SWM which brings moisture from the ocean.

For this precipitation type, multiple DSD groups (PG1, PG2, PG4, and PG6) were observed. The DSD is mostly dominated by normal convection (PG1) and ice-based convection (PG6) appearing mostly during the second peak of the rainfall event. It is also worth mentioning that ice-based convection DSDs appear right after the deep convection owing to time delay of falling large drops. This pattern can also be seen in the SWC case. The 35 dBZ contour (Figure 3.a) can be observed even up to 9 kms further showing the intensity of this convective event. The averaged time-height plot for  $K_{DP}$  in Figure 3.7 also supports this high-water content with very intense  $Z_H$  values (50 dBZ) observed even above the freezing layer (5 km above the disdrometer). The abrupt transition from the second peak of convective rainfall to stratiform can also be seen during the later part of the event.

Showing a much detailed vertical profile, PRHIs (Figure 3.15, 0540 LST) show a defined  $Z_H$ ,  $Z_{DR}$  and  $K_{DP}$  columns during its mature stage. These prominent columns, especially  $Z_H$ , can be observed even piercing through heights above 9 kms which is typical for deep and vigorous convection. The  $K_{DP}$  values are also significantly high ( $>4$  °km<sup>-1</sup>) even above the freezing layer which can signify a mixed phase region which translates to relatively large drops observed by the disdrometer at the surface. Compared to the SWC case, reflectivity values for this rain type of around 50 dBZ can still be identified at heights of 10 kms. High  $K_{DP}$  values are concentrated below 5 kms for SWC case but for SIC case this exceeds this height. Like the SWC case, PG6 appears after the tallest echo tops. This rain type is spatially narrower, has a shorter duration than SWC, but understandably has the highest rain rates among the identified rain types.

### 3.3.3 Weak Shallow Convection

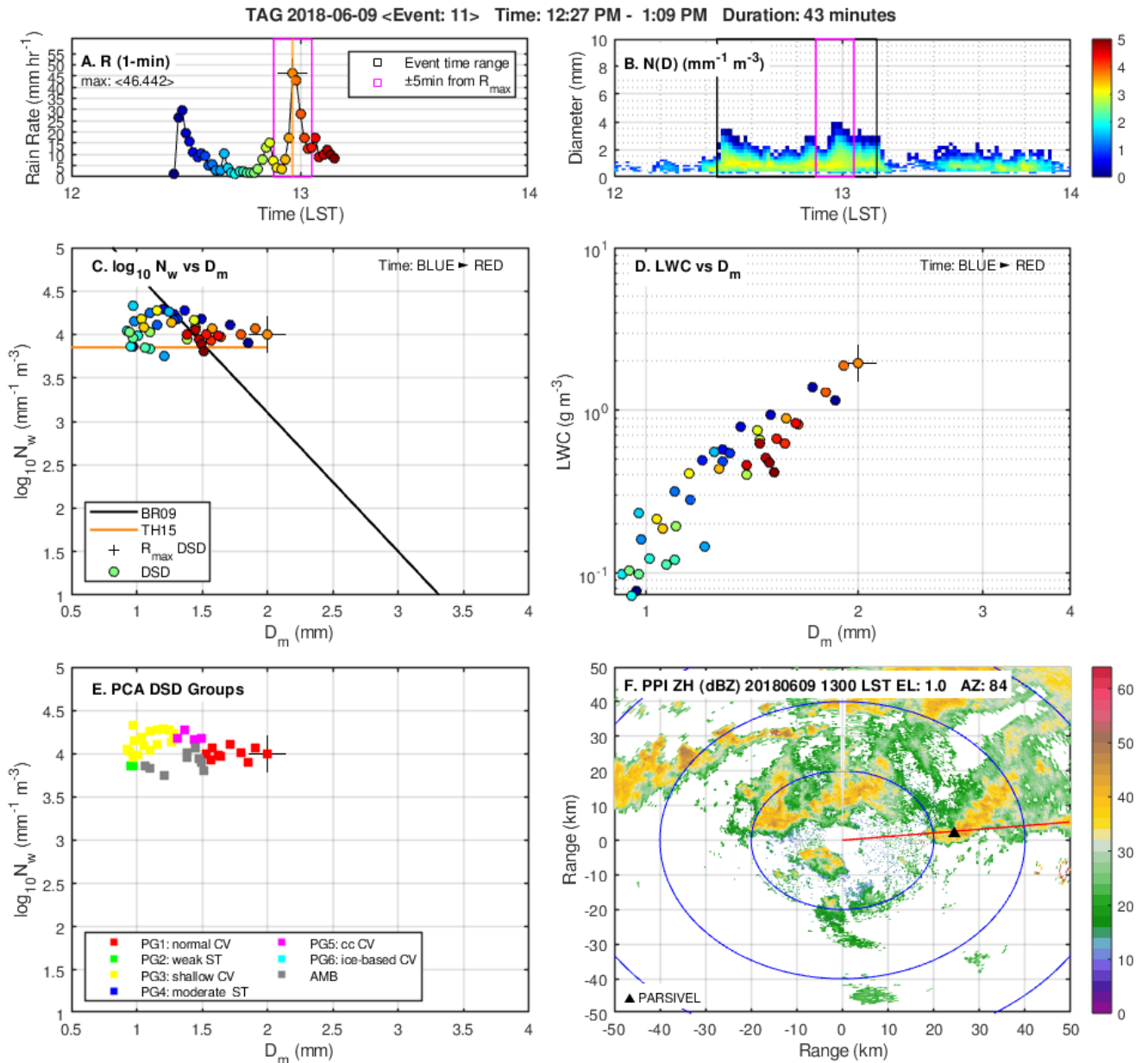


Figure 3.8 Same as Figure 3.5 but for WC case (Event 11).

Figure 3.8 describes a midday weak shallow convection (WC) event which lasted for about 43 minutes. From the observed cases of this same rain type from TH15 and DO18, these convections have relatively low  $R$  ( $<10 \text{ mm hr}^{-1}$ ) and  $Z_H$  ( $<35 \text{ dBZ}$ ). These attributes were observed for this event before transitioning to a fully convective event albeit of lower magnitude than both SWC and SIC events. Comparable to cases of WC that were observed from previous studies, the PG3 dominates the DSDs which is characterized by high concentration ( $4\text{--}4.5 \text{ mm}^{-1} \text{m}^{-3}$ ) of small drops ( $D_m < 1.5 \text{ mm}$ ). The  $N(D)$  (Figure 3.8b) shows high concentration centered around 1 mm. Before its transition (1220 -1240 LST) to a much intense convection, values of

$LWC$  are relatively low ( $< 1 \text{ g m}^{-3}$ ) with the highest value recorded at around  $2 \text{ g m}^{-3}$  during peak  $R$ .

Considering only the surface attributes of this event without carefully looking into the vertical profile leads to the usual errors in identifying this rain type as simply stratiform rain. The time height plots (Figure 3.9) reveal interesting features of this rain type. Before transitioning to full convection,  $Z_H$  remains below 35 dBZ, low  $Z_{DR}$  values ( $< 1 \text{ dB}$ ) as well as  $K_{DP}$  ( $< 0.5 \text{ g m}^{-3}$ ). The 30 dBZ contour throughout this event is confined 4 kms. The PRHIs of this event (Figure 3.16) shows that high reflectivity values are not able to penetrate the 5-km height above the disdrometer as it passes through the disdrometer, thus the ‘shallow’

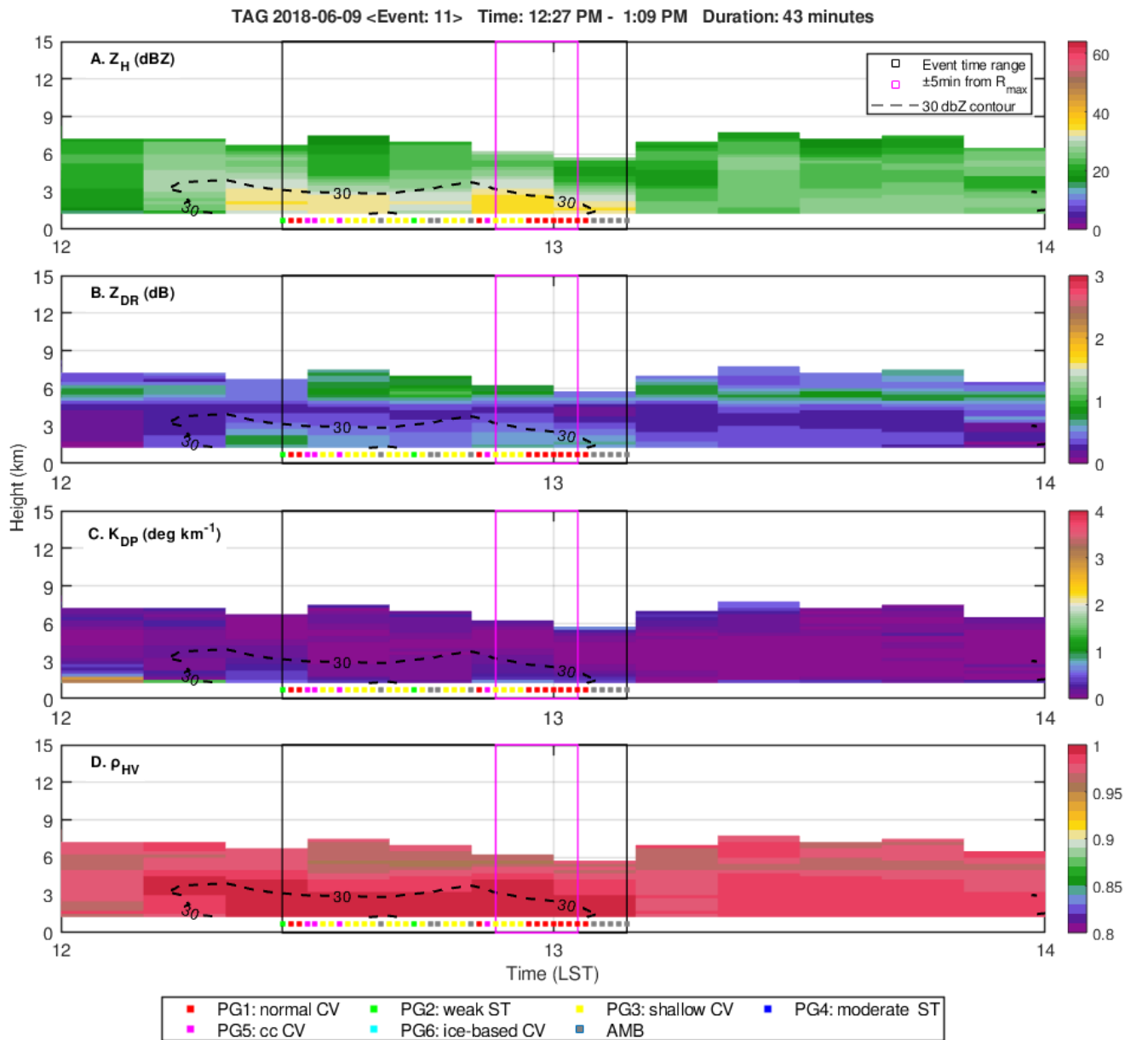


Figure 3.9 Same as Figure 3.6 but for WC case (Event 11). 30 dBZ contour line is shown instead of 35 dBZ.

classification. This also implies that updrafts are relatively weak for this rain type that hydrometeors are concentrated at lower heights. The absence of ice-based convection DSDs (PG6) and the abundance of both normal convection (PG1) and shallow convection (PG3) DSD suggests that these convections are mainly from warm rain process. This feature is distinctive for this precipitation type and are similar to those observed by TH15 using the tropical oceanic regime dataset.

### 3.3.4 Weak Stratiform

Weak stratiform (WS) cases comprised around 37% of all identified rain events. Figure 3.10 shows a WS case during the SWM season. As with most stratiform cases,  $R$  for this case

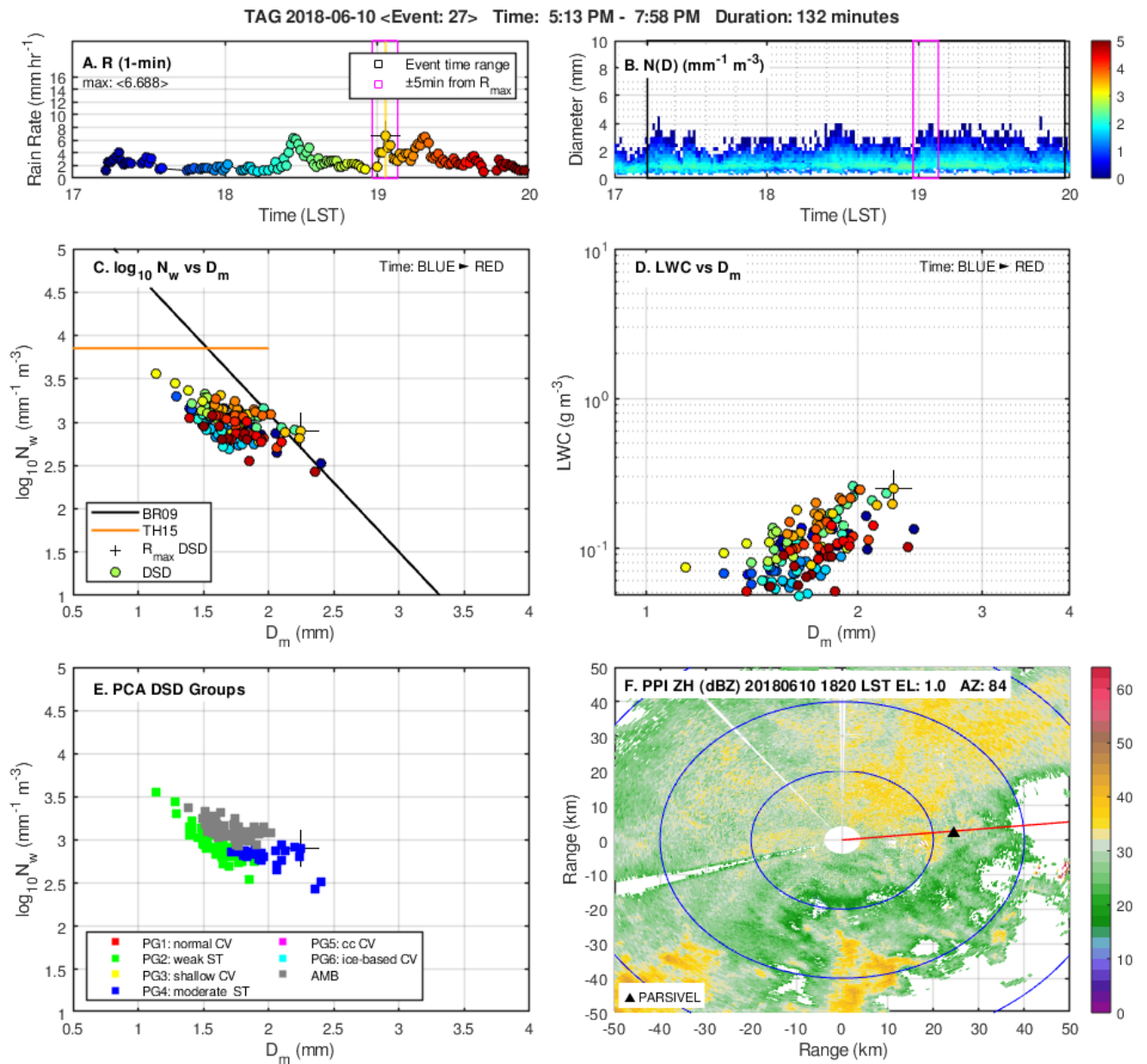


Figure 3.10 Same as Figure 3.5 but for WS case (Event 27).

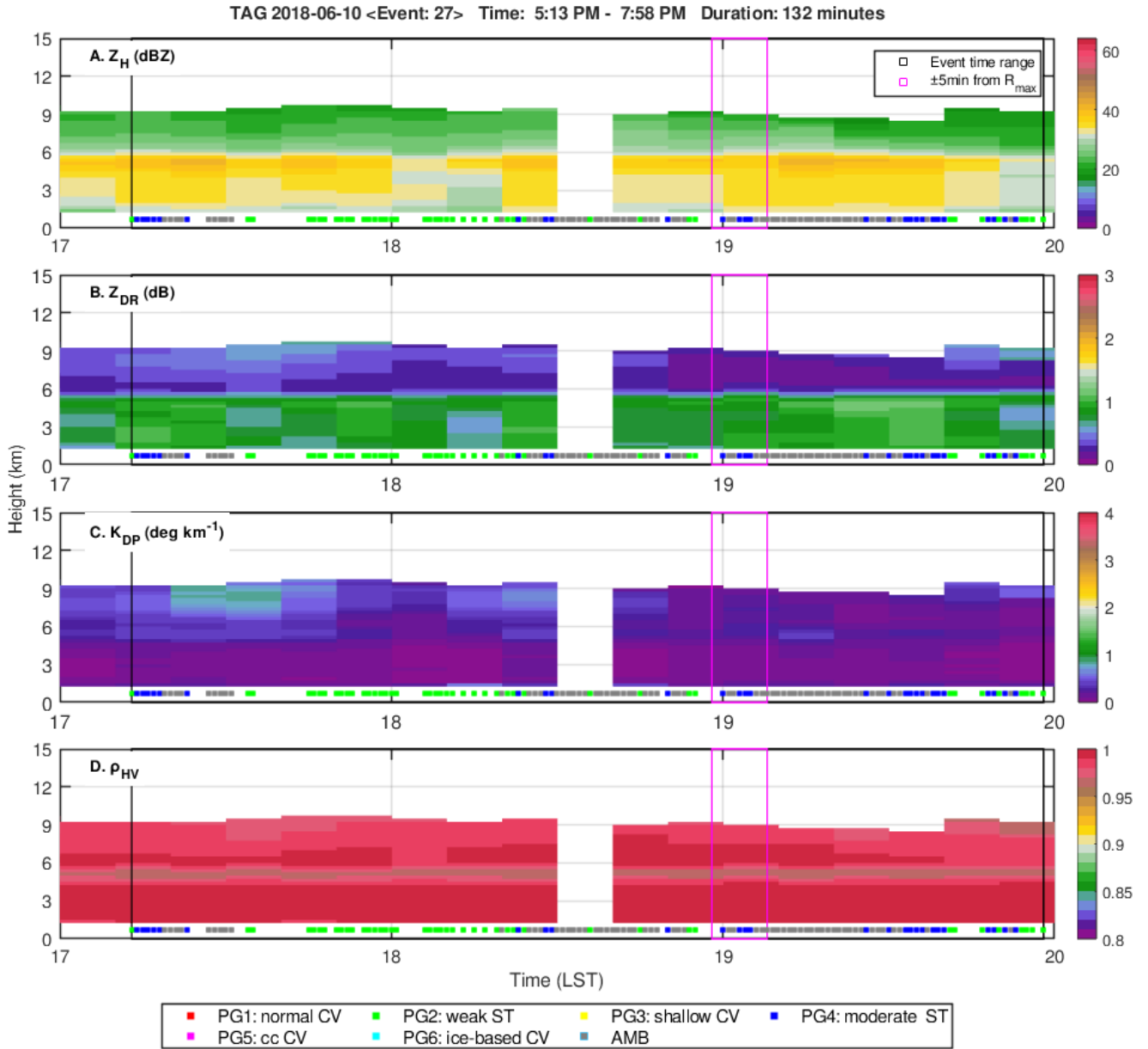


Figure 3.11 Same as Figure 3.6 but for WS case (Event 27).

is relatively low, mostly below  $10 \text{ mm hr}^{-1}$  but has a longer duration of 132 minutes. The  $\log_{10}N_w$ - $D_m$  plot reveals most of the DSDs are below the BR09 CS line with DSD briefly crossing above the line around 1900 LST. The DSDs are densely clustered around  $\log_{10}N_w$  values of 2.75 to 3.5  $\text{mm}^{-1} \text{ m}^3$  and  $D_m$  values ranging from 1 mm to 2.7 mm. Stratiform DSD groups, weak stratiform (PG2) and moderate stratiform (PG4), dominate the DSDs with the latter observed after max  $R$ . Understandably, LWC values are low ranging from 0.1 to below  $0.3 \text{ g m}^{-3}$ .

The averaged time-height profiles (Figure 3.11) of dual polarimetric variables shows a typical stratiform case. The bright band signature is evident throughout the duration of the

event especially in the  $\rho_{HV}$  plot (Figure 3.11d). Below the bright band, reflectivities are <35 dBZ, while  $Z_{DR}$  and  $K_{DP}$  values are also low at around 1 dB and <0.5 °km<sup>-1</sup> respectively. PRHIs (Figure 3.17) also reveal consistent observation for this case. Interestingly, at 1750 LST, a band of high reflectivity can be observed from the freezing layer stretching to the surface. This band is called a *fallstreak*, which is evident for rain events that transitioned from convective to stratiform (Yuter & Houze, 1997).

### 3.3.5 CFAD-PCA Group analysis

To understand and reveal the rainfall microphysical characteristics unique for each PG, CFADs of  $Z_H$ ,  $Z_{DR}$  and  $K_{DP}$  are analyzed. CFADs provide an intuitive way to visualize and analyze radar data. Figure 3.12 shows the CFADs for all identified PGs.

Much of the time-matched radar-DSD samples (33%) were classified as normal convection (PG1, Figure 3.12a, d, g). This group is the easily identifiable convective group from the DSD clusters as they are above the BR09 C/S separation line. The CFAD representing normal convection revealed a wide range of reflectivity values reaching up to more than 40 dBZ below the freezing layer with slight reduction above but still remains high. High  $Z_{DR}$  values can also be observed with the largest frequency around 0.5 to 1.25 dB. High  $K_{DP}$  values can be seen below the freezing layer which confirms that the convective rainfall events associated with this PG has very high water content and  $R$ . For this group, it can be observed that there is a slight increase in frequencies of  $Z_H$  (10 to 25 dBZ) and  $Z_{DR}$  (1.5 to 2.5 dB) at the 9-km height which suggests a possible a mixed phase region where hydrometeors grow through both warm rain and cold rain processes.

In contrast to normal convection (PG1), ice-based convection (PG6, Figure 3.12c, f, i), has the highest frequencies of reflectivity centered at 40 dBZ with sustained high values of around 40 dBZ still observable around 10 kms. At lower levels (below 4 kms), intense reflectivities reaching 50 dBZ can be observed. These observations imply that these are indeed deep and vigorous convections. The  $Z_{DR}$  CFAD for this group is skewed slightly to the right with the highest frequencies centered at 1 to 1.5 dB which is relatively higher in comparison to normal convection. The presence of positive  $Z_{DR}$  values above the freezing level suggests the presence of strong updrafts that brings water deeper into the atmosphere which leads to possible formation of both hail and graupel. In terms of  $K_{DP}$ , this group has more spread in contrast to normal convection with higher values that can be seen even 2 kms above the freezing layer.



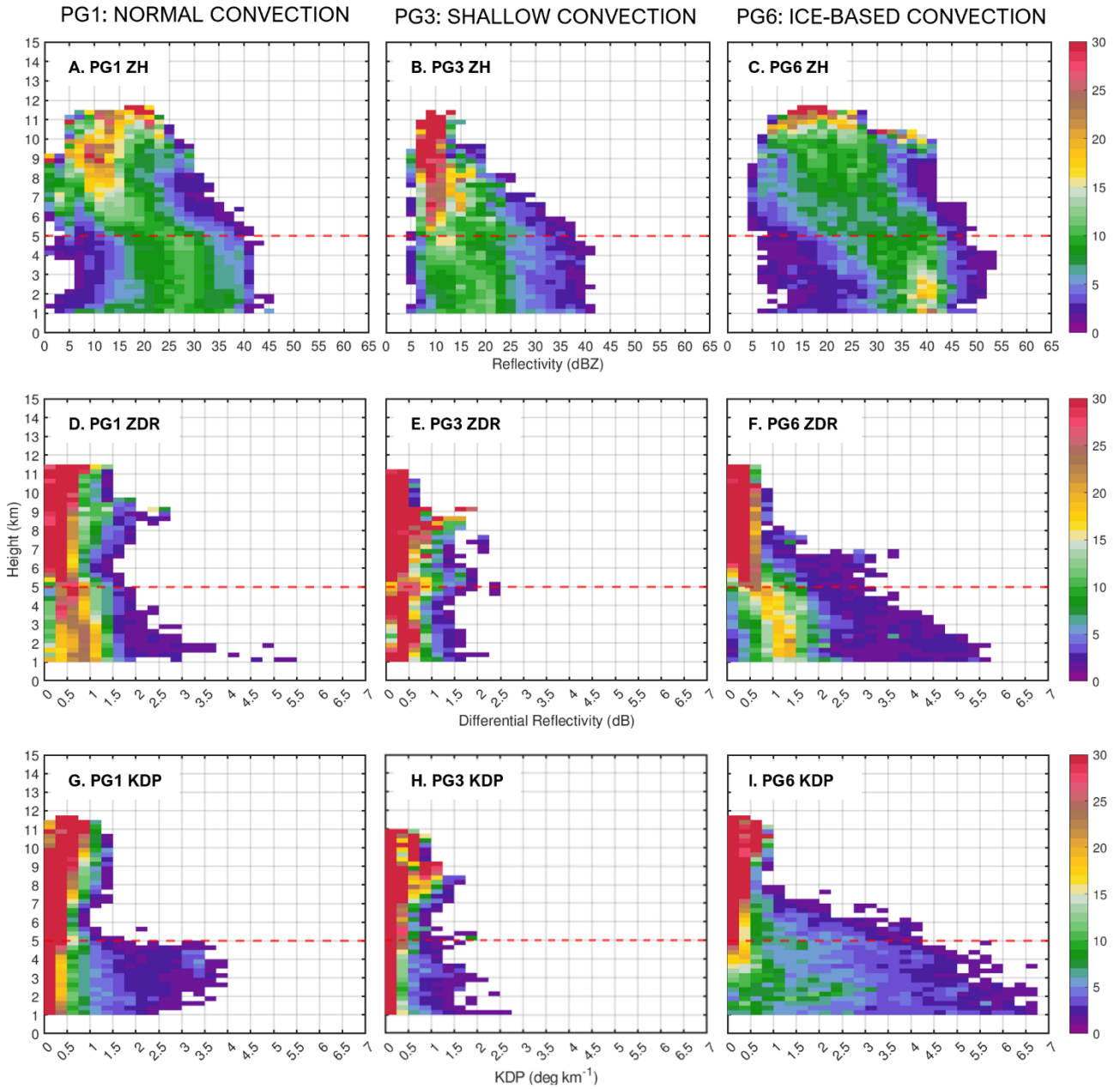


Figure 3.12 Contoured frequency by altitude diagrams (CFAD) of  $Z_H$  (dBZ),  $Z_{DR}$  (dB) and  $K_{DP}$  ( $^{\circ} \text{km}^{-1}$ ) for convective groups (a,d,g) PG1, (b,e,h) PG3, and (c,f,i) PG6. Red dashed line depicts the freezing level at 5 kms.

These high values of radar dual polarization parameters reaching the deep layers in the atmosphere support the large drops observed at the surface owing to melting of hail or graupel.

The  $Z_{DR}$  and  $K_{DP}$  CFADs of shallow convection (PG3, Figure 3.12b, e, h) show high frequencies of lower  $Z_{DR}$  and  $K_{DP}$  values. Unique to this group are high reflectivity values ( $>35$  dBZ) that do not penetrate the 5-km level. Increased  $K_{DP}$  values can be observed near the surface and drops are height increases. These supports the claim that these rain events, though having  $R$  comparable to stratiform rain, are indeed shallow convections.

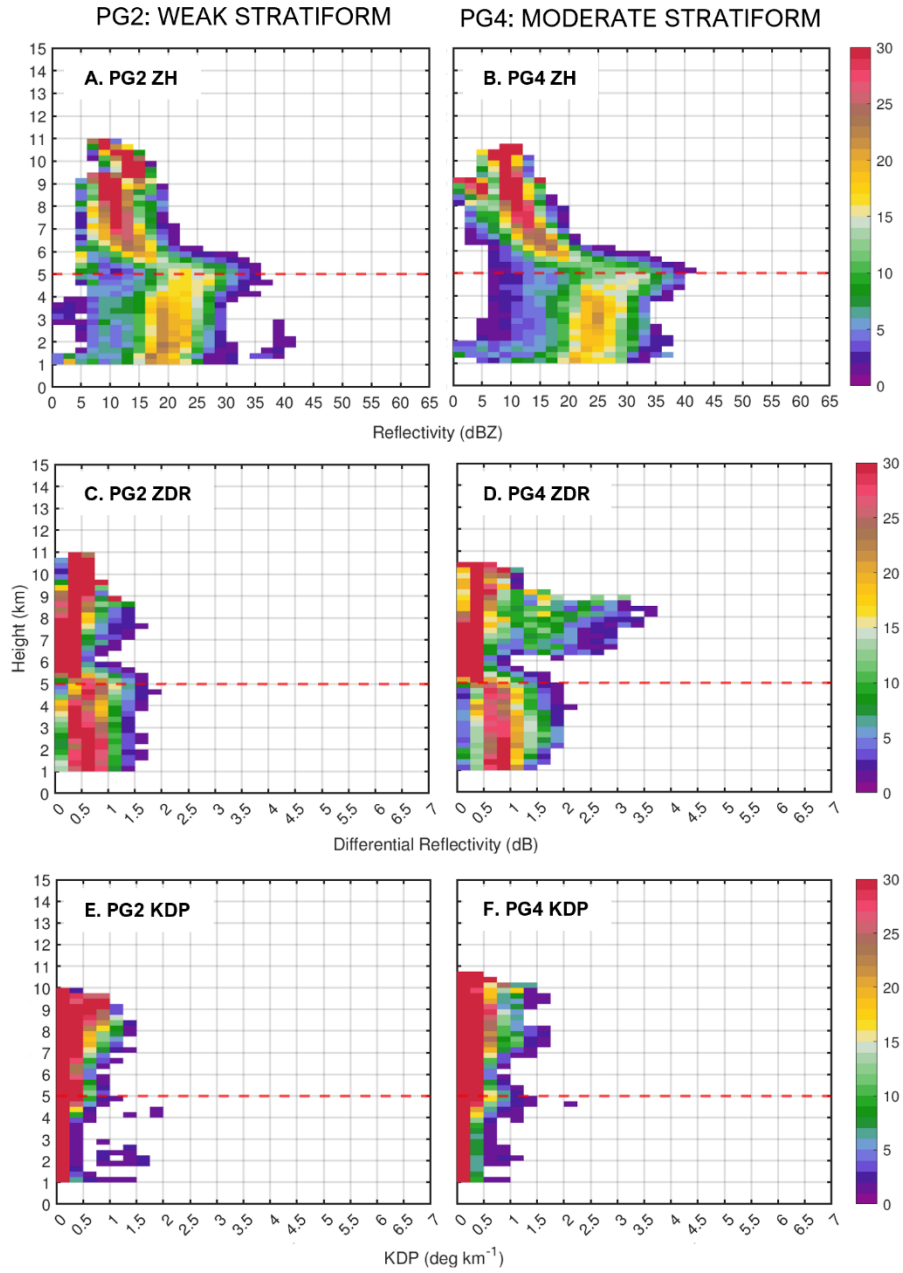


Figure 3.13 Contoured frequency by altitude diagrams (CFAD) of  $Z_H$  (dBZ),  $Z_{DR}$  (dB) and  $K_{DP}$  ( $^{\circ} \text{km}^{-1}$ ) for stratiform groups (a,d,g) PG2, and (b,d,f) PG4. Red dashed line depicts the freezing level at 5 kms.

The CFADs of the stratiform groups, weak (PG2, Figure 3.13a, c, e) and moderate (PG4, Figure 3.13b, d, f) stratiform, are nearly similar except that moderate stratiform has higher values for the same radar parameters. In both PGs, the bright band signature can be observed characterized by the increase of radar values at around 5 kms. Between the two groups, moderate stratiform has higher reflectivity values at the bright band depicted by a sharper turn to the right. This is associated with more significant melting from large, aggregated snow

thereby producing large rain drops. This is supported by large values of  $Z_{DR}$  below the melting layer (Figure 3.13d).

The insufficient number of samples obtained for cc convection (PG5) was not enough to draw reliable conclusions. Therefore, gathering more samples to better represent this group will be crucial in future research.

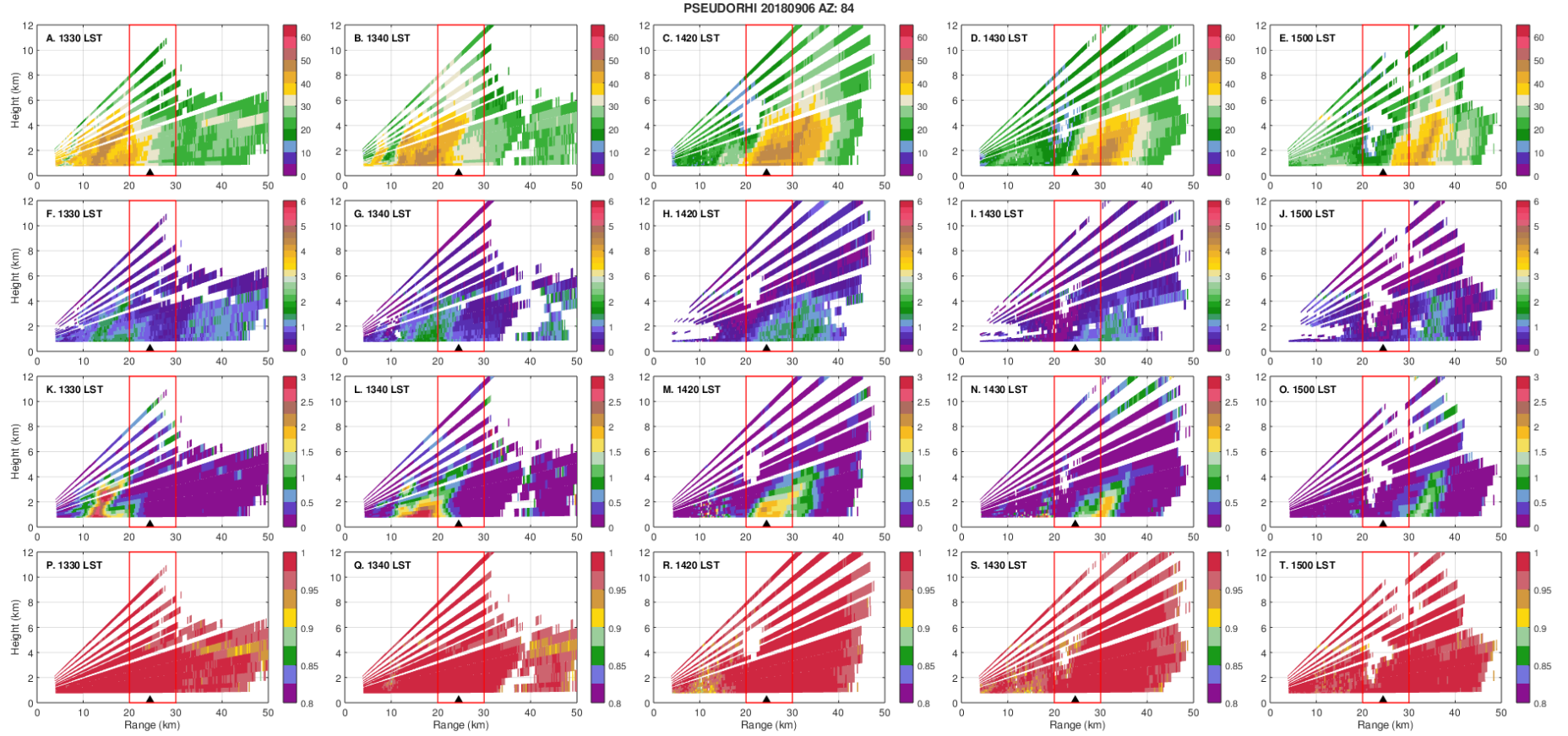


Figure 3.14 PRHIs of different radar parameters for 2018-09-06 (Event 79) which represents the SWC case. (a-e)  $Z_H$  (dBZ), (f-j)  $Z_{DR}$  (dB), (k-o)  $K_{DP}$  ( $^{\circ}\text{km}^{-1}$ ), and (p-t)  $\rho_{HV}$ . Time is indicated in each figure. The black triangle represents the relative location of the disdrometer from the TAG radar site. The red box highlights the vertical profile of the atmosphere above the disdrometer.

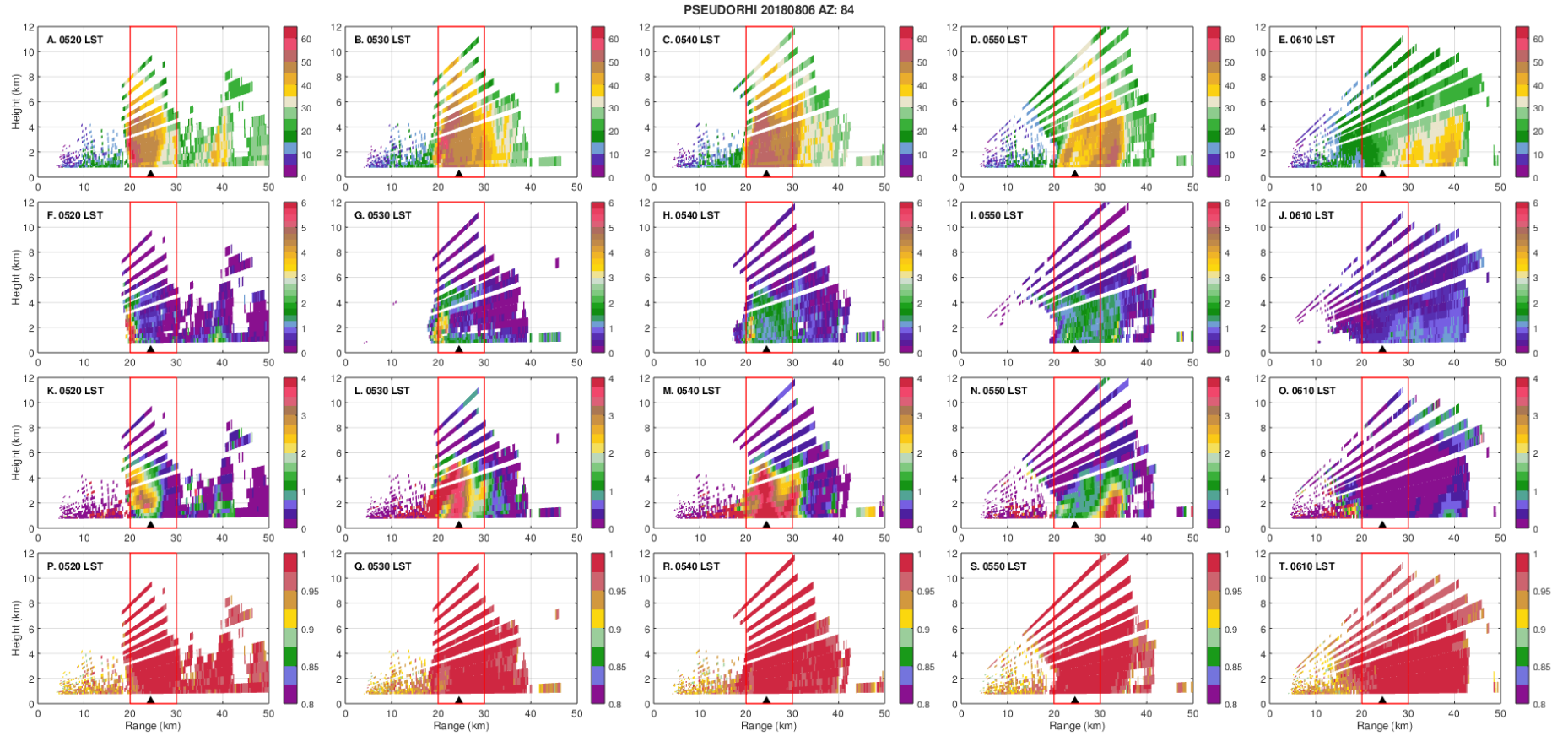


Figure 3.15 PRHIs of different radar parameters for 2018-08-06 (Event55) which represents the SIC case. (a-e)  $Z_H$  (dBZ), (f-j)  $Z_{DR}$  (dB), (k-o)  $K_{DP}$  ( $^{\circ}\text{km}^{-1}$ ), and (p-t)  $\rho_{HV}$ . Time is indicated in each figure. The black triangle represents the relative location of the disdrometer from the TAG radar site. The red box highlights the vertical profile of the atmosphere above the disdrometer.

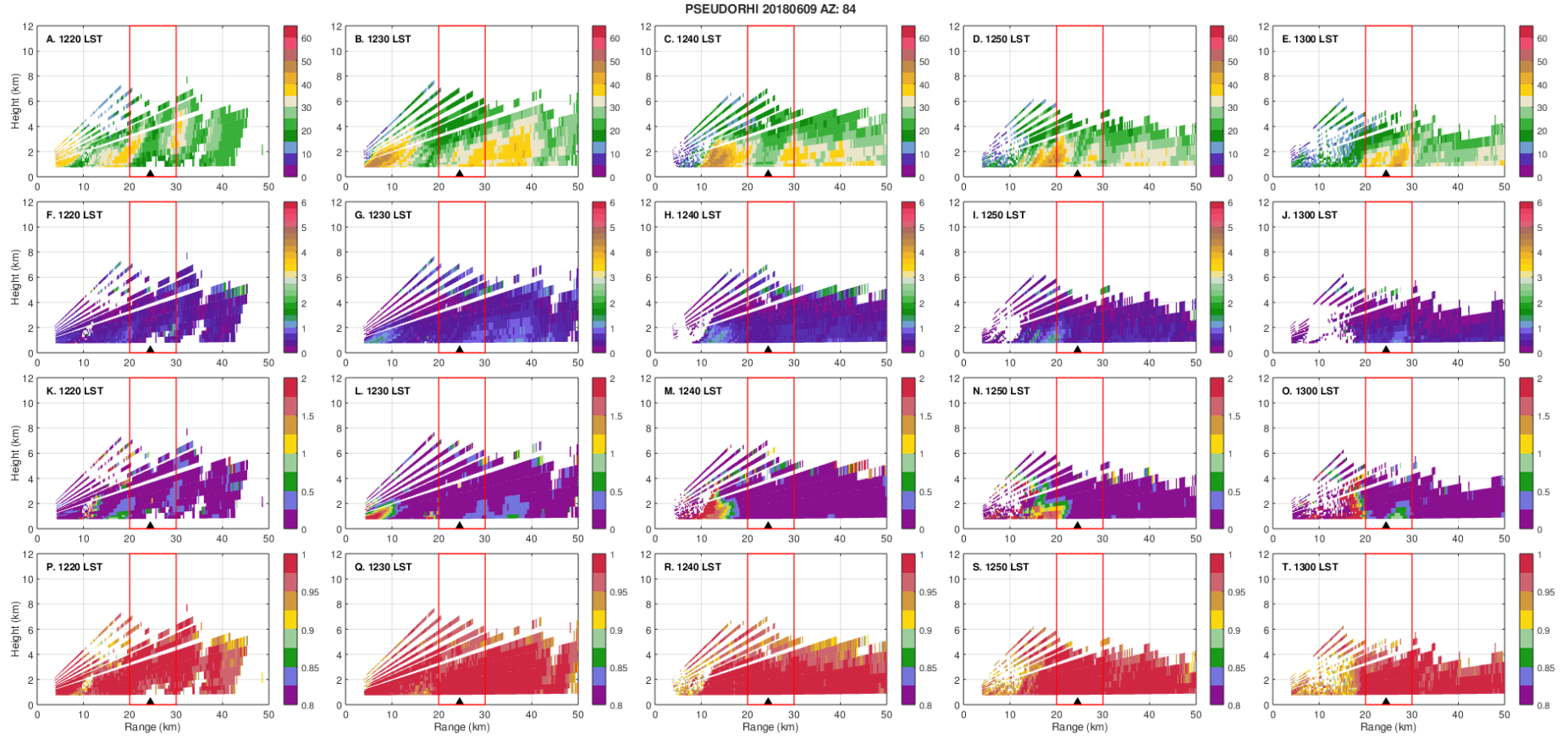


Figure 3.16 PRHs of different radar parameters for 2018-06-09 (Event 11) which represents the WC case. (a-e) Z<sub>H</sub> (dBZ), (f-j) Z<sub>DR</sub> (dB), (k-o) K<sub>DP</sub> (°km<sup>-1</sup>), and (p-t) ρ<sub>HV</sub>. Time is indicated in each figure. The black triangle represents the relative location of the disdrometer from the TAG radar site. The red box highlights the vertical profile of the atmosphere above the disdrometer.



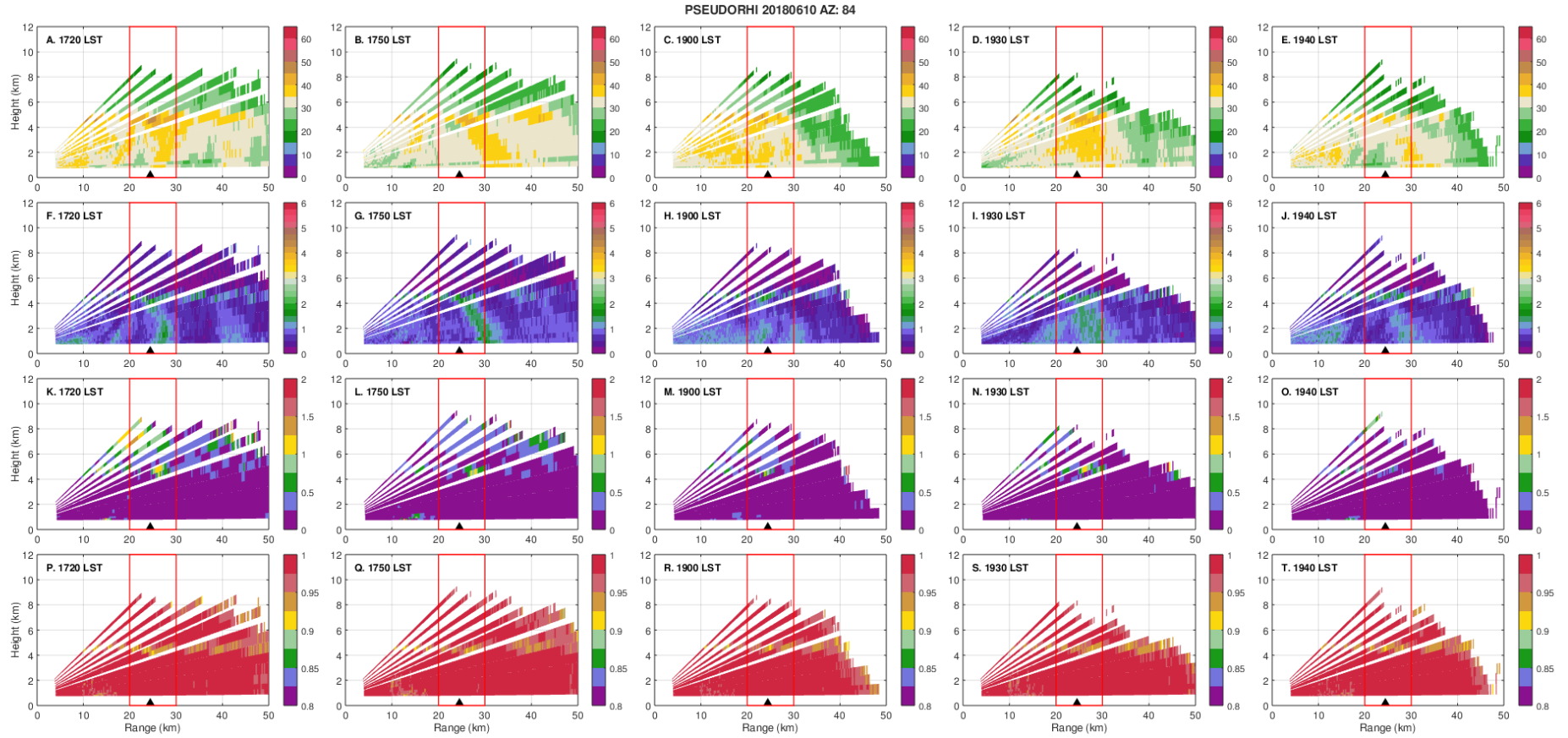


Figure 3.17 PRHIs of different radar parameters for 2018-06-10 (Event 27) which represents the WS case. (a-e)  $Z_H$  (dBZ), (f-j)  $Z_{DR}$  (dB), (k-o)  $K_{DP}$  ( $^{\circ}\text{km}^{-1}$ ), and (p-t)  $\rho_{HV}$ . Time is indicated in each figure. The black triangle represents the relative location of the disdrometer from the TAG radar site. The red box highlights the vertical profile of the atmosphere above the disdrometer.



## Chapter 4 CONCLUSION

This study examined long-term DSD data to describe the seasonal variability of DSDs during the SWM, NEM and TRA seasons in South Luzon, Philippines. The microphysical characteristics and processes of rainfall events during the 2018 SWM season are revealed and analyzed using disdrometer data and the Tagaytay C-band dual polarization weather radar data. The objective analysis presented here involves calculating IRPs ( $N_w$ ,  $D_m$ ,  $\sigma_m$ ,  $R$ ,  $LWC$  and  $N_t$ ) and applying PCA on the same DSD variables to determine clusters (PG) of DSDs with the same characteristics and variabilities. The analysis of the microphysics of different precipitation types are conducted by identifying and classifying rain events, and finally, relating the PGs to vertical profiles of  $Z_H$ ,  $Z_{DR}$  and  $K_{DP}$  through CFADs.

### 4.1 Summary

#### 4.1.1 Seasonal variability of DSD in South Luzon, Philippines

Comparing the DSDs between the different seasons reveals consistent results with previous findings (Aragon et al., 2024; Ibañez et al., 2023; Ibañez et al., 2022; Macuroy et al., 2021). The  $\log_{10}N_w-D_m$  plots generally shows that most of the DSDs are from stratiform events. The DSDs during NEM are composed of small drops with high concentration, while both SWM and TRA have lesser concentration of drops but bigger drop diameters. These results are more apparent and consistent as shown in the  $\log_{10}N(D)-D_m$  plot which were further categorized per rain rate class. Across different rain rate classes, NEM has the largest concentration of small drops but for bigger drops ( $\geq 2.5$  mm) in Class 3, 4 and 5, SWM and TRA overtakes NEM. However, compared to both NEM and SWM, it is worth mentioning that TRA has lesser DSD samples from the data available. In addition, the mean of SWM convective rain is near the BR09 continental clusters. This means that convection in South Luzon, Philippines share some similar characteristics as those from more continental environments.

#### 4.1.2 Modes of DSD

Each identified and calculated IRP describes one important characteristic or variability related to the DSD. By applying PCA to the DSD data, all parameters were considered and analyzed simultaneously, resulting to clusters of DSDs (PGs) exhibiting similar characteristics and variability. Similar with the work of DO18, six clusters were identified from the current dataset. It is important to highlight that as compared to DO18's PCA result, the data yielded

lesser scatter towards higher PC2 standard anomaly. This is especially evident in PG3 and PG5. One of the main causes of this significant difference is the nature of data used. It can be recalled that for the low latitude data, DO18 used the combined dataset from Manus Island and Gan Island, which were both used to represent the characteristics of rain in a tropical oceanic regime, where shallow convections are said to be ubiquitous.

#### 4.1.3 DSD-radar joint analysis

To show the microphysics and how these are reflected in radar parameters, rain events were identified and classified into four: *SWC*, *SIC*, *WC* and, *WS*.

Out of the four rain types, both the SWC and WS have the longest durations ranging from about an hour to more than two hours. The  $\log_{10}N_w-D_m$  plot shows the microphysical transitions during an SWC event from its stratiform phase to a full convection phase and its return to stratiform. High concentrations of big drops can be observed from both SWC and SIC cases also with comparable high  $R$  and  $LWC$  values. Clustered above the separation line, normal convection (PG1) and ice-based convection (PG6) DSD groups can be observed from SIC, while for WS, weak stratiform (PG2) and moderate stratiform (PG4) DSD groups are distinctly clustered below. For WS, the DSDs are dominated by shallow convection (PG3) DSDs, characterized by very high concentration of small drops. Meanwhile, since systems in SWC has longer durations, multiple PGs can be observed showing the transitions within the system.

Radar vertical profiles show much more details regarding these rain types. The transitions can also be seen in radar for the SWC case. During the SWC peak  $R$ , high values of radar parameters can be observed. For SIC, the presence of intense  $Z_H$ ,  $Z_{DR}$  and  $K_{DP}$  columns are common, which is typical for deep convections. High values of radar parameters for this rain type even reaches almost 12 kms above. Unique to WC, reflectivities around 35 dBZ are observed but are not able to penetrate higher than 5 kms thus confirming the shallowness of these systems. Furthermore, these can be mistaken for stratiform since the microphysical characteristics resemble those from the stratiform but with slightly higher  $R$ . Finally, for WS, which has consistent low  $R$ , the bright band signature can be seen in all cases.

Regardless of rain types, this study analyzed the relation between the different PGs and the corresponding radar parameters. This is meticulously done by matching the DSD and radar data and presented as CFADs for  $Z_H$ ,  $Z_{DR}$  and  $K_{DP}$ . The  $Z_H$  CFAD for normal convection (PG1) reveal a wide range of values even at higher altitudes. High values of  $Z_{DR}$  and  $K_{DP}$  can also be observed even above the freezing layer. In contrast, higher frequencies for  $Z_H$  are centered

around 40 dBZ for ice-based convection (PG6). This group also records much higher values of  $Z_{DR}$  and  $K_{DP}$  values compared to normal convection implying the intense and vigorous nature of these systems. On the other hand, for shallow convection (PG3), the  $Z_{DR}$  and  $K_{DP}$  CFAD resemble those of the stratiform groups but with a different reflectivity signature. The PG3 CFAD shows that convective values ( $\geq 35$  dBZ) are confined below the freezing layer. Additionally, compared to the two previous convective groups, these shallow convections are less intense which suggests that updrafts in these events are relatively weaker thereby only confining it below the freezing layer. For the stratiform groups, weak stratiform (PG2) and moderate stratiform (PG4), the CFADs generally reveal higher frequencies for low values, except for the difference in reflectivities with PG4 having slightly higher values than PG2.

#### 4.1.4 Conclusion

The SWM season in the Philippines contributes significantly to the country's annual accumulated rainfall as it also coincides with the TC season. Excluding rainfall events affected or associated to TCs, a huge fraction of observed rainfall events during the SWM season falls under the stratiform classification which is characterized by abundance of small drops. On the other hand, convective rains during SWM produces large drops compared to NEM. By classifying rainfall events into *SWC*, *SIC*, *WC*, and *WC*, this study showed the unique attributes of these precipitation types. The PCA revealed DSD clusters which were time-matched and jointly analyzed with radar vertical profiles. These findings are consistent with the results from DO18, noting the presence of weak shallow convections (PG3) as well as the high echo tops observed concurrent with the presence of ice-based convection (PG6) DSDs.

In the context of the Philippines, this study is one of the first attempts to relate both disdrometer and radar data to understand the microphysical characteristics and processes of precipitation systems. This research provided a more detailed perspective on the SWM rainfall events that were relatively unexplored before. Lastly, the results from this study further highlight the potential of the Tagaytay C-band dual polarization weather radar to observe mesoscale rain events that can greatly impact high-risk and densely populated areas in South Luzon and even in Metro Manila.

#### 4.2 Future work

This study opened the opportunity to study mesoscale events in a tropical environment such as the Philippines using both radar and disdrometer data. In the future, a more comprehensive analysis of these same precipitation types and PGs can be applied to a larger

dataset. This can lead to a more complete analysis of both the microphysical characteristics and processes not only for SWM, but also for both NEM and TRA seasons which has different microphysical characteristics and contributes significantly to the county's annual accumulated rainfall. With a larger dataset, there should be enough samples to represent and analyze convections with dominant collision-coalescence processes (PG5).

With the readily available satellite products such as GPM-DPR data, a broader picture of the DSD characteristics can be drawn. These satellite products have a larger spatial coverage than surface radars which is beneficial in studying the microphysics behind TCs and other synoptic events.

## References

- Abon, C. C., Kneis, D., Crisologo, I., Bronstert, A., David, C. P., & Heistermann, M. (2016). Evaluating the potential of radar-based rainfall estimates for streamflow and flood simulations in the Philippines. *Geomatics, Natural Hazards and Risk*, 1390-1405. <https://doi.org/http://dx.doi.org/10.1080/19475705.2015.1058862>
- Aragon, L. G., Ibanez, M. P., Ordinario, R. C., Simpás, J. B., Cambaliza, M. O., Dado, J. M., Maquiling, J. T., & Reid, E. A. (2024). Seasonal characteristics of raindrop size distribution and implication for radar rainfall retrievals in Metro Manila, Philippines. *Atmospheric Research*. <https://doi.org/https://doi.org/10.1016/j.atmosres.2024.107669>
- Asuncion, J. F., & Jose, A. M. (1980). A study of the characteristics of the northeast and southwest monsoons in the Philippines. *NRCP Assisted Project*.
- Bagtasa, G. (2017). Contribution of Tropical Cyclones to Rainfall in the Philippines. *Journal of Climate*, 3621-3633. <https://doi.org/https://doi.org/10.1175/JCLI-D-16-0150.1>
- Bagtasa, G. (2019). Enhancement of Summer Monsoon Rainfall by Tropical Cyclones in Northwestern Philippines. *Journal of the Meteorological Society of Japan*, 967-976. <https://doi.org/10.2151/jmsj.2019-052>
- Bagtasa, G. (2020). Influence of Madden–Julian Oscillation on the Intraseasonal Variability of Summer and Winter Monsoon Rainfall in the Philippines. *Journal of Climate*, 9581–9594. <https://doi.org/https://doi.org/10.1175/JCLI-D-20-0305.1>
- Bagtasa, G. (2023). Characterization of the 2012 and 2013 Metro Manila “Enhanced Habagat” Heavy Rainfall Events. *Philippine Journal of Science*, 123-135.
- Bañares, E. N., Narisma, G. T., Simpás, J. B., Cruz, F. T., Lorenzo, G. R., Cambaliza, M. O., & Coronel, R. C. (2021). Seasonal and diurnal variations of observed convective rain events in Metro Manila, Philippines. *Atmospheric Research*. <https://doi.org/https://doi.org/10.1016/j.atmosres.2021.105646>
- Bang, W., Lee, G., Ryzhkov, A., Schuur, T., & Lim, K.-S. S. (2020). Comparison of Microphysical Characteristics between the Southern Korean Peninsula and Oklahoma Using Two-Dimensional Video Disdrometer Data. *Journal of Hydrometeorology*, 2675-2690. <https://doi.org/10.1175/JHM-D-20-0087.1>
- Beard, K. V. (1976). Terminal Velocity and Shape of Cloud and Precipitation Drops Aloft. *Journal of the Atmospheric Sciences*, 851-864. [https://doi.org/https://doi.org/10.1175/1520-0469\(1976\)033<0851:TVASOC>2.0.CO;2](https://doi.org/https://doi.org/10.1175/1520-0469(1976)033<0851:TVASOC>2.0.CO;2)
- Brandes, E. A., Zhang, G., & Vivekanandan, J. (2002). Experiments in Rainfall Estimation with a Polarimetric Radar in a Subtropical Environment. *Journal of Applied Meteorology*, 674-685. [https://doi.org/https://doi.org/10.1175/1520-0450\(2002\)041<0674:EIREWA>2.0.CO;2](https://doi.org/https://doi.org/10.1175/1520-0450(2002)041<0674:EIREWA>2.0.CO;2)
- Bringi, V. N., Chandrasekar, V., Balakrishnan, N., & Zrníc, D. S. (1990). An Examination of Propagation Effects in Rainfall on Radar Measurements at Microwave Frequencies.

- Journal of Atmospheric and Oceanic Technology*, 829-840.  
[https://doi.org/https://doi.org/10.1175/1520-0426\(1990\)007<0829:AEOPFI>2.0.CO;2](https://doi.org/https://doi.org/10.1175/1520-0426(1990)007<0829:AEOPFI>2.0.CO;2)
- Bringi, V. N., Chandrasekar, V., Hubbert, J., Gorgucci, E., Randeu, W. L., & Schoenhuber, M. (2003). Raindrop Size Distribution in Different Climatic Regimes from Disdrometer and Dual-Polarized Radar Analysis. *Journal of Atmospheric Sciences*, 354-365.  
[https://doi.org/https://doi.org/10.1175/1520-0469\(2003\)060<0354:RSDIDC>2.0.CO;2](https://doi.org/https://doi.org/10.1175/1520-0469(2003)060<0354:RSDIDC>2.0.CO;2)
- Bringi, V. N., Williams, C. R., Thurai, M., & May, P. T. (2009). Using Dual-Polarized Radar and Dual-Frequency Profiler for DSD Characterization: A Case Study from Darwin, Australia. *Journal of Atmospheric and Oceanic Technology*.  
<https://doi.org/10.1175/2009JTECHA1258.1>
- Carey, L. D., Rutledge, S. A., & Ahijevych, D. A. (2000). Correcting Propagation Effects in C-Band Polarimetric Radar Observations of Tropical Convection Using Differential Propagation Phase. *Journal of Applied Meteorology*, 1405-1433.  
[https://doi.org/https://doi.org/10.1175/1520-0450\(2000\)039<1405:CPEICB>2.0.CO;2](https://doi.org/https://doi.org/10.1175/1520-0450(2000)039<1405:CPEICB>2.0.CO;2)
- Cayanan, E. O., Chen, T.-C., Argete, J. C., Yen, M.-C., & Nilo, P. D. (2011). The Effect of Tropical Cyclones on Southwest Monsoon Rainfall in the Philippines. *Journal of the Meteorological Society of Japan*, 123--139. <https://doi.org/10.2151/jmsj.2011-A08>
- Chang, W.-Y., Lee, G., Jou, B. J.-D., Lee, W.-C., Lin, P.-L., & Yu, C.-K. (2020). Uncertainty in Measured Raindrop Size Distributions from Four Types of Collocated Instruments. *Remote Sensing*. <https://doi.org/10.3390/rs12071167>
- Chang, W.-Y., Vivekanandan, J., & Wang, T.-C. C. (2014). Estimation of X-Band Polarimetric Radar Attenuation and Measurement Uncertainty Using a Variational Method. *Journal of Applied Meteorology and Climatology*, 1099-1119. <https://doi.org/10.1175/JAMC-D-13-0191.1>
- Chang, W.-Y., Vivekanandan, J., Ikeda, K., & Lin, P.-L. (2016). Quantitative Precipitation Estimation of the Epic 2013 Colorado Flood Event: Polarization Radar-Based Variational Scheme. *Journal of Applied Meteorology and Climatology*, 1477-1495.  
<https://doi.org/10.1175/JAMC-D-15-0222.1>
- Chen, B., Yang, J., & Pu, J. (2013). Statistical Characteristics of Raindrop Size Distribution in the Meiyu Season Observed in Eastern China. *Journal of the Meteorological Society of Japan*, 215-227. <https://doi.org/10.2151/jmsj.2013-208>
- Crisologo, I., Vulpiani, G., Abon, C., David, C., Bronstert, A., & Heistermann, M. (2014). Polarimetric Rainfall Retrieval from a C-Band Weather Radar in a Tropical Environment (The Philippines). *Asia-Pac. J. Atmos. Sci.*  
<https://doi.org/10.1007/s13143-014-0049-y>
- Dolan, B., Fuchs, B., Rutledge, S. A., Barnes, E. A., & Thompson, E. J. (2018). Primary Modes of Global Drop Size Distributions. *Journal of Atmospheric Sciences*, 1453-1476.  
<https://doi.org/10.1175/JAS-D-17-0242.1>
- DOST-PAGASA. (n.d.). <https://www.pagasa.dost.gov.ph/climate/climate-data>

- Flores, J., & Balagot, V. (1969). Climate of the Philippines. In H. Arakawa, *Climates of Northern and Eastern Asia, World Survey of Climatology* (pp. 159-213). Amsterdam, New York: Elsevier.
- Heistermann, M., Crisologo, I., Abon, C. C., Racoma, B. A., Jacobi, S., Servando, N. T., David, C. P., & Bronstert, A. (2013). Brief communication "Using the new Philippine radar network to reconstruct the Habagat of August 2012 monsoon event around Metropolitan Manila". *Natural Hazards and Earth System Sciences*, 653-657. <https://doi.org/10.5194/nhess-13-653-2013>
- Huang, X., Bai, L., Yu, Z., Chan, J. C., Yu, H., Tang, J., Guo, R., & Wan, R. (2024). Tropical cyclone activities in the Western North Pacific in 2022. *Tropical Cyclone Research and Review*, 125-135. <https://doi.org/https://doi.org/10.1016/j.tcr.2024.05.002>
- Ibañez, M. P., Martinez, S. C., Pura, A. G., Sajulga, R. A., Cayanan, E. O., Jou, B. J.-D., & Chang, W.-Y. (2023). Development of quantitative precipitation estimation (QPE) relations for dual-polarization radars based on raindrop size distribution measurements in Metro Manila, Philippines. *Terrestrial, Atmospheric and Oceanic Sciences*. <https://doi.org/https://doi.org/10.1007/s44195-023-00056-0>
- Ibañez, M. P., Pura, A. G., Sajulga, R. A., & David, S. J. (2022). Raindrop Size Distribution (RSD) Characteristics during the Southwest Monsoon Period in Western Luzon, Philippines. *Philippine Journal of Science*, 1-16.
- Jameson, A. R. (1991). Polarization Radar Measurements in Rain at 5 and 9 GHz. *Journal of Applied Meteorology*, 1500-1513. [https://doi.org/https://doi.org/10.1175/1520-0450\(1991\)030<1500:PRMIRA>2.0.CO;2](https://doi.org/https://doi.org/10.1175/1520-0450(1991)030<1500:PRMIRA>2.0.CO;2)
- Jameson, A. R. (1992). The Effect of Temperature on Attenuation-Correction Schemes in Rain Using Polarization Propagation Differential Phase Shift. *Journal of Applied Meteorology and Climatology*, 1106-1118. [https://doi.org/https://doi.org/10.1175/1520-0450\(1992\)031<1106:TEOTOA>2.0.CO;2](https://doi.org/https://doi.org/10.1175/1520-0450(1992)031<1106:TEOTOA>2.0.CO;2)
- Kottke, M., Grieser, J., Beck, C., Rudolf, B., & Rubel, F. (2006). World Map of the Köppen-Geiger climate classification updated. *Meteorologische Zeitschrift*, 259-263. <https://doi.org/10.1127/0941-2948/2006/0130>
- Krajewski, W. F., & Smith, J. A. (2002). Radar hydrology: rainfall estimation. *Advances in Water Resources*, 1387-1394. [https://doi.org/https://doi.org/10.1016/S0309-1708\(02\)00062-3](https://doi.org/https://doi.org/10.1016/S0309-1708(02)00062-3)
- Lin, P.-F., Lagrimas, L. K., Wang, J.-B., Chang, P.-L., Fang, W.-T., Almario, J. G., Jou, B. J.-D., & Cayanan, E. O. (2021). Removing interference echoes in Philippine radars using a fuzzy logic approach. *Terr. Atmos. Ocean. Sci.*, 755-776. <https://doi.org/10.3319/TAO.2021.12.20.01>
- Löffler-Mang, M., & Joss, J. (2000). An Optical Disdrometer for Measuring Size and Velocity of Hydrometeors. *Journal of Atmospheric and Oceanic Technology*, 130-139. [https://doi.org/https://doi.org/10.1175/1520-0426\(2000\)017<0130:AODFMS>2.0.CO;2](https://doi.org/https://doi.org/10.1175/1520-0426(2000)017<0130:AODFMS>2.0.CO;2)



- Loh, J. L., Chang, W.-Y., Hsu, H.-W., Lin, P.-F., Chang, P.-L., Teng, Y.-L., & Liou, Y.-C. (2022). Long-Term Assessment of the Reflectivity Biases and Wet-Radome Effect Using Collocated Operational S- and C-Band Dual-Polarization Radars. *IEEE Transactions on Geoscience and Remote Sensing*, Vol. 60. <https://doi.org/10.1109/TGRS.2022.3170609>
- Macuroy, J. T., Chang, W.-Y., Faustino-Eslava, D. V., Sanchez, P. A., Jr., C. L., & Jou, B. J.-D. (2021). Evaluations on radar QPE using raindrop size distribution in Southern Luzon, Philippines. *Terr. Atmos. Ocean. Sci.*, 693-724. <https://doi.org/10.3319/TAO.2021.02.22.01>
- McFarquhar, G. M., Hsieh, T.-L., Freer, M., Mascio, J., & Jewett, B. F. (2015). The Characterization of Ice Hydrometeor Gamma Size Distributions as Volumes in  $N_0-\lambda-\mu$  Phase Space: Implications for Microphysical Process Modeling. *Journal of Atmospheric Sciences*, 892–909. <https://doi.org/10.1175/JAS-D-14-0011.1>
- NASA Shuttle Radar Topography Mission (SRTM). (2013). Shuttle Radar Topography Mission (SRTM) Global. <https://doi.org/10.5069/G9445JDF>
- Ryzhkov, A., & Zrníc, D. (1996). Assessment of Rainfall Measurement That Uses Specific Differential Phase. *Journal of Applied Meteorology*, 2080-2090. [https://doi.org/10.1175/1520-0450\(1996\)035<2080:AORMTU>2.0.CO;2](https://doi.org/10.1175/1520-0450(1996)035<2080:AORMTU>2.0.CO;2)
- Seela, B. K., Janapati, J., Lin, P.-L., Reddy, K. K., Shirooka, R., & Wang, P. K. (2017). A Comparison Study of Summer Season Raindrop Size Distribution Between Palau and Taiwan, Two Islands in Western Pacific. *Journal of Geophysical Research: Atmospheres*, 11,787–11,805. <https://doi.org/10.1002/2017JD026816>
- Sekhon, R. S., & Srivastana, R. C. (1971). Doppler Radar Observations of Drop-Size Distributions in a Thunderstorm. *Journal of Atmospheric Sciences*, 983-994. [https://doi.org/10.1175/1520-0469\(1971\)028<0983:DROODS>2.0.CO;2](https://doi.org/10.1175/1520-0469(1971)028<0983:DROODS>2.0.CO;2)
- Smyth, T. J., & Illingworth, A. J. (1998). Correction for attenuation of radar reflectivity using polarization data. *Quarterly Journal of the Royal Meteorological Society*, 2393-2415. <https://doi.org/10.1002/qj.49712455111>
- Testud, J., Oury, S., Black, R. A., Amayenc, P., & Dou, X. (2001). The Concept of “Normalized” Distribution to Describe Raindrop Spectra: A Tool for Cloud Physics and Cloud Remote Sensing. *Journal of Applied Meteorology*, 1118-1140. [https://doi.org/10.1175/1520-0450\(2001\)040<1118:TCOND>2.0.CO;2](https://doi.org/10.1175/1520-0450(2001)040<1118:TCOND>2.0.CO;2)
- Thompson, E. J., Rutledge, S. A., Dolan, B., & Thurai, M. (2015). Drop size distributions and radar observations of convective and stratiform rain over the equatorial Indian and West Pacific Oceans. *Journal of the Atmospheric Sciences*, 72(11), 4091–4125. <https://doi.org/10.1175/jas-d-14-0206.1>
- Ulbrich, C. W. (1983). Natural Variations in the Analytical Form of the Raindrop Size Distribution. *Journal of Climate and Applied Meteorology*, 1764-1775. [https://doi.org/10.1175/1520-0450\(1983\)022<1764:NVITAF>2.0.CO;2](https://doi.org/10.1175/1520-0450(1983)022<1764:NVITAF>2.0.CO;2)

- Vivekanandan, J., Zhang, G., Ellis, S. M., Rajopadhyaya, D., & Avery, S. K. (2003). Radar reflectivity calibration using differential propagation phase measurement. *Radio Science*. <https://doi.org/10.1029/2002RS002676>
- Vulpiani, G., Montopoli, M., Passeri, L. D., Gioia, A. G., Giordano, P., & Marzano, F. S. (2012). On the Use of Dual-Polarized C-Band Radar for Operational Rainfall Retrieval in Mountainous Areas. *Journal of Applied Meteorology and Climatology*, 405-425. <https://doi.org/10.1175/JAMC-D-10-05024.1>
- Waterman, P. C. (1971). Symmetry, unitarity, and geometry in electromagnetic scattering. *Phys. Rev. D*, 825-839. <https://doi.org/https://doi.org/10.1103/PhysRevD.3.825>
- Williams, C. R., Bringi, V. N., Carey, L. D., Chandrasekar, V., Gatlin, P. N., Haddad, Z. S., Meneghini, R., Munchak, S. J., Nesbitt, S. W., Petersen, W. A., Tanelli, S., Tokay, A., Wilson, A., & Wolff, D. B. (2014). Describing the Shape of Raindrop Size Distributions Using Uncorrelated Raindrop Mass Spectrum Parameters. *Journal of Applied Meteorology and Climatology*, 1282-1296. <https://doi.org/10.1175/JAMC-D-13-076.1>
- Willis, P. T. (1984). Functional Fits to Some Observed Drop size Distributions and Parameterization of Rain. *Journal of Atmospheric Sciences*, 1648-1661. [https://doi.org/https://doi.org/10.1175/1520-0469\(1984\)041<1648:FFTSOD>2.0.CO;2](https://doi.org/https://doi.org/10.1175/1520-0469(1984)041<1648:FFTSOD>2.0.CO;2)
- Yuter, S. E., & Houze, R. J. (1997). Measurements of Raindrop Size Distributions over the Pacific Warm Pool and Implications for Z-R Relations. *Journal of Applied Meteorology*, 847-867. [https://doi.org/https://doi.org/10.1175/1520-0450\(1997\)036<0847:MORSOD>2.0.CO;2](https://doi.org/https://doi.org/10.1175/1520-0450(1997)036<0847:MORSOD>2.0.CO;2)

# Appendix

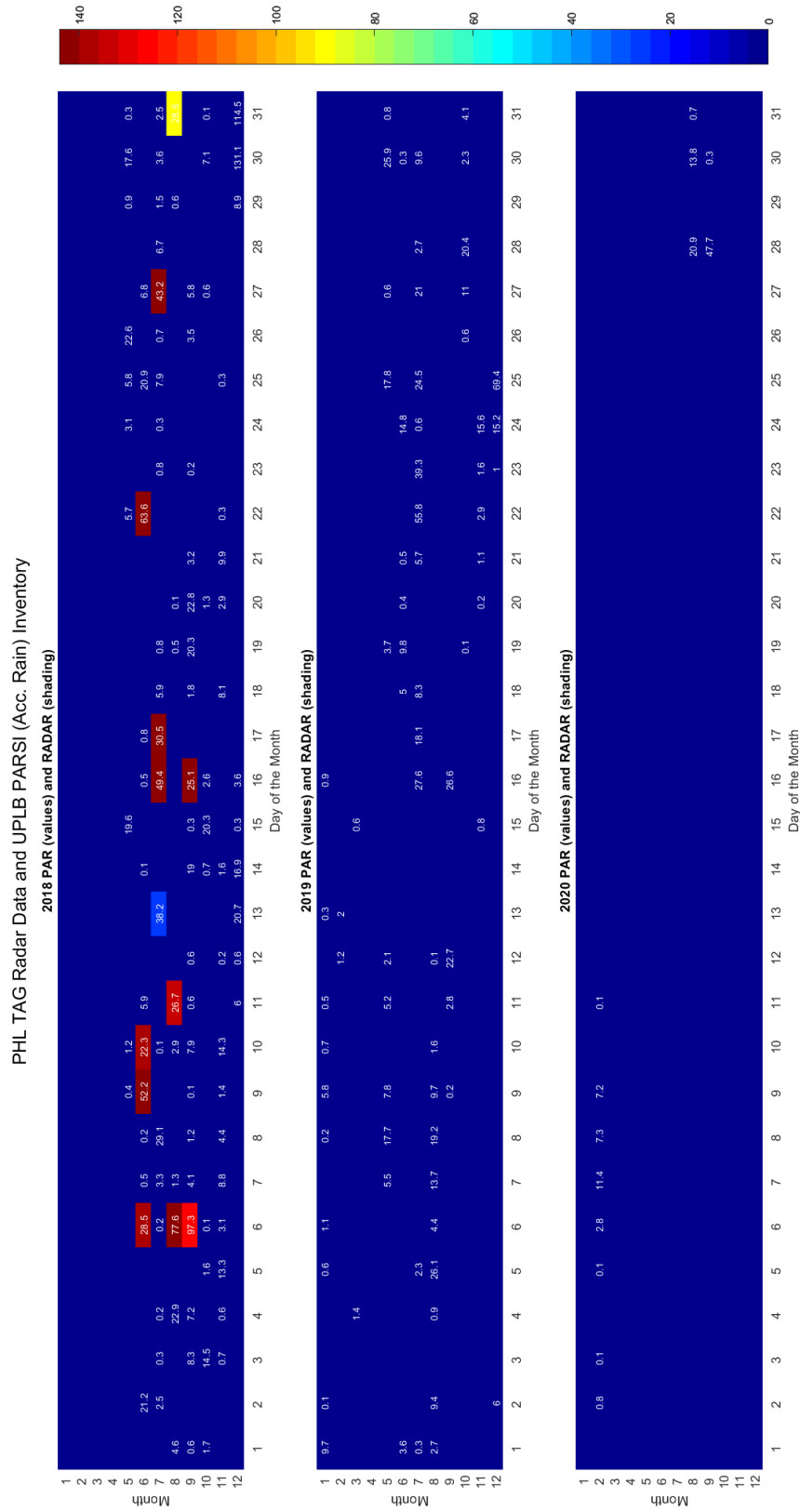


Figure A. 1 Inventory of PHL Tagaytay radar data and PARSIVEL disdrometer data from 2018–2020. Values represent the number of 1-min DSD data while the shading represents the available radar data.

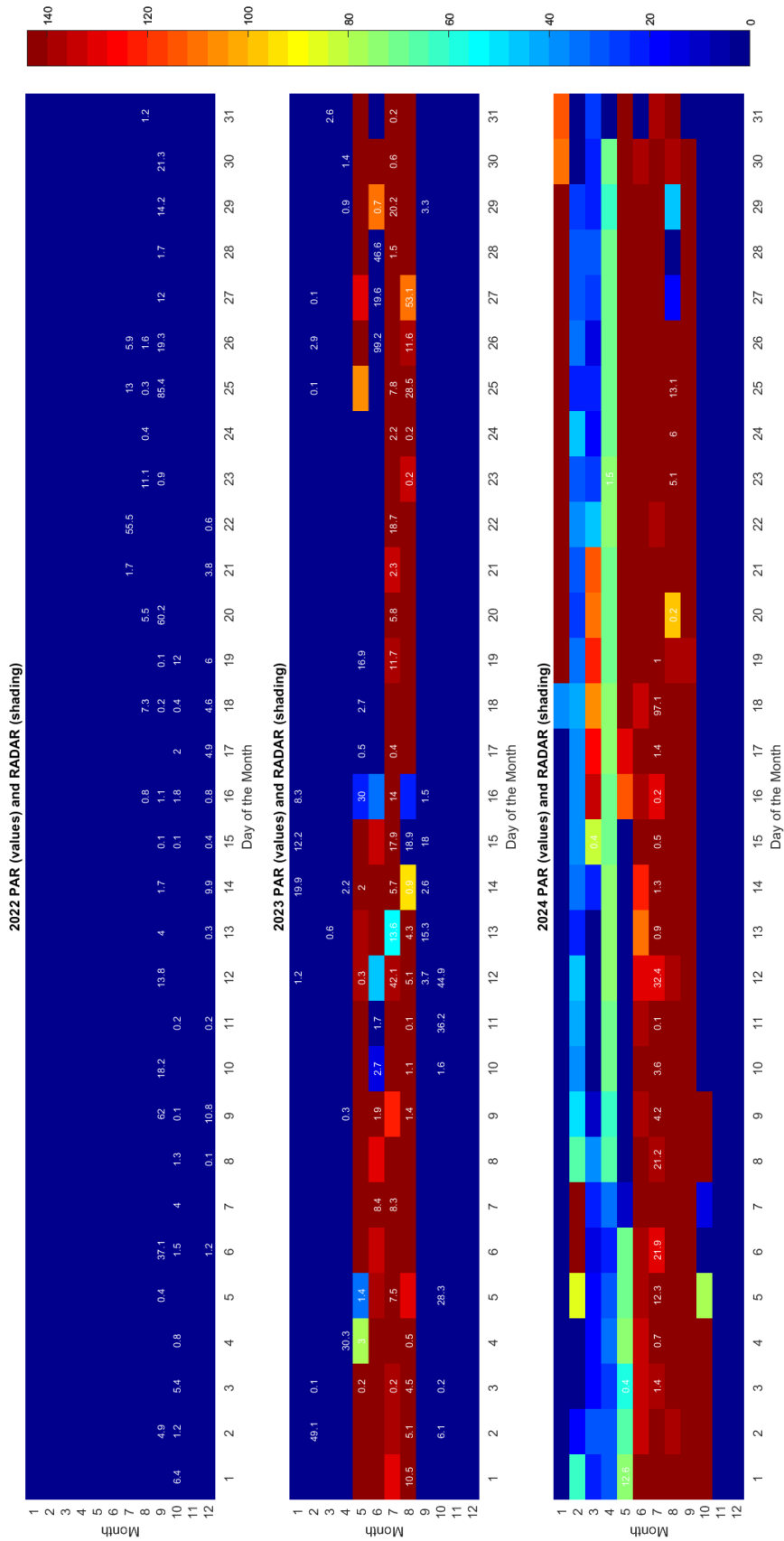


Figure A. 2 Inventory of PHL Tagaytay radar data and PARSIVEL disdrometer data from 2022-2024. Values represent the number of 1-min DSD data while the shading represents the available radar data.

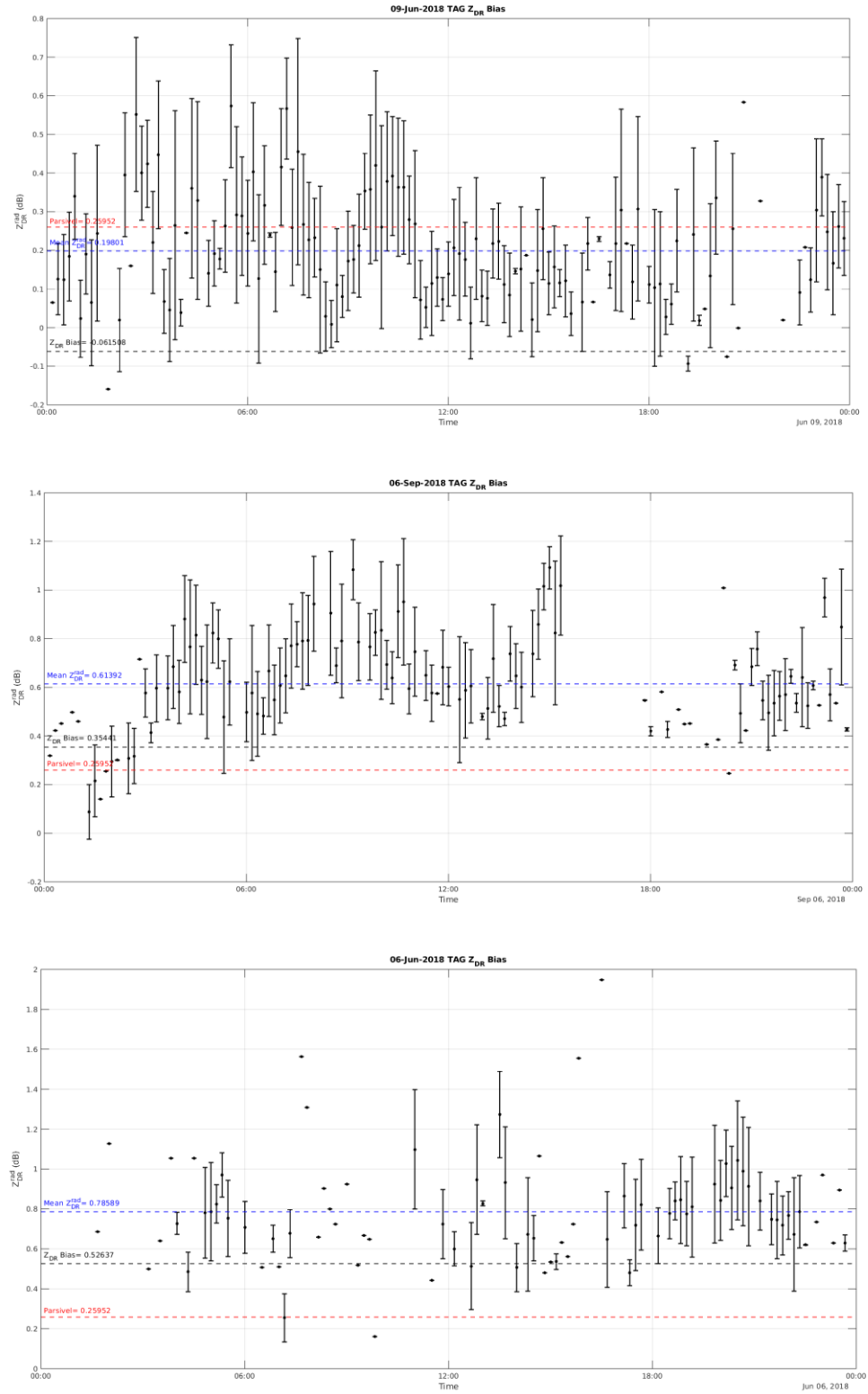


Figure A. 3 ZDR system bias for 09Jun2018, 06Sep2018 and 06Jun2018. Dots and lines are the time series of ZDR and standard deviation. Blue broken line is the mean ZDR calculated from radar; the red line is the mean ZDR from the disdrometer; and the black line shows the calculated Z<sub>DR</sub> system bias.

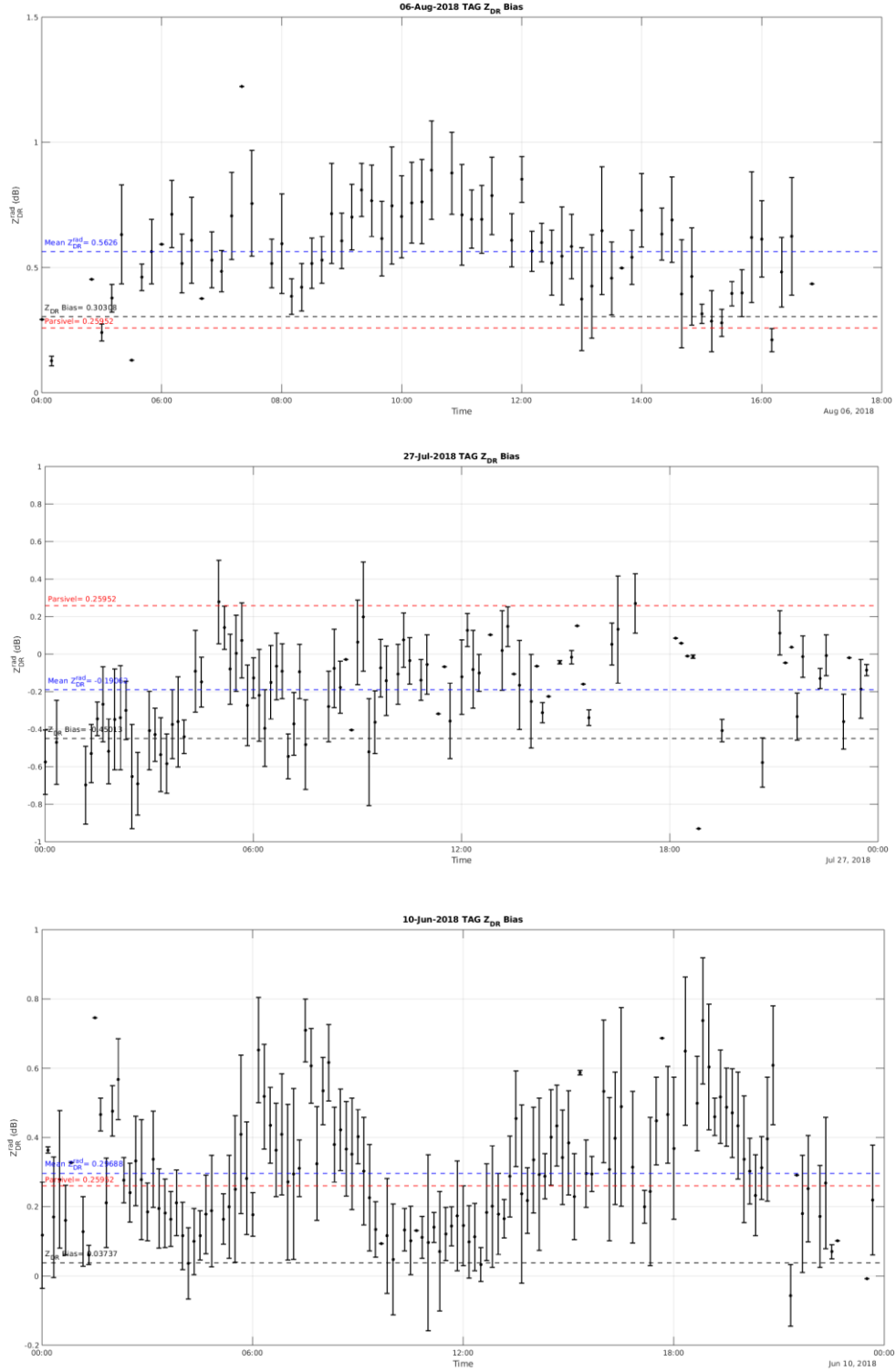


Figure A. 4  $Z_{DR}$  system bias for 06Aug2018, 27Jul2018 and 10Jun2018. Dots and lines are the time series of  $Z_{DR}$  and standard deviation. Blue broken line is the mean  $Z_{DR}$  calculated from radar, the red line is the mean  $Z_{DR}$  from the disdrometer, and the black line shows the calculated  $Z_{DR}$  system bias.

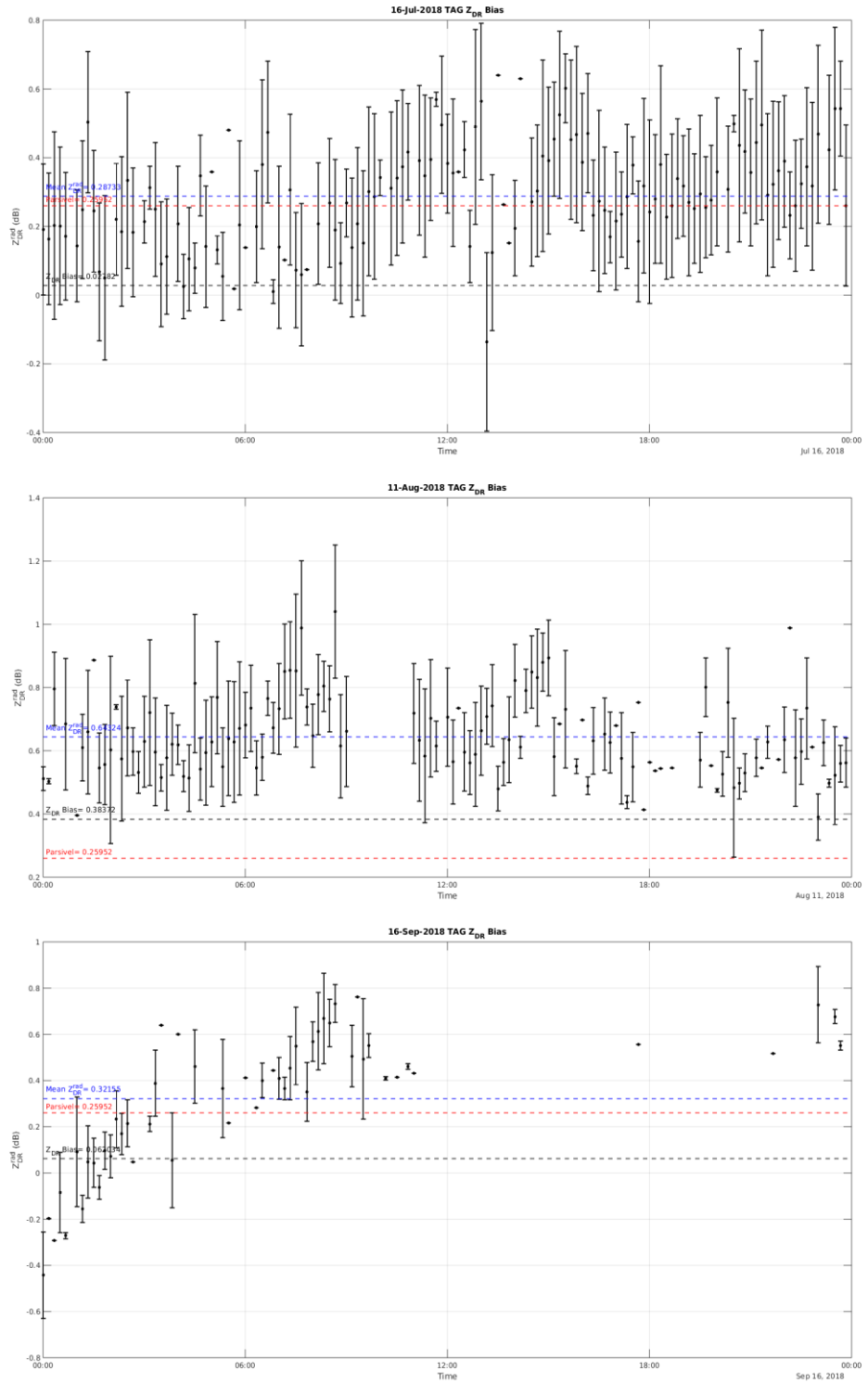


Figure A. 5  $Z_{DR}$  system bias for 16Jul2018, 11Aug018 and 16Sep2018. Dots and lines are the time series of  $Z_{DR}$  and standard deviation. Blue broken line is the mean  $Z_{DR}$  calculated from radar, the red line is the mean  $Z_{DR}$  from the disdrometer, and the black line shows the calculated  $Z_{DR}$  system bias.



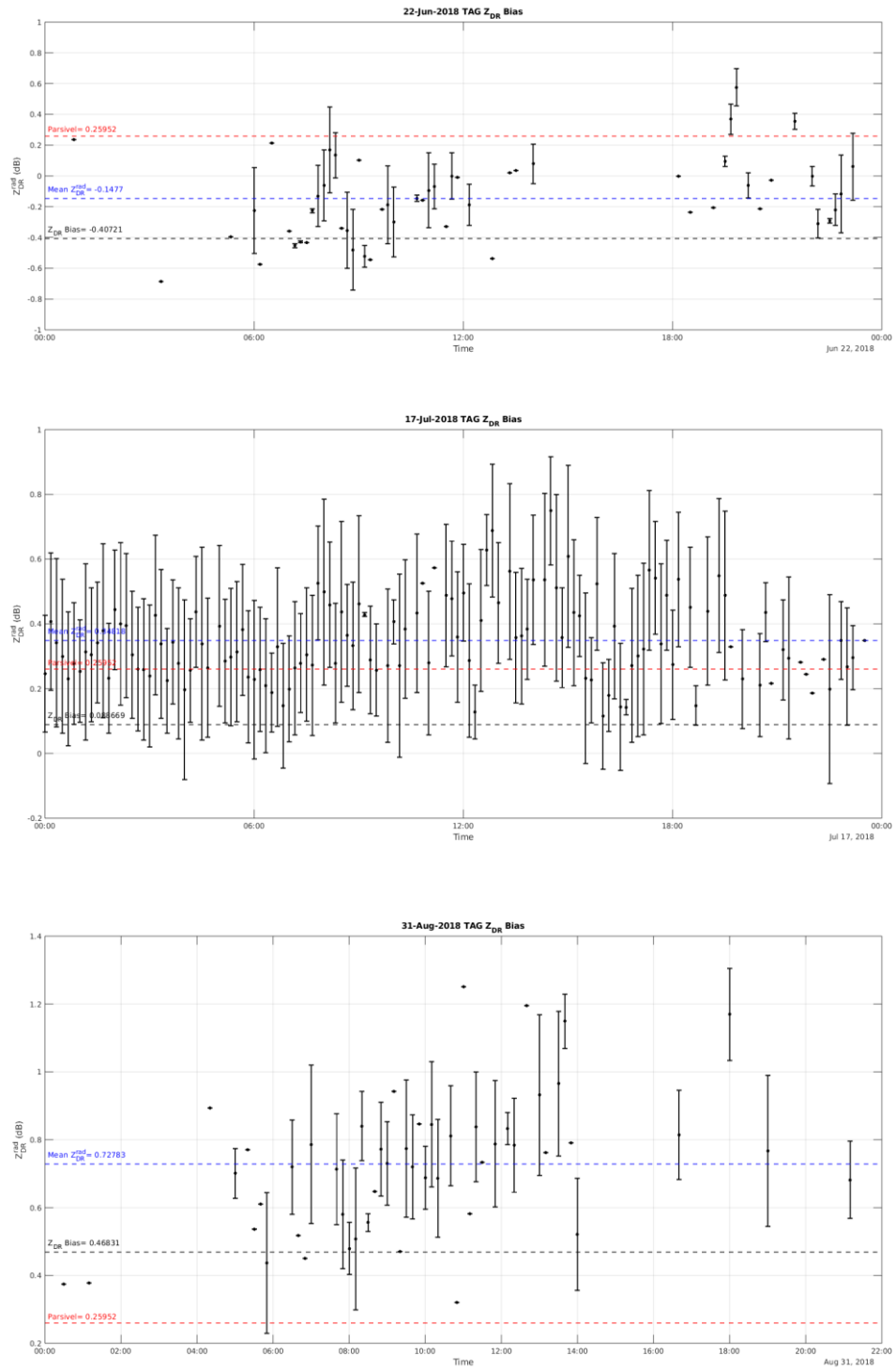


Figure A. 6  $Z_{DR}$  system bias for 22Jun2018, 17Jul2018 and 31Aug2018. Dots and lines are the time series of  $Z_{DR}$  and standard deviation. Blue broken line is the mean  $Z_{DR}$  calculated from radar, the red line is the mean  $Z_{DR}$  from the disdrometer, and the black line shows the calculated  $Z_{DR}$  system bias.

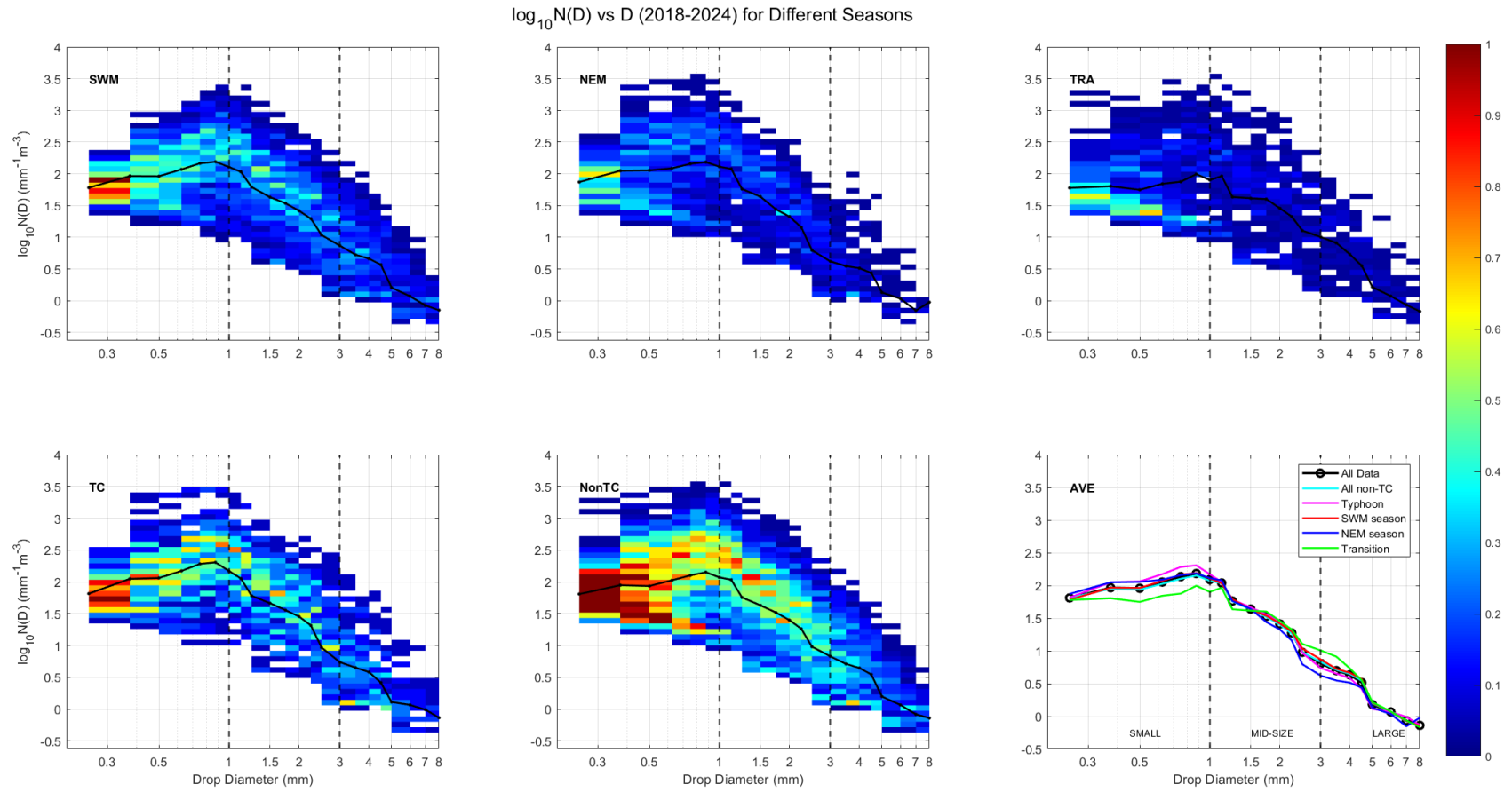


Figure A. 7 Frequency distribution of DSD for (a) SWM, (b) NEM, (c) transition months, (d) TC rains, (e) all non-TC rains and (f) average.

*Table A 1 Full list of rain events during the 2018 SWM season in South Luzon, Philippines.*

<b>Event No</b>	<b>start_time</b>	<b>st_id</b>	<b>end_time</b>	<b>ed_id</b>	<b>max_r</b>	<b>min_r</b>	<b>ave_r</b>	<b>Duration (min)</b>
1	06/06/2018 5:00	1	06/06/2018 5:46	45	8.439	1.092	4.27695556	46
2	06/06/2018 13:32	48	06/06/2018 13:45	61	2.383	1.148	1.72992857	13
3	06/06/2018 18:07	62	06/06/2018 20:18	192	46.285	1.177	11.3631908	131
4	09/06/2018 2:15	194	09/06/2018 3:13	243	57.766	1.102	5.65914	58
5	09/06/2018 3:24	244	09/06/2018 3:33	251	1.46	1.106	1.259875	9
6	09/06/2018 3:47	252	09/06/2018 4:04	264	2.272	1.204	1.57307692	17
7	09/06/2018 4:41	265	09/06/2018 5:19	297	50.627	1.163	12.9284545	38
8	09/06/2018 5:39	298	09/06/2018 6:03	320	107.493	1.238	32.4657391	24
9	09/06/2018 6:46	321	09/06/2018 7:24	359	69.854	1.279	17.4158205	38
10	09/06/2018 9:46	360	09/06/2018 11:10	431	16.687	1.098	3.63668056	84
11	09/06/2018 12:27	432	09/06/2018 13:09	474	46.442	1.273	11.2007442	42
12	09/06/2018 13:28	475	09/06/2018 13:49	485	3.767	1.176	1.75836364	21
13	09/06/2018 15:34	486	09/06/2018 15:44	496	25.424	2.65	9.025	10
14	09/06/2018 23:27	497	09/06/2018 23:58	520	10.758	1.463	4.35241667	31
15	10/06/2018 0:12	521	10/06/2018 0:23	525	5.939	2.016	3.488	11
16	10/06/2018 0:43	526	10/06/2018 0:59	542	5.881	1.194	2.59376471	16
17	10/06/2018 1:11	543	10/06/2018 2:23	606	12.752	1.092	5.42071875	72
18	10/06/2018 5:43	610	10/06/2018 6:43	670	8.564	1.114	3.9567377	60
19	10/06/2018 7:21	671	10/06/2018 7:50	700	7.246	1.136	4.11716667	29
20	10/06/2018 8:10	701	10/06/2018 8:43	725	3.253	1.21	1.95276	33
21	10/06/2018 9:09	726	10/06/2018 9:18	735	1.555	1.197	1.4229	9
22	10/06/2018 11:27	736	10/06/2018 11:31	739	1.953	1.11	1.49675	4
23	10/06/2018 13:54	740	10/06/2018 13:59	741	1.391	1.283	1.337	5
24	10/06/2018 14:48	742	10/06/2018 15:11	760	3.969	1.125	2.29763158	23
25	10/06/2018 16:00	761	10/06/2018 16:03	763	1.287	1.125	1.20333333	3
26	10/06/2018 16:14	764	10/06/2018 16:59	798	4.881	1.09	2.1204	45
27	10/06/2018 17:13	799	10/06/2018 19:58	930	6.688	1.105	2.67912121	165
28	22/06/2018 6:55	931	22/06/2018 7:37	966	256.541	1.749	101.404278	42

29	22/06/2018 10:25	968	22/06/2018 10:45	985	39.681	1.155	8.71038889	20
30	22/06/2018 19:49	986	22/06/2018 19:53	990	2.334	1.308	1.8244	4
31	08/07/2018 5:34	991	08/07/2018 6:01	1018	22.433	1.336	8.05364286	27
32	08/07/2018 6:54	1019	08/07/2018 9:55	1189	53.112	1.101	8.88488304	181
33	13/07/2018 9:05	1191	13/07/2018 12:03	1369	121.507	1.158	12.785095	178
34	16/07/2018 2:23	1372	16/07/2018 2:32	1380	2.364	0.547	1.65788889	9
35	16/07/2018 8:49	1381	16/07/2018 9:01	1384	2.716	1.35	1.71625	12
36	16/07/2018 10:10	1385	16/07/2018 11:05	1432	18.092	1.442	5.58570833	55
37	16/07/2018 11:27	1433	16/07/2018 11:33	1439	2.404	1.101	1.98728571	6
38	16/07/2018 12:00	1440	16/07/2018 16:19	1683	35.392	1.078	6.42396311	259
39	16/07/2018 18:35	1684	16/07/2018 18:38	1687	3.702	1.342	2.6295	3
40	16/07/2018 19:51	1688	16/07/2018 21:51	1782	45.187	1.207	7.04824211	120
41	16/07/2018 22:05	1783	17/07/2018 0:04	1857	33.288	1.116	5.53281333	119
42	17/07/2018 3:28	1859	17/07/2018 3:38	1865	19.781	1.144	8.64042857	10
43	17/07/2018 4:22	1866	17/07/2018 5:01	1895	11.01	1.094	3.71496667	39
44	17/07/2018 5:49	1896	17/07/2018 5:52	1899	13.322	1.862	6.69625	3
45	17/07/2018 8:27	1900	17/07/2018 9:06	1939	6.788	1.422	3.19985	39
46	17/07/2018 9:17	1940	17/07/2018 10:12	1975	52.988	1.156	10.2170556	55
47	17/07/2018 10:25	1976	17/07/2018 10:45	1996	59.621	1.888	18.7624762	20
48	17/07/2018 11:53	1998	17/07/2018 12:22	2020	12.406	1.293	3.92321739	29
49	17/07/2018 13:13	2021	17/07/2018 15:24	2127	22.225	1.317	5.30014019	131
50	17/07/2018 16:47	2129	17/07/2018 16:56	2138	25.412	1.187	6.7382	9
51	27/07/2018 0:25	2141	27/07/2018 0:27	2143	1.825	1.217	1.49666667	2
52	27/07/2018 0:39	2144	27/07/2018 3:15	2300	87.183	1.139	14.3507197	156
53	27/07/2018 5:46	2301	27/07/2018 5:51	2306	6.314	1.211	3.87866667	5
54	27/07/2018 8:12	2309	27/07/2018 9:08	2360	13.411	1.657	5.85175	56
55	06/08/2018 5:13	2363	06/08/2018 6:12	2410	263.337	0.741	89.7727917	59
56	06/08/2018 8:40	2411	06/08/2018 9:21	2448	37.518	1.202	7.73934211	41
57	06/08/2018 10:37	2449	06/08/2018 11:42	2485	2.85	1.079	1.50208108	65
58	11/08/2018 3:20	2486	11/08/2018 3:22	2488	1.84	1.285	1.502	2

59	11/08/2018 5:02	2493	11/08/2018 5:42	2525	40.503	1.272	6.87672727	40
60	11/08/2018 5:55	2526	11/08/2018 5:59	2528	9.733	3.105	5.76733333	4
61	11/08/2018 6:23	2529	11/08/2018 6:46	2539	11.752	1.221	3.84672727	23
62	11/08/2018 7:11	2540	11/08/2018 7:40	2569	57.632	1.343	8.27326667	29
63	11/08/2018 7:59	2570	11/08/2018 9:37	2639	90.054	1.14	14.0475857	98
64	11/08/2018 10:05	2640	11/08/2018 10:07	2642	2.423	0.771	1.775	2
65	11/08/2018 10:36	2643	11/08/2018 10:41	2644	0.536	0.512	0.524	5
66	11/08/2018 13:30	2649	11/08/2018 13:51	2669	4.238	1.308	2.48142857	21
67	31/08/2018 8:12	2671	31/08/2018 8:19	2678	26.693	1.916	12.52175	7
68	31/08/2018 14:16	2679	31/08/2018 16:30	2802	52.959	1.245	12.4264435	134
69	31/08/2018 16:46	2803	31/08/2018 17:32	2841	3.524	1.217	1.92338462	46
70	06/09/2018 3:14	2842	06/09/2018 3:17	2845	7.425	1.901	4.4515	3
71	06/09/2018 3:56	2846	06/09/2018 4:06	2856	83.365	2.006	19.4781818	10
72	06/09/2018 4:20	2857	06/09/2018 4:23	2860	5.52	1.253	3.27525	3
73	06/09/2018 5:13	2861	06/09/2018 5:18	2866	66.538	1.214	17.4958333	5
74	06/09/2018 7:47	2867	06/09/2018 8:20	2893	38.987	1.088	6.39840741	33
75	06/09/2018 8:55	2894	06/09/2018 8:59	2898	9.184	1.524	5.331	4
76	06/09/2018 9:47	2899	06/09/2018 9:52	2904	1.661	1.096	1.30266667	5
77	06/09/2018 11:08	2905	06/09/2018 11:36	2933	12.609	1.738	6.68665517	28
78	06/09/2018 12:19	2934	06/09/2018 13:05	2968	3.301	1.212	2.02151429	46
79	06/09/2018 13:17	2969	06/09/2018 15:23	3085	181.427	1.096	36.1632222	126
80	06/09/2018 15:42	3086	06/09/2018 16:00	3104	15.625	1.29	5.62673684	18
81	06/09/2018 16:35	3107	06/09/2018 17:30	3158	32.278	1.575	7.56609615	55
82	06/09/2018 18:22	3159	06/09/2018 18:47	3180	16.17	1.448	5.23590909	25
83	06/09/2018 19:48	3181	06/09/2018 19:52	3184	1.907	1.189	1.42875	4
84	06/09/2018 22:06	3185	06/09/2018 22:10	3189	2.475	1.178	1.8206	4
85	06/09/2018 22:36	3190	06/09/2018 23:00	3210	28.996	1.152	7.20109524	24
86	16/09/2018 8:38	3211	16/09/2018 9:17	3250	98.983	3.611	37.69225	39

*Table A 2 Full list of time-matched PG-radar data for the 2018 SWM season in South Luzon Philippines.*

	<b>year</b>	<b>MM</b>	<b>dd</b>	<b>hhmm</b>	<b>radar_date</b>	<b>event_no</b>	<b>pca_rep</b>
1	2018	06	06	0500	201806060500	1	2
2	2018	06	06	1030	201806061030	2	2
3	2018	06	06	1810	201806061810	3	1
4	2018	06	06	1820	201806061820	3	1
5	2018	06	06	1830	201806061830	3	1
6	2018	06	06	1840	201806061840	3	1
7	2018	06	06	1850	201806061850	3	1
8	2018	06	06	1940	201806061940	3	4
9	2018	06	06	1950	201806061950	3	4
10	2018	06	06	2000	201806062000	3	4
11	2018	06	06	2010	201806062010	3	4
12	2018	06	09	0210	201806090210	4	1
13	2018	06	09	0220	201806090220	4	1
14	2018	06	09	0250	201806090250	4	2
15	2018	06	09	0310	201806090310	4	2
16	2018	06	09	0320	201806090320	4	2
17	2018	06	09	0440	201806090440	7	1
18	2018	06	09	0450	201806090450	7	1
19	2018	06	09	0540	201806090540	8	1
20	2018	06	09	0550	201806090550	8	1
21	2018	06	09	0650	201806090650	9	1
22	2018	06	09	0700	201806090700	9	4
23	2018	06	09	0710	201806090710	9	4
24	2018	06	09	1010	201806091010	10	1
25	2018	06	09	1030	201806091030	10	4
26	2018	06	09	1230	201806091230	11	5
27	2018	06	09	1240	201806091240	11	3
28	2018	06	09	1250	201806091250	11	3
29	2018	06	10	0140	201806100140	17	4
30	2018	06	10	0200	201806100200	17	2
31	2018	06	10	0210	201806100210	17	2
32	2018	06	10	0620	201806100620	18	2
33	2018	06	10	0810	201806100810	20	2
34	2018	06	10	0820	201806100820	20	2
35	2018	06	10	0830	201806100830	20	4
36	2018	06	10	1450	201806101450	24	4
37	2018	06	10	1610	201806101610	26	2

38	2018	06	10	1620	201806101620	26	2
39	2018	06	10	1630	201806101630	26	2
40	2018	06	10	1640	201806101640	26	2
41	2018	06	10	1650	201806101650	26	2
42	2018	06	10	1710	201806101710	27	4
43	2018	06	10	1720	201806101720	27	4
44	2018	06	10	1730	201806101730	27	2
45	2018	06	10	1740	201806101740	27	2
46	2018	06	10	1750	201806101750	27	2
47	2018	06	10	1800	201806101800	27	2
48	2018	06	10	1810	201806101810	27	2
49	2018	06	10	1820	201806101820	27	4
50	2018	06	10	1900	201806101900	27	4
51	2018	06	10	1940	201806101940	27	4
52	2018	06	10	1950	201806101950	27	4
53	2018	06	22	0710	201806220710	28	6
54	2018	06	22	0720	201806220720	28	1
55	2018	06	22	0730	201806220730	28	1
56	2018	06	22	1030	201806221030	29	1
57	2018	07	16	1020	201807161020	36	3
58	2018	07	16	1030	201807161030	36	3
59	2018	07	16	1040	201807161040	36	5
60	2018	07	16	1050	201807161050	36	5
61	2018	07	16	1230	201807161230	38	3
62	2018	07	16	1300	201807161300	38	1
63	2018	07	16	1340	201807161340	38	1
64	2018	07	16	1400	201807161400	38	4
65	2018	07	16	1410	201807161410	38	4
66	2018	07	16	1500	201807161500	38	2
67	2018	07	16	1510	201807161510	38	2
68	2018	07	16	1540	201807161540	38	2
69	2018	07	16	1550	201807161550	38	2
70	2018	07	16	1600	201807161600	38	2
71	2018	07	16	1610	201807161610	38	2
72	2018	07	16	2000	201807162000	40	3
73	2018	07	16	2020	201807162020	40	4
74	2018	07	16	2030	201807162030	40	4
75	2018	07	16	2100	201807162100	40	1
76	2018	07	16	2110	201807162110	40	1
77	2018	07	17	0420	201807170420	43	2



78	2018	07	17	0920	201807170920	46	3
79	2018	07	17	1000	201807171000	46	1
80	2018	07	17	1020	201807171020	47	1
81	2018	07	17	1030	201807171030	47	1
82	2018	07	17	1150	201807171150	48	3
83	2018	07	17	1210	201807171210	48	2
84	2018	07	17	1310	201807171310	49	4
85	2018	07	17	1320	201807171320	49	4
86	2018	07	17	1410	201807171410	49	1
87	2018	07	17	1420	201807171420	49	3
88	2018	07	17	1440	201807171440	49	4
89	2018	07	17	1450	201807171450	49	4
90	2018	07	17	1510	201807171510	49	3
91	2018	07	17	1520	201807171520	49	3
92	2018	07	27	0810	201807270810	54	3
93	2018	07	27	0820	201807270820	54	3
94	2018	07	27	0830	201807270830	54	3
95	2018	07	27	0840	201807270840	54	3
96	2018	08	06	0520	201808060520	55	1
97	2018	08	06	0530	201808060530	55	1
98	2018	08	06	0540	201808060540	55	1
99	2018	08	06	0550	201808060550	55	6
100	2018	08	06	0840	201808060840	56	3
101	2018	08	06	0850	201808060850	56	1
102	2018	08	06	0900	201808060900	56	1
103	2018	08	06	0910	201808060910	56	4
104	2018	08	06	1050	201808061050	57	2
105	2018	08	06	1100	201808061100	57	2
106	2018	08	06	1110	201808061110	57	2
107	2018	08	06	1120	201808061120	57	2
108	2018	08	11	0530	201808110530	59	1
109	2018	08	11	0710	201808110710	62	1
110	2018	08	11	0810	201808110810	63	1
111	2018	08	11	0820	201808110820	63	1
112	2018	08	11	0830	201808110830	63	1
113	2018	08	11	0900	201808110900	63	2
114	2018	08	11	1330	201808111330	66	4
115	2018	08	11	1340	201808111340	66	4
116	2018	09	06	0400	201809060400	71	6
117	2018	09	06	1230	201809061230	78	2

118	2018	09	06	1330	201809061330	79	1
119	2018	09	06	1340	201809061340	79	1
120	2018	09	06	1350	201809061350	79	1
121	2018	09	06	1400	201809061400	79	1
122	2018	09	06	1410	201809061410	79	6
123	2018	09	06	1420	201809061420	79	6
124	2018	09	06	1430	201809061430	79	1
125	2018	09	06	1510	201809061510	79	3
126	2018	09	06	1520	201809061520	79	3
127	2018	09	06	1820	201809061820	82	5
128	2018	09	06	1830	201809061830	82	3
129	2018	09	16	0840	201809160840	86	1
130	2018	09	16	0850	201809160850	86	6
131	2018	09	16	0900	201809160900	86	6

---